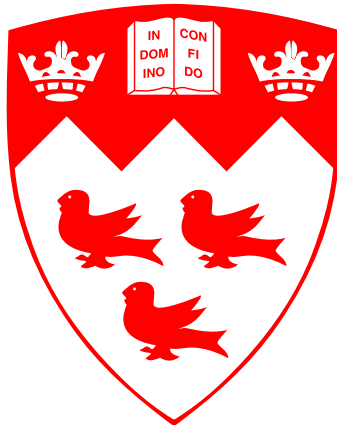


# Electronic Transport in Hydrogenated Graphene

*Jonathan Guillemette*



Department of Physics  
McGill University  
Montréal, Québec, Canada

January 2014

Under the supervision of Professors Thomas Szkopek and Guillaume Gervais

---

A thesis submitted to McGill University in partial fulfillment of the requirements for the degree of Doctor of Philosophy.

© 2014 Jonathan Guillemette

## Acknowledgements

I'd like to begin by thanking Thomas for believing in this project from day one. Your patience and pedagogy with me have been the main ingredients in my growth as a scientist. Your passion for science is contagious and your ability to communicate it so clearly make it a privilege to be around. I will look back on our discussions in Tallahassee and Toulouse as the better moments of this project. I would also like to thank Guillaume for asking what happens when  $B \neq 0$  and having the instinct to pursue it to the end. Thank you for keeping the bar so high that I cannot always reach it. Finally, keep gambling on experimental results, your luck is bound to change!

Essential to the success of this project is the input from the Université de Montréal group led by Prof. Richard Martel, who made us realize the interesting chemical side of this project and who is always a source of insightful scientific advice. Dr. Pierre Lévesque, the best experimental set-up builder I know, was of immense help in getting the hydrogenation gun working. Finally, gratitude goes to Dr. Nicolas Cottenye, who helped me collect and analyze the Raman maps on a new machine under time pressure. Also crucial to this project was the endless source of graphene on copper provided by the Université du Québec à Montréal group led by Prof. Mohammed Siaj. Many samples were made because of the sustained efforts of Dr. Abdelaadim Guerroune and Farzaneh Mahvash Mohammadi. At McGill, I would like to thank Prof. Marta Cerruti for allowing us to use the Raman spectrometer, Jun Li and Don Berry of the microfab for helping out on short notice, Richard Talbot for our repetitive break out box requests and Derek Wong from the Technology

Transfer Office for helping us file the patent. I would like to thank the staff at the NHMFL in Tallahassee, specifically Jonathan Billings, Ju-Hyun Park, Glover Jones and Tim Murphy. Their help under the time pressure of the maglab helped realize the results of this project. Finally, I would like to thank the researchers at the LNCMI in Toulouse, namely Baptiste Vignolle, David Vignolles, David LeBoeuf and Cyril Proust, without whom the measurements would never have worked.

Thanks to Shadi, Helgi, Liz, Peter and Mohammed for the many discussions about scientific and non-scientific topics and for forcing me, as the local, to explain my country and its systems. Thanks also to Dr. Keyan Bennaceur, Dr. Bixin Wu, Michel Savard and Ben Schmidt who have helped me master an arsenal of low temperature fridges. I would like to acknowledge the contribution of Samuel Gaucher in helping me make aesthetically pleasing figures.

I'd like to express my gratitude to the Fonds Québécois de la Recherche sur la Nature et les Technologies, without whom, this entire project would never have seen the light of day.

Merci à mes parents qui ont toujours eu confiance en mes capacités. Votre support a été très apprécié lors des moments plus difficiles.

Finalement, merci à mon épouse, ton écoute et ta lecture de situations difficiles ont été essentiels. Tu as *probablement* fini d'entendre parler de graphène!

## Abstract

The overarching goal of this thesis is to make use of adatoms to tune the electronic properties of a 2D atomic crystal. Specifically, covalently bonding hydrogen adatoms on a graphene sheet by creating  $\text{CH}_x$  with the aim of opening a band gap. This thesis reports the modification of the Raman spectra, the temperature dependent transport and the magnetoresistance as a result of hydrogenating graphene.

Presented in this thesis is a method by which graphene is hydrogenated, the spatial map and density of defects from Raman spectroscopy and the temperature dependent resistance of a hydrogenated graphene sheet. The hydrogenation time was found to correlate poorly with the mean D/G ratio over an area of 200 by 200  $\mu\text{m}^2$ . Samples are observed to hydrogenate at different rates. Also presented are two potential technological applications of hydrogenated graphene: thermometers and bolometers. Thermometers with sensitivities up to  $\approx 10^7 \Omega/\text{K}$  at 10 K were measured as well as bolometers with responsivities up to  $\approx 10^5 \text{V/W}$  at 10 K and a thermal resistance of  $R_{th} = 3\text{K/nW}$  at 10 K. Measurements of the magnetic field dependent transport in both perpendicular and parallel field configurations have been shown to yield opposite magnetoresistance signs. The colossal negative magnetoresistance found in the perpendicular configuration led to the emergence of the  $\nu = -2$  quantum Hall state from an insulating state in the most disordered 2D system to date as measured by a Ioffe-Regel parameter of  $\approx 250$ .

---

## Abrégé

Le but sous-jacent de cette thèse est d'utiliser des adatoms sur un cristal atomique bi-dimensionnel afin d'en ajuster les propriétés électriques. Plus précisément, un lien covalent s'établira entre les atomes d'hydrogène et la feuille de graphène en créant  $\text{CH}_x$  afin d'ouvrir un interstice entre les bandes de valence et de conduction. En attachant les atomes d'hydrogène sur la feuille de graphène, son spectre Raman, son transport en fonction de la température et sa magnéto-résistance ont tous été modifiés. L'investigation de ces modifications est le thème central de cette thèse.

Cette thèse contient: la méthode par laquelle le graphène est hydrogéné, l'analyse de l'hydrogénation en obtenant une cartographie Raman de l'ampleur des défauts et de leur emplacement sur l'échantillon. Également présent est l'analyse de l'hydrogénation du point de vue du transport électrique en fonction de la température. La durée de l'hydrogénation ne démontre pas une bonne corrélation avec le ratio D/G moyen sur une surface de 200 par 200  $\mu\text{m}^2$  obtenu par spectroscopie Raman. De plus, il est démontré que les échantillons s'hydrogènent à des rythmes différents. Également présentés sont deux applications technologiques qui pourraient être potentiellement bonifiées en utilisant le graphène hydrogéné: les thermomètres et les bolomètres. Les thermomètres démontrent une sensibilité allant jusqu'à  $\approx 10^7 \Omega/\text{K}$  à 10 K et les bolomètres démontrent une responsivité allant jusqu'à  $\approx 10^5 \text{V}/\text{W}$  à 10 K et une résistance thermique allant jusqu'à  $R_{th} = 3\text{K}/\text{nW}$ , à 10 K. La magnéto-résistance colossale négative mesurée dans la configuration perpendiculaire a mené à la mesure

de l'effet Hall quantique dans le système le plus désordonné à ce jour en termes du paramètre Ioffe-Regel qui est de  $\approx 250$ . La magnétorésistance colossale négative démontre la transition d'un état isolant à l'état de l'effet Hall quantique  $\nu = -2$ .

## Statement of Originality

In this thesis, the following scholarly contributions are described:

1. Creation of a hydrogenation gun contained in a UHV chamber. Measurement *in-situ* of four point resistance during hydrogenation.
2. Characterization of the hydrogenation process on a graphene sheet. Evolution of the Raman spectra and the temperature dependent transport as a function of hydrogenation time.
3. Demonstration of the use of hydrogenated graphene as a low temperature thermometer and bolometer.
4. The observation of the emergence of the quantum Hall effect at  $\nu = -2$  from an insulating state in hydrogenated graphene.

The original contributions of the author are listed below. Items one and two are relevant to this thesis and published in peer reviewed journals, item three pertains to this thesis and is under review and item four is a patent submitted to the US Patent Office.

1. A. Guermoune, T. Chari, F.B. Popescu, S. Sabri, *J. Guillemette*, H.S. Skulason, T. Szkopek, and M. Siaj, Chemical vapor deposition synthesis of graphene on copper with methanol, ethanol, and propanol precursors Carbon 49, 4204-4210, 2011.
2. *J. Guillemette*, S.S. Sabri, B. Wu, K. Bennaceur, P.E. Gaskell, M. Savard, P.L. Lévesque, F. Mahvash, A. Guermoune, M. Siaj, R. Martel, T.

Szkopek, and G. Gervais, Quantum Hall effect in hydrogenated graphene, Phys. Rev. Lett. 110, 176801, 2013.

3. *J. Guillemette*, S.S. Sabri, M. Savard, P.L. Lévesque, A. Guermoune, M. Siaj, R. Martel, G. Gervais and T. Szkopek, Magnetic Refrigeration with Doped Silicon, under review, 2013.
4. *J. Guillemette*, G. Gervais and T. Szkopek, Methods and Systems for Magnetic Solid State Cooling, US 61/652,931, provisional, 2012.

Portions of chapter six were published with the author of this thesis as the first author of the publication. Portions of chapter 5 are currently undergoing the review process. Finally, a manuscript based on the other portions of chapter 5 is in preparation.

## Contents

<b>1</b>	<b>Introduction</b>	<b>1</b>
1.1	Motivation . . . . .	1
1.2	From Graphene to Hydrogenated Graphene . . . . .	3
1.3	Thesis Organization . . . . .	10
<b>2</b>	<b>Review of Graphene and Hydrogenated Graphene Properties</b>	<b>12</b>
2.1	Historical Perspective . . . . .	12
2.2	Theories on disordered transport . . . . .	14
2.2.1	Metal Insulator Transitions . . . . .	15
2.2.2	Variable Range Hopping . . . . .	18
2.2.3	Ioffe-Regel Limit to Metallic Conductivity . . . . .	19
2.3	Quantum Hall Effect . . . . .	21
2.3.1	Classical Hall Effect . . . . .	21
2.3.2	Integer Quantum Hall Effect . . . . .	23
<b>3</b>	<b>Fabrication and Apparatus</b>	<b>31</b>
3.1	Graphene Fabrication . . . . .	32
3.1.1	Chemical Vapor Deposition Growth of Graphene . . . . .	32
3.1.2	Graphene Transfer . . . . .	33
3.1.3	Contacting, Slicing and Dicing . . . . .	35
3.2	Hydrogenated Graphene Fabrication . . . . .	37
3.2.1	Hydrogen Gun and Set-Up . . . . .	37
3.3	Experimental Apparatuses and Techniques . . . . .	40

<b>4</b>	<b>Characterization of the Hydrogenation Process</b>	<b>44</b>
4.1	Raman Spectroscopy . . . . .	44
4.1.1	Experimental Details about the Raman Systems . . . . .	45
4.1.2	Classification of Raman Peaks and Bands in Graphene . . . . .	46
4.1.3	Estimating Defect Density from Raman Spectra . . . . .	48
4.1.4	Single Point Raman Spectra . . . . .	50
4.1.5	Raman Maps . . . . .	51
4.2	From Raman to Transport . . . . .	56
4.3	Temperature Dependent Transport . . . . .	57
<b>5</b>	<b>Hydrogenated Graphene Based Thermometer and Bolometer</b>	<b>62</b>
5.1	Hydrogenated Graphene as a Thermometer . . . . .	64
5.1.1	Calibration . . . . .	64
5.1.2	Adiabatic Demagnetization Cooling . . . . .	68
5.2	Hydrogenated Graphene as a Bolometer . . . . .	71
5.2.1	Thermal Resistance Characterization . . . . .	74
5.2.2	Responsivity . . . . .	78
<b>6</b>	<b>Magnetoresistance of Hydrogenated Graphene</b>	<b>82</b>
6.1	Measured Samples . . . . .	83
6.2	Magnetoresistance in a Parallel High Magnetic Field . . . . .	85
6.3	Magnetoresistance in a Perpendicular High Field . . . . .	88
6.3.1	Quantum Hall Effect . . . . .	88
6.3.2	Differential Resistance ( $dV/dI$ ) in the Quantum Hall Regime . . . . .	94
6.3.3	Quantum Hall Effect and the Ioffe-Regel Limit . . . . .	97
<b>7</b>	<b>Conclusions and Future Work</b>	<b>100</b>
7.1	Conclusions . . . . .	100
7.1.1	Hydrogenated Graphene Characterization . . . . .	101
7.1.2	Applications . . . . .	102
7.1.3	Hydrogenated Graphene in a Magnetic Field . . . . .	103
7.2	Future Work . . . . .	104
	<b>Appendices</b>	<b>111</b>
	<b>References</b>	<b>113</b>

## List of Tables

2.1	Summary of differences between a 2DEGs and graphene for cyclotron frequency $\omega_c$ , energy dispersion $E_N$ and allowed fillings $N$ . . . . .	29
3.1	Summary of apparatuses used. . . . .	41
4.1	Summary of the position of the Raman Stokes shift at a pump wavelength of 514 nm with their commonly used label and scattering mechanism. . . . .	47
5.1	Summary of thermometers used in low temperature environments.	63
5.2	Summary of samples used in this chapter for fabrication of thermometers and bolometers. . . . .	65
6.1	Summary of the properties and measurements for the four samples measured in high fields. These all share a two point geometry.	84

## List of Figures

- 1.1 Material maps showing band gap *vs* lattice constant. A: band gap map for 2D materials. B: band gap map for 3D semiconductors. Only one alloy family in the 3D semiconductors is shown for clarity. The alloying line between graphene and graphane (CH) is shown on the left panel. . . . . 2
- 1.2 Important contributions concerning graphene since 2008: a) The fractional quantum Hall effect [1]. b) Discovery of the Hofstadter butterfly [2]. c) Its use as an analog transistor [3]. d) Sony mass producing 100 m rolls of graphene [4]. e) Samsung creating 30 inch sheets to be used as touch screens [5]. f) Graphene as an impermeable membrane [6]. g) Graphene used as a TEM grid [7]. . . . . 5
- 1.3 A: a single carbon atom's orbitals (taken from [8]). B: six carbon atoms of benzene bonded together via their  $sp^2$  orbitals forming  $\sigma$  bonds and their  $p$  orbitals hybridizing to form  $\pi$  bonds (taken from [9]). In an extended graphene structure, the  $\pi$  and  $\pi^*$  bonds constitute the valence and conduction bands respectively. . . . . 6
- 1.4 Atomic visualizations A: graphene, B: graphene with  $\approx 1\%$  hydrogen coverage, C: graphane (taken from [10]). . . . . 7
- 1.5 A: The density of states of a clean  $5 \times 5$  graphene sheet. B: The density of states of a  $5 \times 5$  atom graphene sheet with one hydrogen atom. The positive DOS (density of states) is for spin up and the negative DOS is for spin down. Taken from [11]. . . . . 8
- 1.6 Energy band diagrams for a) graphene and b) graphane. Taken from [12]. Calculations made using a tight binding model. . . . . 9

1.7	ARPES data showing the appearance of a mid gap state as hydrogen coverage is increased. a) ARPES intensities near the K point with the hydrogen coverage in white on the lower right corner of each subfigure. b) Photemission intensities showing the appearance of a hydrogen mid gap state [13]. . . . .	9
2.1	The graphitic allotropes of carbon [14]: graphene, graphite, buckminsterfullerene and nanotubes (clockwise). . . . .	14
2.2	A given material's density of states as function of energy. The grayed out region represents the mobility gap within which the carriers are localized [15]. . . . .	16
2.3	Sheet resistance versus temperature of a 2D Metal-Oxide-Semiconductor structure with $p$ type dopants where tuning the carrier density changes the temperature dependent sheet resistance (modified from [16]). . .	17
2.4	Conceptual representation of variable range hopping where transport takes place by hopping between localized states. . . . .	19
2.5	Schematic of the Hall Effect with the separation of charges and ensuing forces shown. Picture taken from [17]. . . . .	21
2.6	Longitudinal ( $U_{PP}$ ) and transverse ( $U_H$ ) voltages <i>vs</i> gate voltage at fixed magnetic field for an electron gas in a Si MOSFET at 1.5K [18]. Here, the quantum Hall effect is seen by the plateaux in $U_H$ . . .	24
2.7	A: conceptual representation of the formation of LLs in the bulk for both the sample (using the rotationally invariant symmetric gauge). B: the density of states. Taken from [17]. . . . .	25
2.8	Sample of width $w$ showing the bending of the LLs as they approach the confining potential of the edges. Only the states at the intersection of the LL and the Fermi level will contribute to transport along the edge. Taken from [17]. . . . .	26
2.9	A: $\rho_{xx}$ and $\sigma_{xy}$ as a function of carrier density for a graphene sample. Modified from [14]. B: Energy <i>vs</i> the density of states in the bulk of the sample when there is a plateau in $\sigma_{xy}$ (ii) or not (i). Modified from [14]. . . . .	30
3.1	Schematic of the CVD system used to grown graphene on copper from [19]. . . . .	33
3.2	Process flow for the fabrication of large area graphene samples on a silicon back-gate substrate. Picture taken from [19]. . . . .	35
3.3	Typical Hall bar shaped device on a G-10 carrier. . . . .	37
3.4	Hydrogen gun with the design inspired from [20] and the top image taken from [21]. . . . .	39

3.5	A: A sample exposed to an atomic hydrogen beam. The light originates from the white hot tungsten filament heated to $> 2000\text{K}$ . B: The two point resistance <i>vs</i> hydrogenation time taken <i>in situ</i> during the hydrogenation and an exponential fit to the curve. . . . .	41
3.6	Circuit diagram of a four point Van der Pauw measurement with a lock-in amplifier. A 100 mV RMS AC voltage is applied to a $10\text{M}\Omega$ resistor to source a current $I_x$ . The voltage $V_x$ is measured using differential input on an SRS 830 with $10\text{M}\Omega$ input impedance. . . . .	43
4.1	E-k diagrams of the Raman Stokes scattering process corresponding to the G, D, and G' peaks. Transitions are indicated by arrows, wherein: red arrows represent photon absorption, blue arrows represent phonon emission, purple arrows represent scattering by a defect potential, and green arrows represent photon emission. Modified from [22]. . . . .	46
4.2	Experimental Raman spectra from three different graphene samples bombarded by ions at a pump wavelength of 514 nm. A: Non-monotonic relationship between $I_D/I_G$ and the defect density $\lambda_D$ . B: Use of the D' peak to resolve ambiguity in determining $\lambda_D$ from $I_D/I_G$ . Taken from [23]. . . . .	50
4.3	Comparison of Raman spectra before (black) and after (red) hydrogenation. A: Hydrogenation time of 4 minutes with an extracted $\lambda_D \approx 4.5\text{nm}$ . B: Hydrogenation time of 15 minutes with an extracted $\lambda_D \approx 1.5\text{nm}$ . A vertical offset has been applied to the hydrogenated graphene spectra. . . . .	51
4.4	A typical fit of the D peak for one of the points making up the Raman map. The blue line is the baseline fit, the green line is the signal fit and the black line is the data. Data taken from the 12 minute hydrogenation sample. . . . .	52
4.5	Comparison of Raman maps where both the $x$ and $y$ axes are positions in $\mu\text{m}$ . These are from the same sample which was hydrogenated twelve minutes. A: Intensity of the D peak before hydrogenation. B: Intensity of the D peak after hydrogenation. C: Intensity of the G peak before hydrogenation. D: Intensity of the G peak after hydrogenation. The bottom left corner of maps C and D is a scratched off gold pad. The circles represent regions which have defects before hydrogenation. . . . .	53
4.6	Raman D/G ratio maps for samples hydrogenated six, eight, ten and fourteen minutes. All areas shown are $110$ by $225 \mu\text{m}^2$ . . . . .	55

4.7	Comparison of mean $I_D/I_G$ ratio from Raman maps in fig 4.6 as a function of hydrogenation times for different samples. The points are taken from Raman maps (RIMA) in fig 4.6 with a typical clean sample at zero minutes for comparison. Every point corresponds to an independent sample. . . . .	56
4.8	Two point resistance as a function of hydrogenation time. Measured <i>in situ</i> during the hydrogenation process at 300K with an exponential fit represented by the dashed line. . . . .	57
4.9	Two point resistance <i>vs</i> temperature in log-log scale of sample HG9. Three different gate voltages are shown: -40V (black), 0V (blue) and 50V (red), with the latter having the fewest charge carriers (the device is p-type). . . . .	58
4.10	Comparison of two point resistance <i>vs</i> temperature with the $x$ axis plotted as $T^{-1/3}$ on the left side and $T^{-1/2}$ on the right side. The gate voltage is 50V at the top and -40V at the bottom. The quality of the fit fails to distinguish whether a Mott or Efros-Shklovskii model applies in the temperature range explored. . . . .	59
4.11	Two point resistance <i>vs</i> temperature as a function of gate voltage of sample HG18. The inset shows the two point resistance as a function of gate voltage at 1.7K. There is evidence of a saturation regime at low carrier density at the lowest temperature. . . . .	60
5.1	Thermal sensitivity ( $-dR/dT$ at minimum temperature) <i>vs</i> temperature taken for all low temperature thermometers sold by Lakeshore compared to hydrogenated graphene. The GR series is doped germanium, RX is ruthenium oxide, and CX is zirconium oxy-nitride. . . . .	64
5.2	Resistance <i>vs</i> bias current of HG7 at 300 mK on a subsequent cooldown. Sourcing currents of 10, 20 and 50 nA show no signs of self heating (blue region). The sourcing currents in the red region show signs of self heating. . . . .	66
5.3	A: Calibration of R <i>vs</i> T at B = 0 T. B: Calibration of R <i>vs</i> B at T = 300 mK. C: Calibration of the hydrogenated graphene thermometer in both T and B. The device measured is HG7. . . . .	67
5.4	Dynamic magnetoresistance with sweep rate at 0.225 T/min (blue) with the steady state values (red). The grey arrows represent the order in which the magnetic field was swept. The device measured is HG7. . . . .	69
5.5	Magnetoresistance (black) with the steady state value (blue). The sweep rate is 0.225 T/min. The device measured is HG7. . . . .	70

5.6	Dynamic cooling of the demag stage at different temperatures. The sweep rate is 0.225 T/min. The device measured is HG7. . . . .	71
5.7	Schematic of the sample being exposed to incoming radiation and the various channels through which heat can be dissipated. . . . .	75
5.8	$R_{2pt}$ of four devices as a function of temperature. The carrier density was minimized for each sample. . . . .	75
5.9	Extracted electron temperature <i>vs</i> applied electrical power for HGD5 with base temperature 9.8K. . . . .	76
5.10	$R_{th}$ <i>vs</i> temperature for all devices. . . . .	77
5.11	A: Responsivity <i>vs</i> impinging global power at 10 K with 9 $\mu$ W of incident power for HGD2. B: Responsivity <i>vs</i> cryostat temperature with 25 $\mu$ W of incident power for HGD2. . . . .	79
5.12	Comparison of responsivity (black) and $dR/dT$ (blue) as a function of two point resistance at 10K for the three surviving devices. . . . .	80
6.1	Resistance $R_{2pt}$ <i>vs</i> temperature for different gate voltages $V_G$ of sample HG-33. The inset shows the resistance $R_{2pt}$ <i>vs</i> gate voltage $V_G$ at the base temperature of 1.7 K. . . . .	85
6.2	A: Resistance $R_{2pt}$ <i>vs</i> gate voltage for a perpendicular magnetic fields for sample HG-18. B: Resistance $R_{2pt}$ <i>vs</i> gate voltage for a parallel magnetic field for sample HG-18. The parallel magnetic field increases the resistance plateau and the perpendicular one reduces the resistance plateau. All data was taken at $\approx 300$ mK. . . . .	86
6.3	Normalized two point resistance $R_{2pt}$ <i>vs</i> parallel magnetic field for different gate voltages $V_G$ for sample HG-18. The low carrier densities exhibit no change in resistance as a function of parallel magnetic field in contrast to the high carrier densities. Data was taken at $\approx 300$ mK. Both sweep directions are plotted. . . . .	87
6.4	Normalized two point resistance $R_{2pt}$ <i>vs</i> parallel magnetic field at -60V gate voltage for different temperatures for sample HG-18. Increasing the temperature reduces the positive magnetoresistance. Both sweep directions are plotted. . . . .	88
6.5	Resistance $R_{2pt}$ <i>vs</i> perpendicular magnetic field and gate voltage at $\approx 550$ mK for sample HG-33. . . . .	90
6.6	Resistance $R_{2pt}$ <i>vs</i> hole density (lower ordinate) or gate voltage (higher ordinate) at 45 T for sample HG-33 from [24]. The density was estimated by using a parallel plate capacitor model and the charge neutrality point was taken to be the gate voltage about which the curve is symmetric. Data was taken at $\approx 550$ mK. . . . .	91

- 6.7 A: Resistance  $R_{2pt}$  vs gate voltage for 0 T, 17.5 T and 45 T for sample HG-33. The voltage distance between the charge neutrality point and when the resistance falls below  $6.25 \text{ M}\Omega$  is plotted on the bottom and converted to carrier density. B: Localized carriers vs magnetic field in units of both carrier density and width of the plateau in gate voltage for sample HG-33. The two are related via  $n = \epsilon V_g / t_{ox} q$  where  $n$  is carrier density,  $\epsilon$  the permittivity of  $\text{SiO}_2$  and  $t_{ox}$  the oxide thickness. Data was taken at  $\approx 550 \text{ mK}$ . . . . . 93
- 6.8 Resistance  $R_{2pt}$  of sample HG33 at 21 V gate voltage vs both the magnetic field (lower ordinate) and magnetic length,  $l_B$  (upper ordinate). The shaded region indicates the estimated point defect spacing extracted from the Raman spectra from [24]. Data was taken at  $\approx 550\text{mK}$ . . . . . 94
- 6.9 Two point resistance as a function of gate voltage for HG-33 at 45 T. The labels show the positions at which the  $dV/dI$  experiments were performed. Data was taken at  $\approx 550\text{mK}$ . . . . . 96
- 6.10 Normalized two point differential resistance  $dV/dI$  vs applied DC bias at different gate voltages and magnetic fields for sample HG-33. Data was taken at  $\approx 550\text{mK}$ . Both sweep directions are plotted. . . 96
- 6.11 Ioffe-Regel Wigner-Seitz diagram for the main families of materials exhibiting the quantum Hall effect. The figure shows the zero-field value of the Ioffe-Regel disorder parameter  $(k_F \lambda)^{-1}$  plotted vs the Wigner-Seitz radius, both dimensionless, for the main 2DEG families in which the integer and fractional quantum Hall effect were observed. A brief description of the material system, indexed numerically, is given in the upper right. The size of the labeled regions is representative of the parameter range from observed mobilities and densities. The dashed line shows the Ioffe-Regel limit where  $k_F \lambda = 1$ . The Wigner crystal (WC), thought to occur at large  $r_s$  and low disorder, is highlighted in green. Taken from [24]. . . . . 98
- 7.1 Measurement of the band gap of the compound as a function of the mole fraction of cadmium. These measurements are taken with optical absorption and magneto-optical measurements at 80K. Graph from [25]. . . . . 107

- 7.2 Proposed evolution of the energy band diagram as more disorder is introduced. In i), we have the density of states of a pristine graphene sheet. In ii) a gap opens and localized states appear. Mid gap states associated with dangling bonds are generated by isolated hydrogenation sites. iii) A fully hydrogenated graphene, meaning graphane, is anticipated to be a gapped system with no mid gap states because there are no dangling bonds. The green region corresponds to states that are localized. Band diagrams taken from [12] . . . . . 109
- 1 Shadow mask used to make a Hall bar geometry on a sample. The mask material is molybdenum and its thickness is  $\approx 1$   $\mu\text{m}$ . 112

## Introduction

### 1.1 Motivation

The invention of the transistor by Bardeen, Brattain and Shockley at Bell Labs in 1947 launched solid state electronics. Significant improvements were made to bulk 3D semiconductors used in the electronics industry: the purity of materials, the control over dopant concentrations, the formation of alloys and the creation of heterostructures by molecular beam epitaxy (MBE) or by metalorganic chemical vapor deposition (MOCVD). From these technical advances, quantum confinement of electrons has led to the widespread study of two dimensional electron gases (2DEGs). More recently, 2D atomic crystals were isolated and found to be advantageous because of their high mobility and their presence on the surface of a substrate which facilitates surface analysis and modification. The overarching goal of this thesis is to make use of adatoms in a 2D atomic crystal to tune its properties, specifically, the chemical bonding of hydrogen adatoms on a graphene sheet to create  $\text{CH}_x$  and open a band gap.

The ability to isolate and electrically measure various intrinsically 2D materials in the past few years has allowed a new band gap map to emerge. Compound semiconductors such as GaAs and AlGaAs can be alloyed to form  $\text{Al}_x\text{Ga}_{1-x}\text{As}$ , whereby the distribution of Al is random within the crystal. This alloying allows for an extension of the properties of the elementary and binary semiconductor compounds to enable a tuneable band gap. The process of adding hydrogen atoms to the graphene can be considered as alloying. Notably, this process is unlike doping because hydrogen atoms do not replace carbon atoms. Rather, the graphene is alloyed between C and graphane *i.e.* a fully hydrogenated graphene, or CH and the end result is an organic compound.

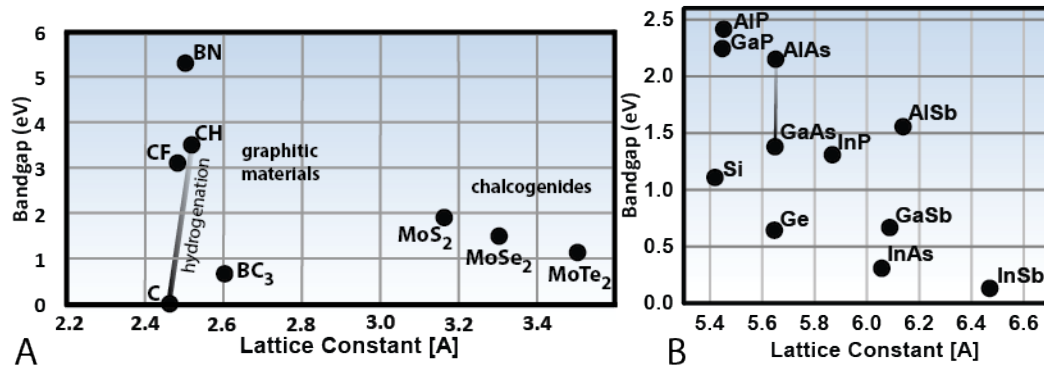


**Fig. 1.1:** Material maps showing band gap *vs* lattice constant. A: band gap map for 2D materials. B: band gap map for 3D semiconductors. Only one alloy family in the 3D semiconductors is shown for clarity. The alloying line between graphene and graphane (CH) is shown on the left panel.

The right panel of fig 1.1 shows common materials used in modern electronics for the fabrication of HEMTs, solar cells and LEDs. The left panel of fig 1.1 shows a similar map, but for intrinsically 2D materials. In this thesis,

the emphasis will be on probing hydrogenated graphene ( $\text{CH}_x$ ) where  $x$ , the hydrogen concentration, is no greater than 5%. By tuning the hydrogen content on the alloying line between graphene and graphane, band gap tunability should be achievable. Furthermore, tailoring the hydrogen adatom coverage will allow a study of the impact of disorder, in the form of hydrogen adatoms modifying the electronic properties of the material.

The three goals of this thesis are:

1. From the perspective of material synthesis, to characterize the mechanism of the hydrogenation process and its impact on electronic transport.
2. From the perspective of device applications, to use the localization of carriers in graphene due to hydrogenation to realize a proof of concept thermometer and bolometer.
3. From the perspective of condensed matter physics, to use this 2D material to analyze the impact of disorder on the magnetotransport of hydrogenated graphene.

## **1.2 From Graphene to Hydrogenated Graphene**

In 2004, Andre Geim and Konstantin Novoselov from the University of Manchester, were the first to isolate graphene by mechanical exfoliation [26]. They were awarded the Nobel Prize in physics in 2010 *for groundbreaking experiments regarding the two dimensional material graphene*. Their seminal paper demonstrated that graphene could be used as an ambipolar field effect transis-

tor and Shubnikov-de Haas oscillations suggested that the quantum Hall effect was within reach. The future Nobel laureates showcased many of graphene's unique properties [27] such as, the relativistic behavior of Dirac fermions, the fourfold degenerate quantum Hall effect and the anomalous first plateau at  $\nu = \pm 2$ , as well as the non trivial Berry phase  $\beta = 0.5$ . Graphene's linear dispersion and true 2D nature have opened the door to many discoveries such as the observation of fractional quantum hall states in graphene [1, 28, 29] and the experimental observation of the Hofstadter butterfly, *one of the first quantum fractals in physics* [2]. Advances were also made on the material fabrication front such as Samsung fabricating 30 inch screens made of graphene films by using roll to roll production [5]. More recently, 100 m graphene screens were fabricated by Sony [4]. Further work has shown that graphene could be an ideal TEM grid material [7]. Graphene's mechanical properties are also interesting, as demonstrated by its tensile modulus of 1TPa [30, 31]. Finally, from the perspective of electronics, it would be surprising if, at this moment, graphene could replace current silicon MOSFETs. While IBM has demonstrated that graphene has a large threshold frequency (100 GHz)[3], it nevertheless lacks a band gap and the absence of saturation prevents it from reaching the cut-off frequency obtained for silicon ( $\approx 500$  GHz) [32]. As of now, graphene has become so omnipresent that even the tennis racquet company Head has started incorporating graphene into the shaft of their latest racquet in order to reduce weight while increasing strength [33].

On a different front, a small number of research groups have focused on the electronic properties of the chemical derivatives of graphene such as fluorinated

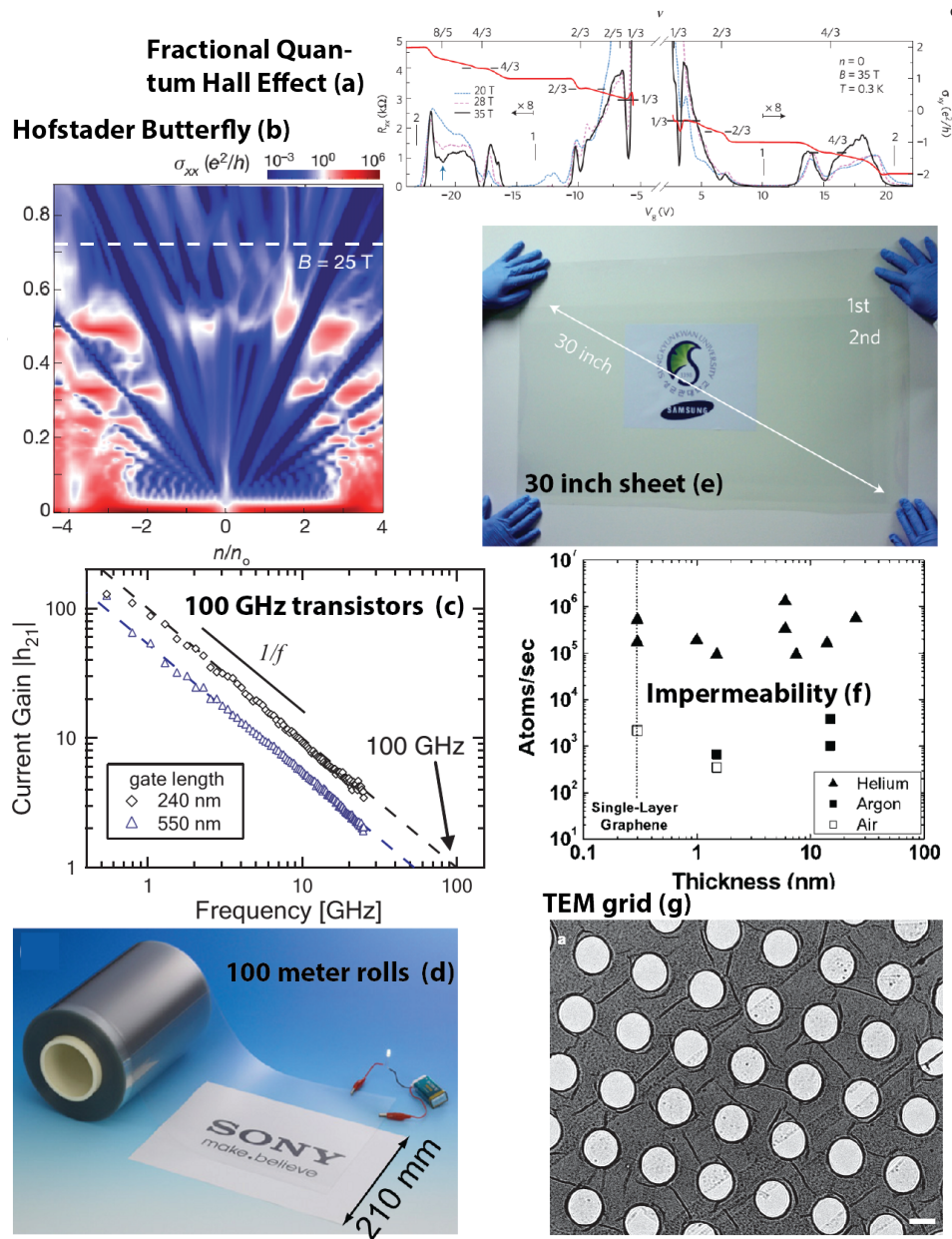


**Fig. 1.2:** Important contributions concerning graphene since 2008: a) The fractional quantum Hall effect [1]. b) Discovery of the Hofstadter butterfly [2]. c) Its use as an analog transistor [3]. d) Sony mass producing 100 m rolls of graphene [4]. e) Samsung creating 30 inch sheets to be used as touch screens [5]. f) Graphene as an impermeable membrane [6]. g) Graphene used as a TEM grid [7].

graphene [34, 35, 36], graphene oxide [37, 38] and what is of interest in this thesis, hydrogenated graphene [39, 40, 41, 42, 24]. Hydrogenated graphene is an ideal material to study disorder in 2D. In 2DEGs, the confinement energy of the carriers is limited by the band offset energies (100's of meV) as opposed to graphene where the carriers are confined by the work function ( $\approx 4.5$  eV). This difference gives graphene an inherent advantage for studying disorder in two dimensions, wherein a large disorder potential can be introduced without loss of carrier confinement. The ability to use Raman spectroscopy to infer defect spacing is one more asset that graphene has over buried 2DEGs. Furthermore, by adding hydrogen, the simplest atom, it simplifies the theoretical calculations required to predict the band structure of this compound material. To understand what happens when hydrogen is added to graphene, the starting material's electronic orbital picture is shown in fig 1.3 as well as the chemical bonding picture in fig 1.4.

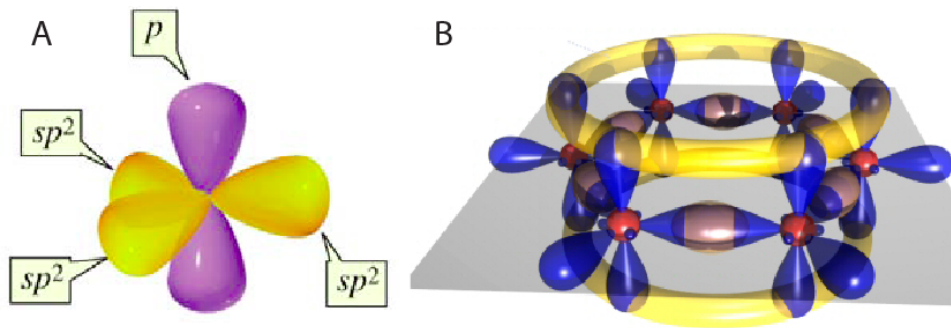


**Fig. 1.3:** A: a single carbon atom's orbitals (taken from [8]). B: six carbon atoms of benzene bonded together via their  $sp^2$  orbitals forming  $\sigma$  bonds and their  $p$  orbitals hybridizing to form  $\pi$  bonds (taken from [9]). In an extended graphene structure, the  $\pi$  and  $\pi^*$  bands constitute the valence and conduction bands respectively.

From the perspective of chemical bonding, the addition of a hydrogen atom in the right panel of fig 1.3 localizes one electron, creating a covalent bond and

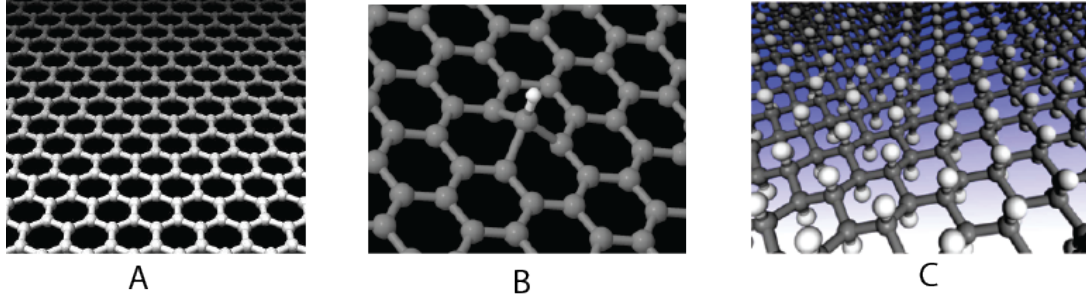


**Fig. 1.4:** Atomic visualizations A: graphene, B: graphene with  $\approx 1\%$  hydrogen coverage, C: graphane (taken from [10]).

leaving each of the three neighboring carbon atoms short by  $1/3$  of a  $\pi$  bonded  $p_z$  orbital. These three neighboring atoms have incomplete dangling bonds arising from their lack of  $1/3$  of a partner  $p_z$  electron. By having the  $1s$  hydrogen electron bond with the  $p_z$  electron of the carbon atom, the carbon atom re-organizes its structure from  $sp^2$  to  $sp^3$ . Theoretical calculations for hydrogenated graphene cells [11], as well as graphene sheets with missing carbon atoms, which is similar to removing a  $p_z$  electron [43, 44], have shown the emergence of a mid gap state. This can be seen in fig 1.5, and the mid gap state can be identified with the dangling  $p_z$  orbital states.

From the perspective of band theory, the hydrogen atoms should, in principle, be considered as a neutral point defect that acts as a short range scatterer. Conceptually, breaking the translational invariance, even on only one site, will also affect the band structure. The breaking of translational invariance with a point defect will prevent the states that have the greatest spatial extent (*i.e.* the smallest  $k$  vectors) from contributing to transport. Therefore, it is expected that, rather than having a linear band crossing at the Dirac point, there may be a slight curvature in the dispersion and the formation of a very

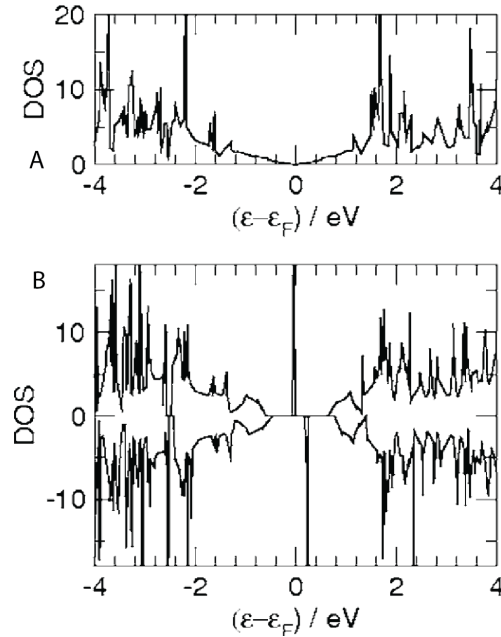


**Fig. 1.5:** A: The density of states of a clean 5 x 5 graphene sheet. B: The density of states of a 5 x 5 atom graphene sheet with one hydrogen atom. The positive DOS (density of states) is for spin up and the negative DOS is for spin down. Taken from [11].

small impurity induced gap. The level crossing of a Dirac cone is effectively modified by into an anti-crossing by the symmetry breaking potential of the point defect.

In the words of Herb Kroemer *If, in discussing a semiconductor problem, you cannot draw an energy band diagram, you do not know what you are talking about. If you can draw it, but don't, then your audience won't know what you are talking about* [45]. The energy band diagrams of both graphene and graphane are shown in fig 1.6. Note that the Dirac cone disappears and the band minima shifts from the K and K' points to the  $\Gamma$  point.

Experimental data from angle resolved photoemission spectroscopy (ARPES)

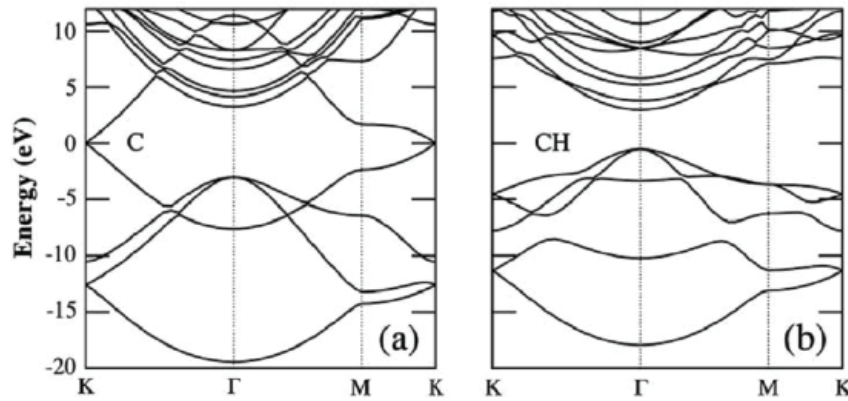


**Fig. 1.6:** Energy band diagrams for a) graphene and b) graphane. Taken from [12]. Calculations made using a tight binding model.

[13] are shown in fig 1.7, giving the evolution of the energy band diagram near the K point as a function of hydrogen coverage up to  $\approx 2\%$ .

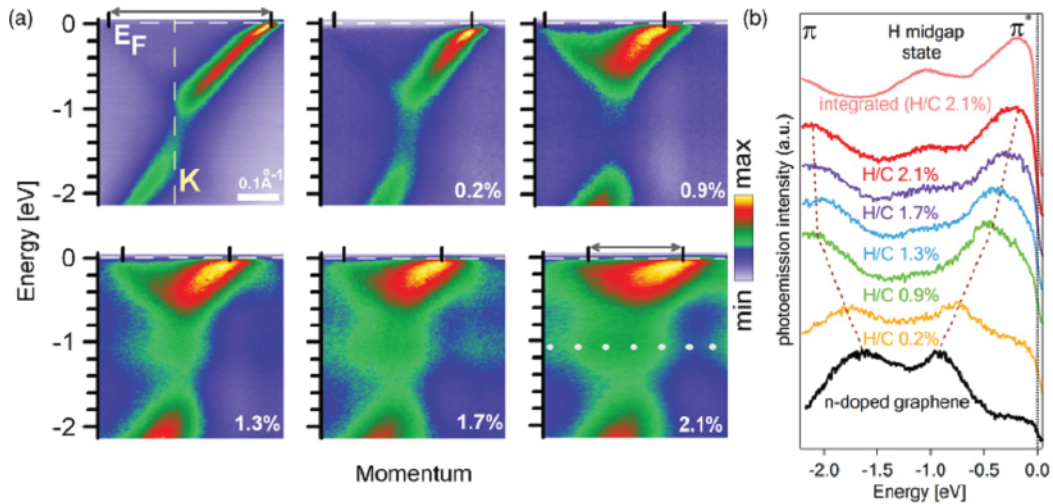


**Fig. 1.7:** ARPES data showing the appearance of a mid gap state as hydrogen coverage is increased. a) ARPES intensities near the K point with the hydrogen coverage in white on the lower right corner of each subfigure. b) Photomission intensities showing the appearance of a hydrogen mid gap state [13].

As the hydrogen coverage is increased, ARPES data suggests that a mid gap states will form an impurity band, as shown in fig 1.7 B. The ARPES

results do not provide direct information concerning localization effects and requires electron transport measurements such as those presented in chapter four [13].

Naively, the density of point defects at which scattering ceases to be well described as a perturbation is  $k_F^2$ , where  $k_F$  is the Fermi wavevector of the electron gas. This limit is called the *Ioffe-Regel limit* to metallic conduction and will be explored in detail in a later section. Verifying this conceptual picture will be one of the aims of this thesis.

### 1.3 Thesis Organization

The thesis will proceed as follows:

Chapter 2: A brief historical perspective of graphene will be presented. An overview of the current picture of disorder in 2D will be presented along with an introduction to the integer quantum Hall effect. This chapter ensures the reader will have the proper theoretical basis to understand the experiments performed in chapters 4, 5 and 6.

Chapter 3: A complete picture of the fabrication of chemical vapor deposition grown graphene on copper foils. The transfer process, the mounting to headers and the hydrogenation process will be explained. Finally, the various experimental set-ups on which the measurements in chapters 4, 5 and 6 were performed will be presented.

Chapter 4: An experimental introduction to hydrogenated graphene by analyzing Raman spectra and temperature dependent transport as a function

of hydrogenation level.

Chapter 5: The applications of hydrogenated graphene as a thermometer and a bolometer will be shown. Principles of operation and comparisons to existing technologies will be included.

Chapter 6: An analysis of the magnetotransport of hydrogenated graphene. The colossal negative magnetoresistance of hydrogenated graphene that led to the emergence of the  $\nu = -2$  quantum Hall state will be explained as well as its magnetoresistance in a parallel field set-up. This is the most disordered samples to date on which the quantum Hall effect has been measured.

Chapter 7: This will summarize the conclusions of the previous three chapters and highlight exciting directions for future work.

## **Review of Graphene and Hydrogenated Graphene Properties**

### **2.1 Historical Perspective**

Graphite was discovered in 1565 in England as a means to mark animals or even paper. It is only one hundred years later that graphite was molded into cylindrical shapes and made into pencils. During all these years, it was mistakenly believed that this black material was composed of lead. In 1779, Carl Scheele discovered that this black lead as it was called, was in fact carbon. During the same decade, Antoine Lavoisier discovered that diamond was also another form of carbon. Not unlike the desire of alchemists to produce gold from other metals, this decade launched several searches for ways to convert black lead into diamond. Confirmation of the crystallographic properties of diamond and graphite happened in 1924 when John Bernal [46] used the technique of X-ray diffraction which had just been invented by his PhD advisor, William Bragg. These measurements confirmed the hexagonal structure of the lattice, measured the interplane distance, as well as the lattice constant. Us-

ing known data regarding graphite, Phil Wallace ventured in 1947 to calculate the charge carrier densities for varying thicknesses of graphite and obtained a peculiar linear dispersion for a single sheet of graphite [47]. This was in the same year the transistor was invented by John Bardeen, Walter Brattain and Bill Shockley at Bell Laboratories. The next allotrope of carbon to be discovered was the 0D variant: the fullerene, or bucky ball, was synthesized in 1985 and observed by Kroto *et al.* [48]. However, the size of a single fullerene was too small in all three dimensions to turn it into a device and so attention was turned towards making the 1D allotrope of carbon: nanotubes (CNTs). At the beginning of the 1990s, Sumio Iijima and his team at NEC ignited interest in CNTs by inventing a repeatable method of fabricating them [49]. This interest grew when it was discovered that they exhibit the electric field effect in 1998 [50, 51]. By then, the 0D, 1D and 3D variants of carbon had all been discovered, and only the 2D variant remained. A chemist by the name of Hans-Peter Boehm coined the term graphene in 1962 to represent the 2D variant while he was himself working on creating it by using oxidized graphite [52]. By 1997, ultrathin layers of graphite and hexagonal boron nitride (h-BN) were grown on TiC, Ni, Pt, Ir, Pd and Ru [53].

In 2004, Andre Geim and co-workers at the University of Manchester isolated and measured the optical and electronic properties of a single sheet of carbon atoms by using the scotch tape method. Geim and Novoselov won the Nobel prize in physics in 2010 *for groundbreaking experiments regarding the two-dimensional material graphene.*

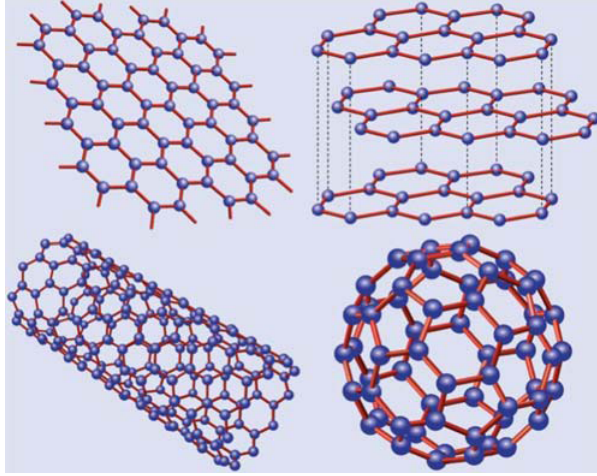


**Fig. 2.1:** The graphitic allotropes of carbon [14]: graphene, graphite, buckminsterfullerene and nanotubes (clockwise).

## 2.2 Theories on disordered transport

This section will provide a conceptual basis to understand the physical mechanisms behind electronic transport in disordered media. Using theoretical concepts established by Phil Anderson and Nevill Mott, a qualitative description of the temperature dependent transport in hydrogenated graphene is presented in chapter four.

Hydrogenated graphene, as well as other functionalized variants of graphene, are ideal physical systems to study electron transport in 2D. Disorder in 2D systems is simpler to study if carriers are confined to a single 2D sub-band, as is the case in graphene owing to the atomic layer carrier confinement with a confinement potential of  $\approx 4.5$  eV. This is contrast with the confinement potential of 2DEGs in conventional semiconductor heterostructures ( $\approx 100$ 's meV). In the following sections, the topics reviewed are: metal insulator transitions

(MIT), variable range hopping (VRH) and the Ioffe-Regel limit to metallic conductivity.

### 2.2.1 Metal Insulator Transitions

In 1977, Sir Nevill Mott, John Hasbrouck van Vleck and Phil Anderson shared the Nobel prize in physics *for their fundamental theoretical investigations of the electronic structure of magnetic and disordered systems* [54, 55]. By finding a way to theoretically study disorder in a lattice and predict experimental manifestations, a new path was opened: disorder mediated transport modifications. Recall that an experimental trait to distinguish a metal from an insulator is the temperature dependence of the resistance. Regardless of dimensionality, metals can be defined by the condition  $dR/dT > 0$  and insulators by  $dR/dT < 0$ . From the theoretical perspective of the Ioffe-Regel limit to metallic conductivity, as  $T \rightarrow 0\text{K}$ , metallic 2D systems should have a sheet resistance below the quantum of resistance  $h/e^2$  per square and insulating systems should exhibit  $R \rightarrow \infty$ . A caveat to the distinction between metal and insulator is that in 2D systems, the behavior is never truly metallic [56]. More precisely, for metallic 2D systems,  $dR/dT \approx 0$  as experimentally observed in graphene samples [39].

To formalize what is meant by an insulator, it is important to clarify the different theoretical models of a *band insulator*, an *Anderson insulator* and a *Mott insulator*. One difference is that the former two arise due to electron-ion interactions and the latter is due to electron-electron interactions [57]. The band insulator is most commonly encountered in solid state electronics and is

what is usually meant when speaking of insulators. It also explains the gap in density of states between the valence and conduction bands arising from electron interactions with the periodic ion potential of a crystal. The Anderson insulator arises from the presence of randomly placed defects and is characterized by the localization of states that lie at energies beneath the mobility edge (see fig 2.2) which are the states in the shadowed region. Notice that the states are still present, but they are localized and cannot contribute to conduction. The criterion for Anderson localization is usually written as  $N_d^{1/3} a_B \approx 0.25$  in three dimensions [15]. In other words, when the mean defect spacing ( $N_d^{1/3}$ ) is comparable to the effective Bohr radius ( $a_B$ ), the carriers are considered to be Anderson localized. As the carrier density is modified, it is possible to go from localized states to extended states and thus from a metallic phase to an insulating phase.

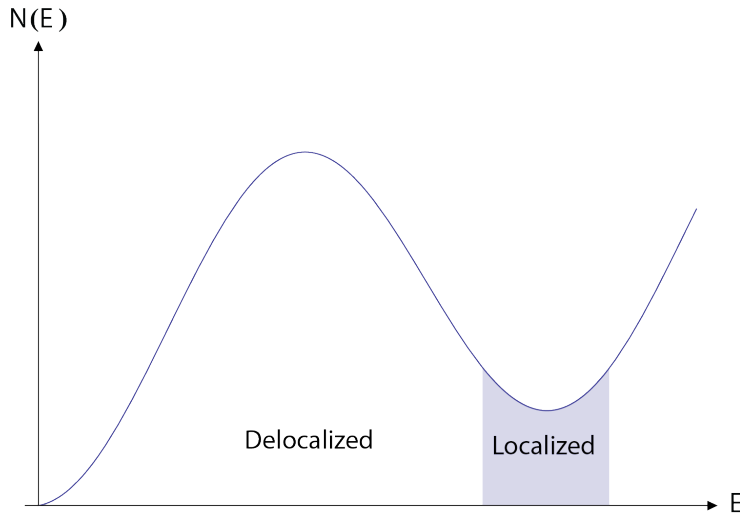


**Fig. 2.2:** A given material's density of states as function of energy. The grayed out region represents the mobility gap within which the carriers are localized [15].

Mott insulators come about from many body interactions of the electrons

in the system. However, no feature of temperature dependent transport can distinguish between Mott insulators or Anderson insulators [58].

In the example shown in fig 2.3, it is the ratio of the carrier density to defect density that determines whether the system will behave as a metal or an insulator. As a consequence of the complexity of determining the nature of the insulator from temperature dependent transport, the authors of this paper would not venture to specify the type of insulating state observed.

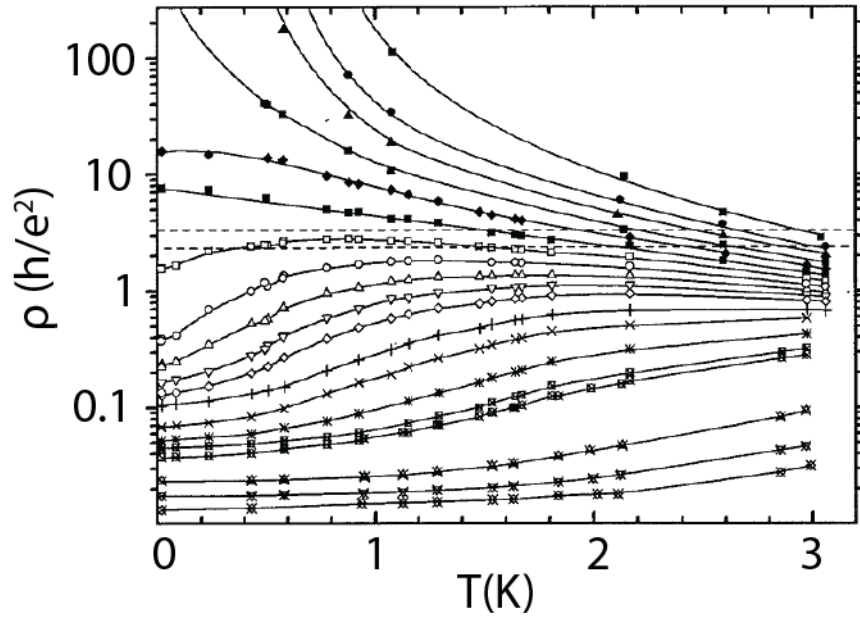


**Fig. 2.3:** Sheet resistance versus temperature of a 2D Metal-Oxide-Semiconductor structure with  $p$  type dopants where tuning the carrier density changes the temperature dependent sheet resistance (modified from [16]).

### 2.2.2 Variable Range Hopping

Both of the models brought forward by Anderson and Mott take a density of states approach to the problem. However, as experimentalists, there is considerable interest in having a signature in the resistance versus temperature data so as to unambiguously determine the nature of charge carrier localization. There are several theories that attempt to explain the behavior of the resistance as a function of temperature: Mott variable range hopping (VRH), Efros-Shklovskii variable range hopping (ESVRH) and Arrhenius thermal activation. These three types of transport have the same general formula,

$$\sigma = \sigma_0 \cdot e^{-(T_0/T)^{1/n}}, \quad (2.1)$$

where  $n$  in Eq 2.1 will be  $d+1$  for VRH (where  $d$  is the dimensionality of the system), 2 for ESVRH and 1 for Arrhenius thermal activation [59, 60, 15, 61] and  $T_0$  is the activation temperature. In the simplest case of Arrhenius thermal activation,  $T_0$  can be associated to a well defined energy gap for carrier excitation as in an intrinsic semiconductor (an ideal band insulator). Note that these models apply only to 2D and 3D conductivity.

Fig 2.4 depicts a cartoon showing that variable range hopping can be thought of as charge carriers inside the mobility gap being localized with transport occurring by hopping from localized state to localized state. Variable range hopping does not have localized states hop to non-localized states as would be the case with thermally assisted transport where  $n = 1$ . The interaction be-

tween electrons and phonons is thought to be the mechanism by which the carriers will hop between localized states. However, some experimental results suggest that electron-electron interactions may also be at play [62]. The hopping mechanism replaces the more common band conduction mechanism because disorder is so high that the mean free path of diffusive transport becomes an ill defined concept and thus the conceptual picture of conduction should be modified.

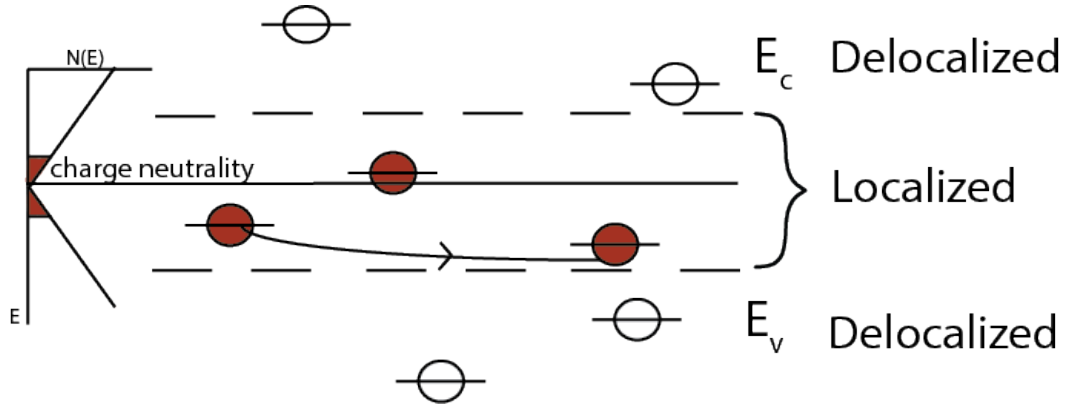


**Fig. 2.4:** Conceptual representation of variable range hopping where transport takes place by hopping between localized states.

The Efros-Shklovskii VRH model also takes into account Coulomb interactions between charge carriers [61]. The most important consequence of ES-VRH is that the temperature dependent resistance is now independent of the dimensionality of the system.

### 2.2.3 Ioffe-Regel Limit to Metallic Conductivity

Another perspective on the distinctions between insulators and metals is the *Ioffe-Regel limit* to metallic conductivity. The conceptual picture is if a

## 20 Review of Graphene and Hydrogenated Graphene Properties

minimum charge carrier mean free path ( $\lambda_{tr}$ ) exists, then there must be a minimum to band conduction. At the Ioffe-Regel limit, the Fermi wavelength  $\lambda_F$  is the minimum mean free path and so if the transport mean free path is smaller than the Fermi wavelength, the material will no longer be a metal. In other words, the Ioffe-Regel parameter establishes a dimensionless number given by  $\lambda_{tr}k_F$ , where  $k_F = 2\pi/\lambda_F$ . For a material to be considered a metal, the condition  $\lambda_{tr} \geq \lambda_F$  (with the appropriate constant), factor must be satisfied. This criterion is somewhat analogous to the criterion for Anderson localization ( $N_d^{1/3} a_B \approx 0.25$ ) that relates the defect spacing to the effective Bohr radius. The critical value of the Ioffe-Regel parameter for the transition from metallic to insulating conduction occurs when the mean free path is comparable to the Fermi wavelength. Using the Büttiker expression for conductivity in 2D, the sheet conductance is  $\sigma_{2D} = \frac{e^2}{h} \cdot \frac{g}{\pi} \cdot \frac{\lambda_F}{\lambda_{tr}}$  where  $g$  is the degeneracy (spin and valley). Applying the condition at the interface between metallic and insulating ( $\lambda_{tr} = \lambda_F$ ), the minimum metallic sheet conductance becomes the quantum of conductance ( $e^2/h$ ) to within a numerical constant and degeneracy  $g$ .

Since neither a Fermi wavelength nor a mean free path can be defined in an insulating transport regime where variable range hopping between localized states describes conduction rather than diffusive band conduction, care must be taken in defining a value of the Ioffe-Regel parameter in the insulating phase. One can define the Ioffe-Regel parameter as a ratio of measured sheet conductance to the conductance quantum, with the caveat that the parameter is only an approximate indicator of disorder [63].

## 2.3 Quantum Hall Effect

### 2.3.1 Classical Hall Effect

This section briefly reviews the origins of the quantum Hall effect, and includes a discussion on the effects of disorder. To comprehend the results shown in chapter six, a brief review of the quantum Hall effect in typical 2DEGs and graphene is presented.

During his PhD studies at Harvard, Edwin Hall discovered the effect that now holds his name. The Hall effect is the difference in potential developing transverse to the path of an electrical current when a magnetic field applied perpendicular to the plane of the current. Any build up of voltage in the transverse direction is commonly referred to as Hall voltage ( $V_H$ ) and is a consequence of the Lorentz force  $F_B$  on the charge carriers,

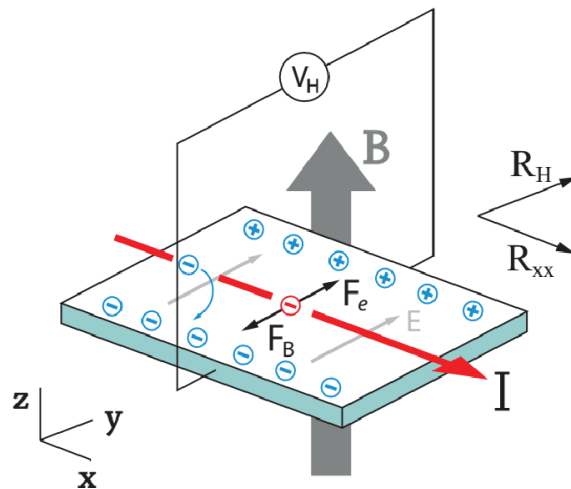


**Fig. 2.5:** Schematic of the Hall Effect with the separation of charges and ensuing forces shown. Picture taken from [17].

$$\vec{F}_B = q (\vec{v} \times \vec{B}). \quad (2.2)$$

Here,  $q$  is the charge of the carrier,  $\vec{v}$  the velocity of the carriers and  $\vec{B}$  is the magnetic field. Whether charges are electrons (-) or holes (+), the Lorentz force will segregate the positive or negative charges on the same side of the sample. In turn, this separation will cause an electric field to be created in the direction transverse to the current. The resulting electrostatic force is given by

$$|\vec{F}_e| = \frac{qV_H}{w}, \quad (2.3)$$

where  $V_H$  is the Hall voltage across the sample and  $w$  is the width of the sample. The sign of the electrostatic force, and hence the Hall voltage, will thus depend on the carrier type. Upon reaching equilibrium, the electrostatic force will balance the Lorentz force,

$$\frac{eV_H}{w} = qv_d B. \quad (2.4)$$

In order to simplify the expression for Hall voltage, one can use  $I = nqv_d w$  where  $n$  is the area charge density and  $v_d$  is the charge drift velocity. Combining this equation and 2.4, a simpler expression for the Hall voltage yields,

$$V_H = \frac{IB}{nq}. \quad (2.5)$$

A typical way to report this quantity is to consider the Hall or transverse

resistance which is obtained by dividing both sides by  $I$  so as to obtain  $R_{xy}$  or  $R_H$  as shown in eq. 2.6,

$$\frac{V_H}{I} = R_{xy}. \quad (2.6)$$

Therefore, if the contacts permit it, one can measure the longitudinal resistance ( $R_{xx}$ ) as well as the transverse resistance ( $R_{xy}$ ) when a magnetic field is applied. There are many devices used today that operate using the Hall effect such as magnetic field sensors and current sensors. This effect is a sensitive way to measure changes in either of these two quantities.

### 2.3.2 Integer Quantum Hall Effect

In a seminal paper presented in 1980, Klaus von Klitzing measured the Hall resistance in a silicon MOSFET (metal oxide semiconductor field effect transistor) and found that its values were quantized in units of  $h/e^2$  (25813  $\Omega$ ) at 1.5K [18]. In 1990, the National Institute of Standards and Technology (NIST) adopted the quantum of resistance  $h/e^2$  as the primary definition of resistance since it can be related to the fundamental units  $h$  and  $e$ .

The sample geometry of Klitzing's MOSFET is shown on the top right of fig 2.6. The source and drain contacts are used for sourcing current and all the other contacts are designed to measure voltage in either the longitudinal or transverse directions (Hall bar geometry). Two key observations are made from the data in fig 2.6: the plateaus in transverse voltage are quantized and the longitudinal voltage drops to zero for these plateaus in the Hall voltage.

Recall that the motion of charged particles under a perpendicular magnetic

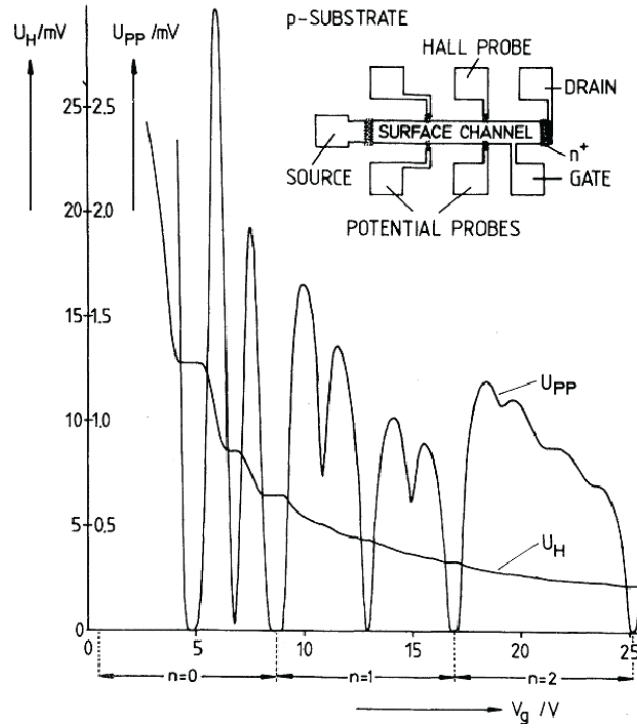


**Fig. 2.6:** Longitudinal ( $U_{PP}$ ) and transverse ( $U_H$ ) voltages *vs* gate voltage at fixed magnetic field for an electron gas in a Si MOSFET at 1.5K [18]. Here, the quantum Hall effect is seen by the plateaux in  $U_H$ .

field is a circular orbit called a cyclotron orbit, with a cyclotron frequency,

$$\omega_c = \frac{qB}{m^*}, \quad (2.7)$$

where  $m^*$  is the effective mass of the charge carriers. These cyclotron orbits can only take on specific energy levels, per the solution given by solving the Schrödinger equation for carriers in 2D with a vector potential corresponding to a perpendicular magnetic field. The aggregation of electrons into these cyclotron orbits forms what are called Landau Levels (LLs). These are highly degenerate states with energies given by

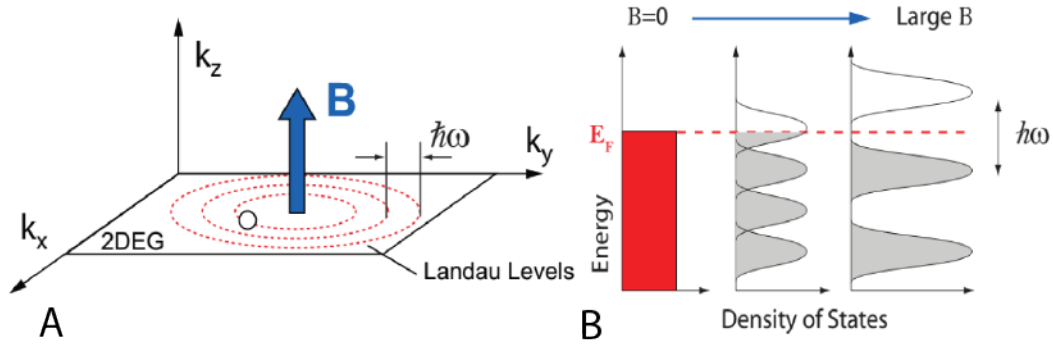


**Fig. 2.7:** A: conceptual representation of the formation of LLs in the bulk for both the sample (using the rotationally invariant symmetric gauge). B: the density of states. Taken from [17].

$$E_N = \left(N + \frac{1}{2}\right)\hbar\omega_c. \quad (2.8)$$

As can be seen from fig 2.7, as the magnetic field is increased, the spacing between the LLs is also increased. In the ideal limit, the density of states of LLs would be delta functions, however, the unavoidable introduction of disorder will broaden these into Gaussian like levels [64]. In order to observe the quantum Hall effect, the temperature must be smaller than the cyclotron gap between consecutive LLs. The carrier density required to fill a single LL is given by,

$$n_B = \frac{geB}{h} \quad (2.9)$$

where  $g$  accounts for the spin and valley degeneracy and  $n_B$  is the number of carriers in the LLs. As the magnetic field increases, the energy spacing between LLs increases and the degeneracy of each LL also increases allowing

for more carriers within a given LL. For a given number of carriers, the Fermi level will therefore be determined by how many LLs are filled or partially filled, as depicted in the right panel of fig 2.7. There are two parameters that can modify the position of the Fermi level with respect to the LLs: the carrier density, which can be modulated by doping or applied gate voltage, and the magnetic field. The filling fraction of the LLs is defined in the following way:

$$\nu = \frac{n}{n_B} = \frac{n\phi_0}{B}, \tag{2.10}$$

where  $\phi_0 = h/e$  is the flux quantum. A filling fraction of  $\nu = 1$  thus means that all the charge carriers are filling the first LL.

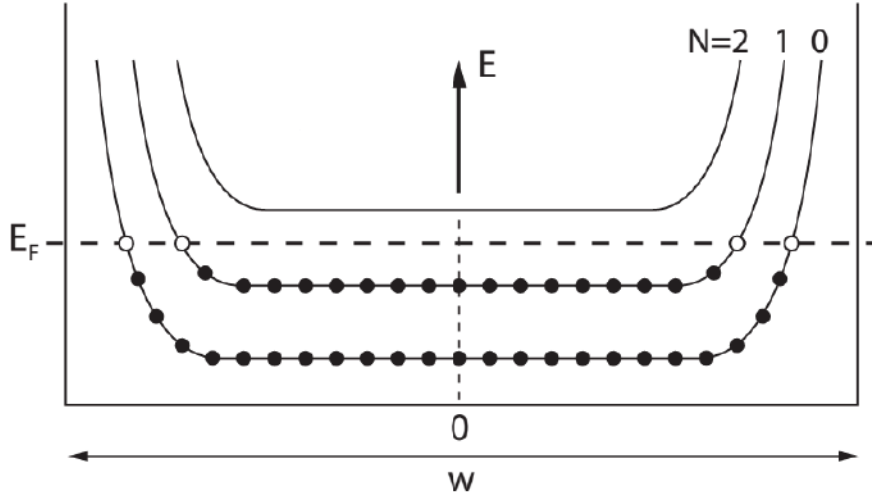


**Fig. 2.8:** Sample of width  $w$  showing the bending of the LLs as they approach the confining potential of the edges. Only the states at the intersection of the LL and the Fermi level will contribute to transport along the edge. Taken from [17].

When an integer number of LLs are filled in the bulk of the sample and thus the Fermi level is located between LLs, there will be no bulk conduction. The LL energy will however bend at the edge of the sample due to the electronic

confinement potential and thus edge conduction will arise from the intersection of the Fermi level and the LLs, as shown in fig 2.8. In a sample with two edges, there will be two counter-propagating channels (one on each side of the sample) that will carry a current with back scattering suppressed by the Lorentz force. The different electrochemical potentials of the counter propagating edges manifests itself as a transverse voltage  $V_y$  while simultaneously producing a null in the longitudinal voltage,  $V_x = 0$ . The null in longitudinal voltage arises because the electrochemical potential is constant along an edge. The allowed values of  $V_y$  when the Fermi level is located between two LLs will be given by an integer number of conductance channels multiplied by the current and divided by the degeneracy,

$$R_{xy} = \frac{h}{\nu g e^2}, \quad (2.11)$$

where  $h/e^2$  is the quantum of resistance and  $\nu$  the filling fraction.

### Integer Quantum Hall Effect in Graphene

Graphene's linear dispersion relation (and thus constant carrier velocity) and gapless nature will modify the quantum Hall effect in the following way. The cyclotron frequency in graphene is given by the Fermi velocity and magnetic length [14],

$$\omega_c = \sqrt{2} \frac{v_F}{l_B}, \quad (2.12)$$

where  $v_F$  is the Fermi velocity ( $\approx c/300$ ) and  $l_B = \sqrt{\frac{\hbar}{eB}}$  is the magnetic length. From this, it can be shown that the energy spectrum of the LLs is given by,

$$E_N = \pm \sqrt{2e\hbar v_F^2 |N| B} = \pm \hbar \omega_c \sqrt{|N|}, \quad (2.13)$$

where  $\pm$  represents the sign of the LL. The effect of a linear dispersion is to increase the LL energy spacing due to the increased value of  $\omega_c$ . The energy gap at 10T for GaAs/AlGaAs is  $\approx 10$ K, whereas for graphene it is  $\approx 1000$ K [14] between the  $0^{th}$  and  $1^{st}$  LLs. Given that the energy gap is so large and that the cyclotron energy scales as  $\sqrt{B}$  rather than linearly in  $B$  as in GaAs/AlGaAs, the quantum Hall effect in graphene is expected to be more robust to disorder. In addition, graphene is the only material for which the quantum Hall effect was measured at room temperature [27], a direct consequence of the large energy gaps mentioned above.

Another property requiring differentiation with conventional quantum Hall systems is the gapless nature of graphene's energy band diagram. This gapless nature yields an anomalous Hall sequence. The anomaly stems from the formation of a  $N = 0$  LL which is neither in the conduction band, nor in the valence band, but rather centered on the Dirac point. This ambiguity in associating the  $N=0$  LL with either conduction band or valence band states results in an offset of 0.5 in LLs of the Hall conductivity. Graphene's Hall sequence, with its spin and valley degeneracy preserved is given by,

$$\sigma_{xy} = \pm 4 \left( N + \frac{1}{2} \right) \frac{e^2}{h}. \quad (2.14)$$

The offset of  $1/2$  prompted several groups to take a closer look at the  $N = 0$  LL. It was found that spin degeneracy can be lifted and a  $\sigma_{xy} = 0$  plateau can be measured. However,  $R_{xx} \neq 0$  when  $\sigma_{xy} = 0$  [65]. The most complete integer quantum Hall sequence measured to date is  $\sigma_{xy} = \pm 0, 1, 2, 3, 4, \dots, 14 \frac{e^2}{h}$  upon spin and valley splitting [66, 65]. Table 2.1 shows a summary of the difference between graphene and 2DEGs for the formation of LLs.

**Table 2.1** Summary of differences between a 2DEGs and graphene for cyclotron frequency  $\omega_c$ , energy dispersion  $E_N$  and allowed fillings  $N$ .

	Conventional	Graphene
$\omega_c$	$\frac{qB}{m^*}$	$\sqrt{2} \frac{v_F}{l_B}$
$E_N$	$(N + \frac{1}{2}) \hbar \omega_c$	$\pm \hbar \omega_c \sqrt{ N }$
$N =$	$1, 2, 3, 4, \dots$	$\pm 0, 1, 2, 3, 4, \dots$

At the electron density labeled i) on fig 2.9, it is clear that  $R_{xx}$  is at a local maximum while  $\sigma_{xy}$  is at the edge of the plateau. At point i), the LL in the bulk is partially empty and so the charge carriers conduct as they would in an unfilled conduction or valence band. However, when a LL in the bulk is completely filled (indicated by point ii on fig 2.9),  $R_{xx}$  falls to zero and  $\sigma_{xy}$  is at the plateau. The value of  $\sigma_{xy}$  in a conventional 2DEG corresponds to the number of LLs that are filled multiplied by the degeneracy. The  $1/2$  offset

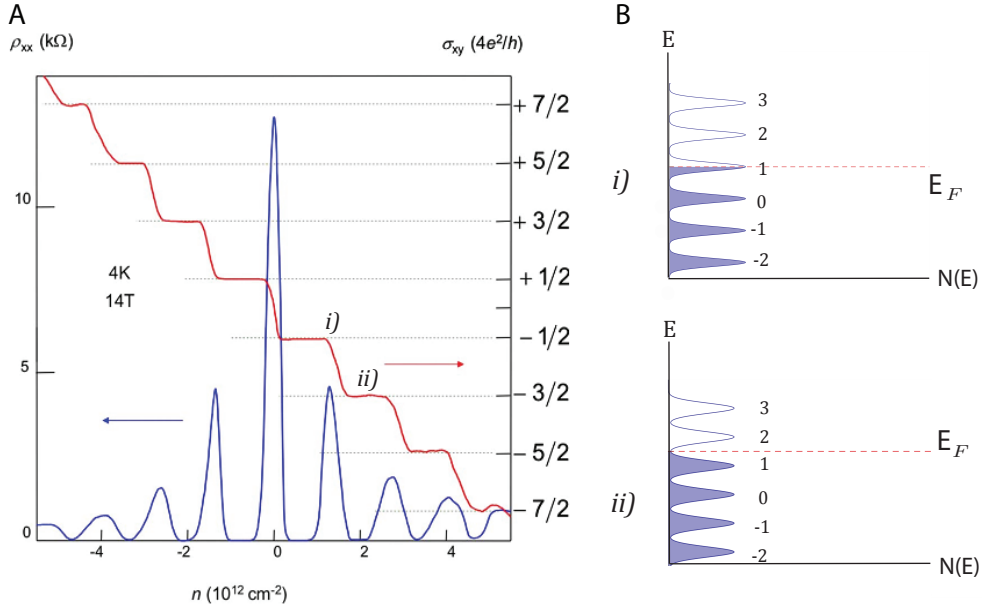


**Fig. 2.9:** A:  $\rho_{xx}$  and  $\sigma_{xy}$  as a function of carrier density for a graphene sample. Modified from [14]. B: Energy *vs* the density of states in the bulk of the sample when there is a plateau in  $\sigma_{xy}$  (i) or not (ii). Modified from [14].

associated with the  $N = 0$  LL modifies this correspondence. For example in this graphene sample at the point labeled ii) in fig 2.9, conduction is mediated by electrons. There are  $\sigma_{xy} = \frac{6e^2}{h}$  channels for propagation along the edge. Given a degeneracy of  $g = 4$ , as inferred from the plateau spacing of  $4e^2/h$  in  $\sigma_{xy}$ , the number of LLs contributing to conduction is  $6/4 = 1.5$ . The  $N = 0$  LL is filled with electrons, but in fact only contributes  $1/2ge^2/h = 2e^2/h$  to  $\sigma_{xy}$ . At neutrality, the  $N = 0$  LL is already half filled with electrons, and a charge neutral sample will give transverse conductivity  $\sigma_{xy} = 0$ . It is thus only the electrons required for filling half of the  $N = 0$  LL that contribute to  $\sigma_{xy}$ , in the amount of  $2e^2/h$ . The remaining  $4e^2/h$  of conduction is provided by a filled  $N = 1$  LL, again taking into account degeneracy  $g = 4$ .

## 3

**Fabrication and Apparatus**

Graphene was grown on copper foils using chemical vapor deposition with organic precursors, following the technique of Ruoff *et al.* [67]. Hydrogenation was performed in a ultra high vacuum chamber by thermally cracking molecular hydrogen flowing through a white-hot tungsten capillary. All details pertaining to the fabrication of hydrogenated graphene devices are presented in this chapter. The apparatuses used to measure temperature dependent transport are standard liquid helium 3 (LHe3) and liquid helium 4 (LHe4) cryostats. The infrastructure used to perform magnetotransport measurements are standard superconducting magnets up to 9T at McGill, resistive magnets to 33T and a hybrid resistive and superconducting magnet up to 45T at the National High Magnetic Field Lab (NHMFL) in Tallahassee.

## 3.1 Graphene Fabrication

### 3.1.1 Chemical Vapor Deposition Growth of Graphene

This section describes the chemical vapor deposition (CVD) process used for the growth of graphene on copper in collaboration with Prof. Mohammed Sijaj's group at Université du Québec à Montréal. This method was first realized by Ruoff's group in 2009 [67]. It is known that in general, CVD grown graphene samples have lower mobility, more cracks and defects than exfoliated graphene [68]. This growth method was chosen because of the overall ease of processing and the large sample size that can be achieved. Lower sample quality is not a limiting factor for this work involving the introduction of comparatively high levels of disorder.

Ruoff's use of Cu as a growth substrate for CVD graphene growth was followed. Cu is well suited for monolayer graphene growth because of its low cost and the low solid solubility limit of C in Cu (0.008% at 1084°C [53]) favours graphene growth by surface adsorption rather than the more difficult to control phase segregation of dissolved C. The copper substrate was thoroughly cleaned with 1M acetic acid at 60°C for 10 minutes followed by a 10 minute immersion in acetone and a 10 minute immersion in isopropyl alcohol. The Cu substrates are then inserted into a glass tube furnace where the oxide walls will remain inert up to approximately 1000°C. The chamber was pumped out to a base pressure of  $10^{-5}$  Torr. When the temperature reaches approximately 250°C, the chamber was pressurized with 700 mTorr of hydrogen gas. Once

the temperature has reached  $980^{\circ}\text{C}$ , methane was flowed into the chamber at 38 sccm (standard cubic centimeters per minute) until the total pressure reaches 1.1 Torr. The graphene was left to grow for 1.5 hours at which point the methane gas was switched off and the furnace was left to cool. Hydrogen gas flow was maintained during the entire cooldown. A schematic of the set-up is shown in Fig 3.1.

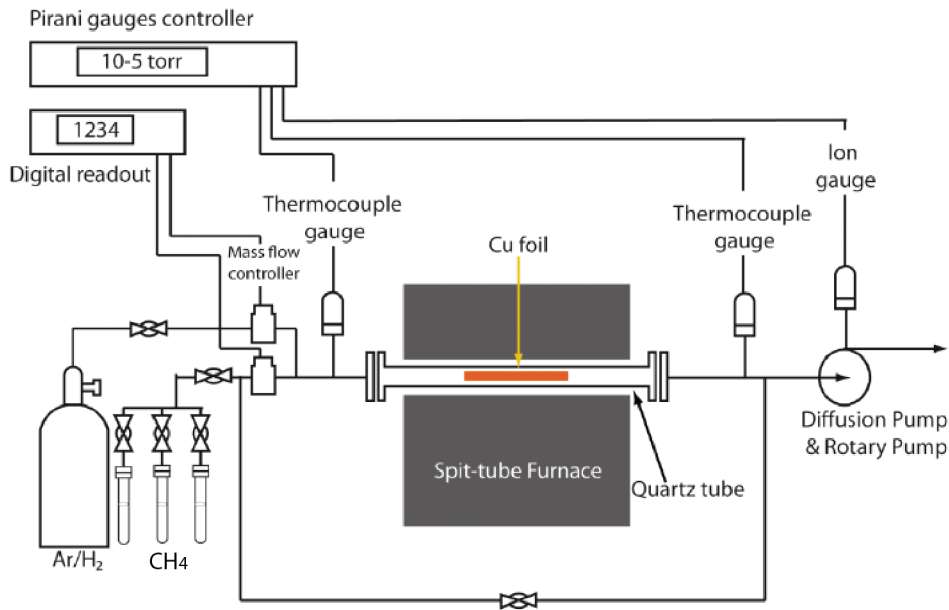


**Fig. 3.1:** Schematic of the CVD system used to grown graphene on copper from [19].

### 3.1.2 Graphene Transfer

Once graphene on copper was obtained, it must be transferred onto a substrate suitable for experiments. For electronic transport experiments, the standard Si/SiO<sub>2</sub> stack with 300 nm of SiO<sub>2</sub> is suitable. Silicon wafers are

purchased from Addison Engineering and are degenerately doped with arsenic to a concentration of  $2 - 5 \cdot 10^{19} \text{cm}^{-3}$  which is equivalent to a resistivity of  $1 - 5 \text{m}\Omega \cdot \text{cm}$ . This concentration of dopants ensures metallic behavior of the silicon substrate down to at least 20 mK. The resistance corresponding to the metal insulator transition in arsenic doped silicon is  $\approx 7 \text{m}\Omega \cdot \text{cm}$  [69] at room temperature. An oxide thickness of 300 nm also provides a high optical contrast of graphene monolayers via a Fabry-Pérot effect and sufficient thickness to allow handling of the substrates with low risk of dielectric breakdown that would impair field effect measurements. The silicon oxide was obtained by a chlorinated dry thermal oxidation followed by a forming gas anneal.

One side of the copper/graphene stack was spin coated with a 50 nm layer of poly-methyl methacrylate (PMMA) to provide a handle with which to transfer the graphene sample. The newly covered stack was then floated atop a 0.1M solution of ammonium persulfate ( $(\text{NH}_4)_2\text{S}_2\text{O}_8$ ). Note that it was not immersed, it was essential that the side with the PMMA handle remain uncovered by the solution to allow flotation by surface tension. The ammonium persulfate will etch away the copper after  $\approx 24$  hours. The remaining transparent film was then removed from the solution using glass slides and deposited in a de-ionized water bath to stop the reaction. After 15-30 minutes, the film was picked up using the Si/SiO<sub>2</sub> stack. The final product was left to dry for 36-48 hours. Finally, the PMMA layer was removed by a 2-4 hour immersion in acetone followed by a 5 minute IPA and DI water clean. A summary of this process is shown in fig 3.2.

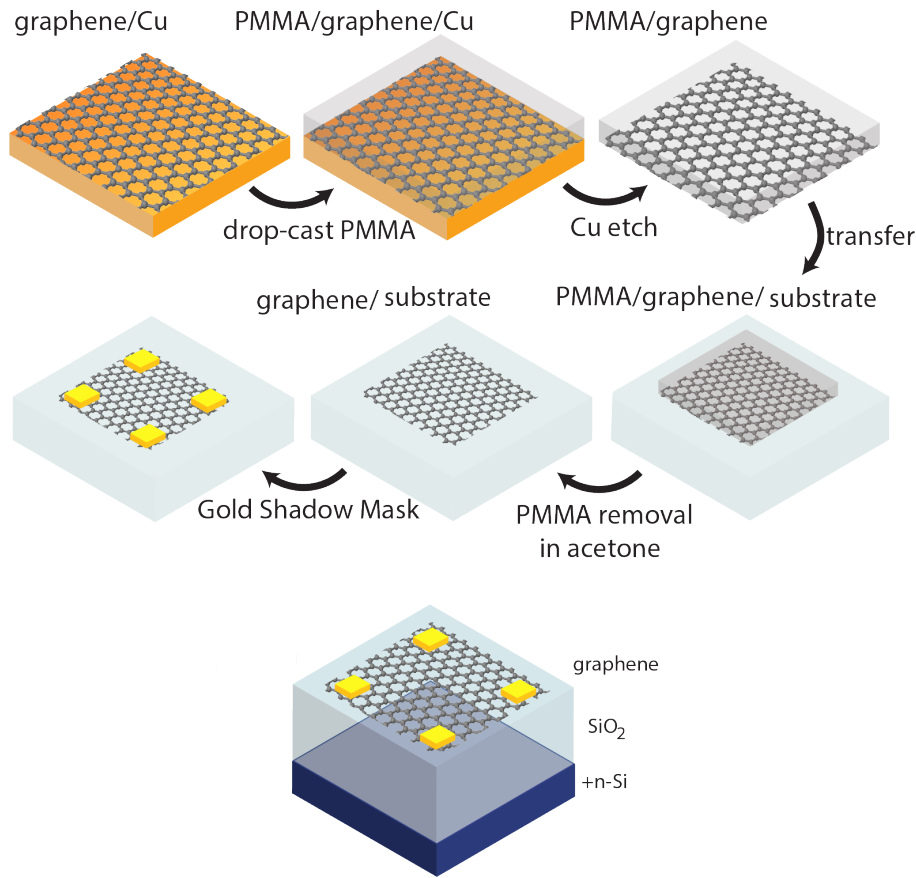


**Fig. 3.2:** Process flow for the fabrication of large area graphene samples on a silicon back-gate substrate. Picture taken from [19].

### 3.1.3 Contacting, Slicing and Dicing

A shadow mask was used to contact the graphene samples because it provides a resist free way of contacting the sample. The mask that was used was a 6 by 6 contacts mask where the individual contacts are 200 by 400  $\mu\text{m}$ . The spacing between contacts was  $\approx 2.5\text{mm}$ . The Hall bar mask has similar contact size and has a 5:1 length to width ratio with six voltage probe contacts and two large current sourcing pads as shown in fig 1 in the appendix. The metal stack deposited by electron beam evaporation was 3 nm of Ti and 50

nm of Au. Titanium was chosen because it provides an optimal wetting layer on graphene because their work functions are close and titanium is experimentally found to yield the lowest contact resistance [70]. Gold was chosen because it does not oxidize, it provides good adhesion for wire bonding, and the desorption temperature of hydrogen on gold is between 150K and 175K [71]. The silicon oxide gate dielectric can however store hydrogen at room temperature. It is problematic when hydrogen is stored in the oxide as it was experimentally found to diminish the insulating quality of the oxide. This problem arises because the diffusion coefficient of atomic hydrogen in  $\text{SiO}_2$  is measured to be  $\approx 10^{-15}\text{cm}^2/\text{s}$  [72] and predicted to be potentially as large as  $\approx 4 \cdot 10^{-6}\text{cm}^2/\text{s}$  [73]. The simplest way to circumvent this problem is to ensure graphene was covering the entire surface that will be exposed to the hydrogen beam as graphene has been reported to be impermeable to all gases [74].

Dicing was performed to transform the 2 cm by 2 cm contacted graphene surface to 4-6 devices comprising of 4-8 contacts each. A diamond scribe tool was used to precisely cut the wafer piece into different sections. To prevent gate leakage, the graphene on the edges, which may be in contact with the Si back gate, must be de-coupled from the rest of the graphene sheet. This step was performed with a tungsten probe tip. The tip was also used to remove graphene sections that are not to be probed in transport measurements. A typical sample is shown in fig 3.3

In fig 3.3, the metalized sample is sitting atop a small copper foil (not visible) that was adhered to the G10 package using non conductive glue and

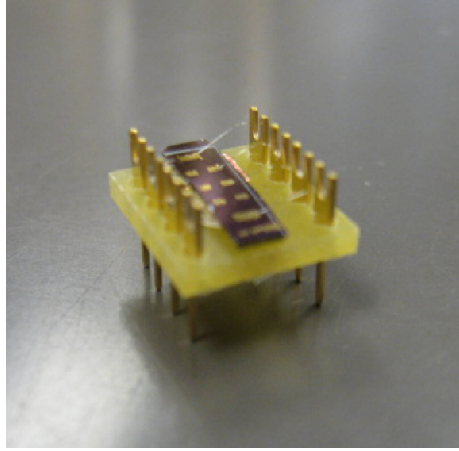


**Fig. 3.3:** Typical Hall bar shaped device on a G-10 carrier.

was shorted to a pin using silver paint (DuPont 4929). The same silver paint was used to adhere the device on the copper foil to ensure conductivity of the back gate. Aluminum wire bonds are then made between the device's contacts and the G10 package forks. The final step was to deposit small doses of silver paint on top of the aluminum bond-fork junction to solidify the contact.

## 3.2 Hydrogenated Graphene Fabrication

### 3.2.1 Hydrogen Gun and Set-Up

Producing a high flux of hydrogen atoms is of paramount importance for hydrogenating graphene samples. In collaboration with Richard Martel's group at Université de Montréal, a hydrogen gun based on thermal cracking of molecular hydrogen in an ultra high vacuum chamber was used to perform the hydrogenation as it is required that the hydrogen atoms bond to a clean graphene surface. A *in situ* measurement of resistance was added to the set-up to monitor the effect of hydrogenation on the two point resistance of the graphene

sheet.

The hydrogen gun consists of a cooling shroud made of copper, a tungsten filament wound in a circle (inside the cooling shroud), a stainless steel tube leading to a smaller tungsten tube capillary providing the flow of molecular hydrogen, a manual shutter and two thermocouples (one at the silver solder joint between the stainless steel fittings and one at the bottom of the copper shielding). This is inspired by Bertel's classic design [20] and shown in fig 3.4.

The thermionic emission current (typically 20mA) from the tungsten filament was accelerated towards the capillary by the application of a modest -600V voltage to the filament relative to the capillary (held at chamber ground). The temperature reached by the tungsten capillary has been measured using an IR thermometer (Mikron M90H) to be  $> 2000\text{K}$  which is measured to dissociate  $> 80\%$  of the hydrogen atoms [75]. The angular full width half maximum of the atomic hydrogen beam at our estimated flow of 1 sccm was  $\approx 15^\circ$  [76]. All wires have been encompassed in ceramic tubing so as to prevent electrical shorts. The cooling shroud provides cooling by either flowing chilled water or nitrogen gas through the cooling lines within the shroud walls. Water cooling allows the joint temperature to be maintained at or below  $20^\circ\text{C}$ , as measured by a thermocouple, during the hydrogenation process. The sample chuck also includes a tungsten filament under the sample which allows the sample to be heated in UHV to anneal and prepare the sample for hydrogenation. There are six wires from the sample chuck to the outside environment. Two of these wires are used to heat the tungsten filament under the sample chuck. The remaining four wires are used to contact the graphene sample. This allows

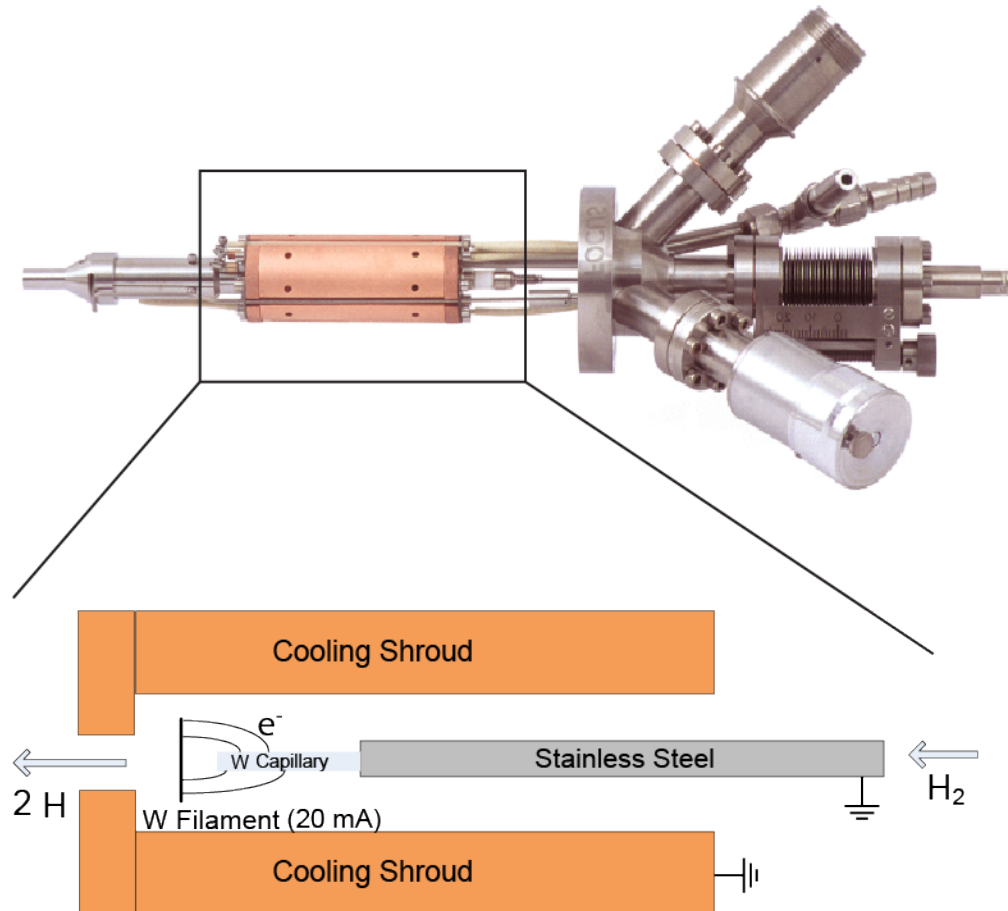


**Fig. 3.4:** Hydrogen gun with the design inspired from [20] and the top image taken from [21].

for a *in situ* measurement of two or four point resistance during either annealing or hydrogenation. The process by which graphene was hydrogenated has the following steps: the sample was inserted and the system was pumped down by an ion pump to the low  $10^{-8}$  or high  $10^{-9}$  Torr range. The sample was heated by electron bombardment of the sample chuck with its tungsten filament. The sample heating promotes the thermal desorption of any species

that may have adsorbed onto the surface from ambient conditions. The heating in particular aids in the desorption of water from the graphene / oxide interface. The sample was heated until its temperature reaches more than 100°C which takes  $\approx 15$  minutes while supplying  $\approx 2$  mA of emission current (using  $\approx 2.2$ A filament current and -600V bias relative to ground) between the tungsten filament under the sample and the grounded chuck. The sample was then left to cool down for 15-20 minutes or until the temperature of the transfer arm falls below 40°C as measured by the thermocouple on the transfer arm. This process can be shortened in duration by allowing nitrogen gas to flow in the transfer arm and indirectly cool the chuck. Before hydrogenation can begin, the ion pump must be turned off to allow a rise in pressure from the introduction of hydrogen gas. When turning off the ion pump, a turbo pump located in the sample load-lock chamber was used to pump out the hydrogen gas introduced to the chamber. The hydrogen gun was turned on by applying an accelerating voltage of -600V and increasing the filament current until the thermionic emission current reaches 20mA. The pressure in the chamber was increased to  $10^{-5}$  Torr of hydrogen from the base pressure of  $10^{-9}$  Torr using a butterfly leak valve. The multimeter was connected to the sample and the shutter opens: the hydrogenation begins. Fig 3.5 shows a picture of a sample undergoing hydrogenation.

### 3.3 Experimental Apparatuses and Techniques

Table 3.3 shows a summary of all the experimental apparatuses used in the collection of data including their respective base temperatures, how they

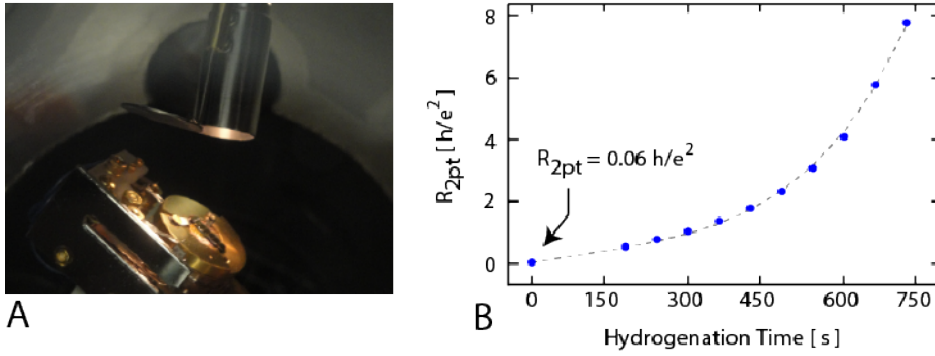


**Fig. 3.5:** A: A sample exposed to an atomic hydrogen beam. The light originates from the white hot tungsten filament heated to  $> 2000\text{K}$ . B: The two point resistance *vs* hydrogenation time taken *in situ* during the hydrogenation and an exponential fit to the curve.

reach those temperatures, the magnetic field, the measurements performed on that apparatus and the chapter where results observed with that particular apparatus are found.

**Table 3.1** Summary of apparatuses used.

Location	Base T [K] - Environment	B [T]	Measurement	Chapter
ECE	0.27 - Vacuum	0	R <i>vs</i> T	4, 5
ECE	9 - Vacuum	0	R <i>vs</i> T, Resp	5
Physics	1.6 - Exchange Gas	0	R <i>vs</i> T	4
Physics	0.27 - Vacuum	9	R <i>vs</i> [T,B]	5,6
NHMFL	0.27 - LHe3	18,33T	R <i>vs</i> [T,B](  , $\perp$ )	6
NHMFL	0.55 - LHe3	45T	R <i>vs</i> B	6

A standard low frequency AC lock-in technique was used throughout the

experiments. An AC sourcing voltage of 100mV RMS was applied to a 10M $\Omega$  resistor. The sourcing current,  $I_x$ , was applied to the  $I_+$  electrode and the  $I^-$  contact was kept at ground. A lock-in (SRS-830) set at a frequency of either 11 or 13 Hz with all filters off was used in differential (A-B) voltage mode as shown in fig 3.6. If the device was a Hall bar, two lock-ins were used to measure  $V_x$  and  $V_y$  simultaneously under the same settings after verifying that a simultaneous measurement doesn't change the single measurement. If, instead, the device was a two point device, the four contacts would be merged with BNC tees ( $I_+$  with  $V_+$  and  $I_-$  with  $V_-$ ). The voltage on the gate was set using a Keithley 2400 SourceMeter to source a DC voltage to the gate with respect to the  $I_-$  contact while keeping the DC leakage current under  $\approx 10\%$  of the AC sourcing current. For each measurement, a calibration up to 11 M $\Omega$  using a decade resistor box was performed since the lock-in input impedance (10 M $\Omega$ ) and the sample resistance up to 7M $\Omega$  present a non-negligible load on the current source. In the event where the resistance of the sample was expected to be of the same order as the 10 M $\Omega$  sourcing resistor, a second lock-in would be used to measure the voltage drop on the sourcing resistor. This measurement allows for a measurement of the sourcing current at all times which now allows a measurement of the device resistance.

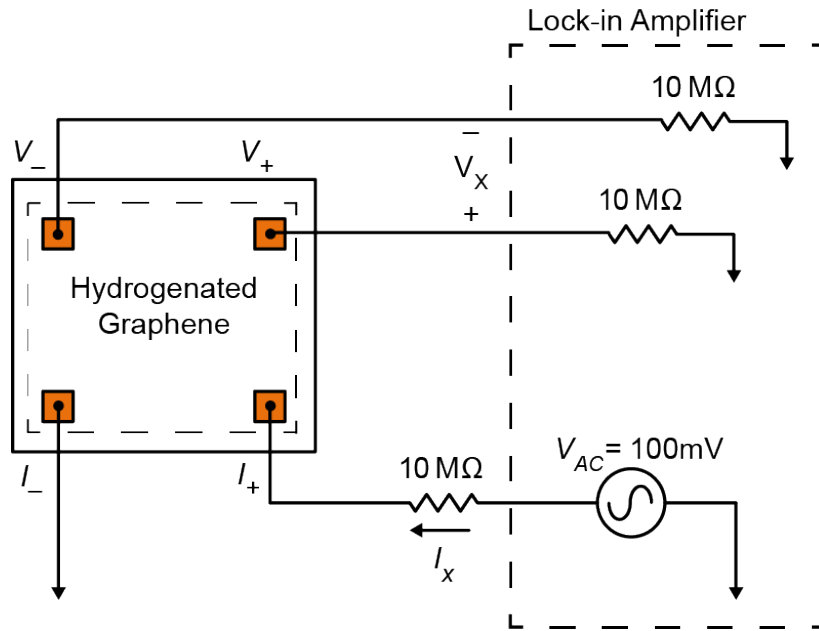


**Fig. 3.6:** Circuit diagram of a four point Van der Pauw measurement with a lock-in amplifier. A 100 mV RMS AC voltage is applied to a  $10\text{M}\Omega$  resistor to source a current  $I_x$ . The voltage  $V_x$  is measured using differential input on an SRS 830 with  $10\text{M}\Omega$  input impedance.

## Characterization of the Hydrogenation Process

In this chapter, Raman spectra and electrical transport measurements of hydrogenated graphene are described. The increase, upon hydrogenation of graphene, of the ratio of the intensity of the Raman D-band at  $1350\text{ cm}^{-1}$  Stokes shift to the intensity of the Raman G peak at  $1585\text{ cm}^{-1}$  is a clear signature of the introduction of translational symmetry breaking point defects. Raman mapping reveals a heterogeneous defect density and a comparison across samples reveals significant variation in defect density increase with hydrogen dose. The increase, upon hydrogenation of graphene, in electrical resistance and development of insulating ( $dR/dT < 0$ ) behavior is qualitatively consistent with a transition from band conduction to a variable range hopping regime. However, the resistance does not quantitatively fit any known model for variable range hopping over the wide range of temperature investigated.

### 4.1 Raman Spectroscopy

Raman spectroscopy is a powerful tool to analyze material properties, including graphene. A review of the theory and practice of Raman spectroscopy

in the study of graphene is beyond the scope of this thesis, and the reader is encouraged to consult the tome of Herzberg [77] for a general introduction to Raman spectroscopy, or the review by Jorio *et al.* [78] on the application of Raman spectroscopy to graphene. Notably, defect density can be probed by Raman spectroscopy in graphene but not in conventional buried 2DEGs. Indeed, graphene shows an anomalously strong Raman scattering due to the resonant conditions provided by its zero-gap bandstructure [78].

#### 4.1.1 Experimental Details about the Raman Systems

Two systems were used to collect Raman spectra of graphene and hydrogenated graphene.

The first system that was used to gather Raman spectra on samples is a Renishaw RM3000 which is a point mapping micro-spectrometer. It delivers up to 15 mW of power to the sample through a linearly polarized 514 nm Ar ion laser (Spectra Physics 177-G42). The signal reflected from the sample is collected through with a 20x objective that has a numerical aperture of 0.4 and is sent through a 50  $\mu\text{m}$  slit and diffracted with a grating of 1800 lines per mm. This system collects Raman spectra point-by-point with a spot size of  $\approx 1\mu\text{m}$ .

The second spectrometer is a Raman Hyperspectral Imager (RIMA) manufactured by Photon *etc.* Unlike a point mapping micro-spectrometer, the RIMA is an imaging spectrometer. It can deliver up to 4W of power on the sample using a single mode doubled Nd:YAG laser operating at 532 nm. It

is an imaging spectrometer that uses volume Bragg gratings. A 50x objective with a numerical aperture of 0.8 was used, resulting in a two dimensional Raman map of  $225 \times 225 \mu\text{m}^2$  from  $1000 \text{ cm}^{-1}$  to  $3000 \text{ cm}^{-1}$ , with a resolution of  $\approx 500\text{nm}$ .

#### 4.1.2 Classification of Raman Peaks and Bands in Graphene

Table 4.1 shows the Raman peaks and bands typically observed in graphene, including peaks and bands whose intensity depends upon the translational symmetry breaking of defects. Notably, the Raman peaks correspond to different scattering processes, involving either one or two phonons and in some cases scattering by a point defect. The scattering can involve intra-valley ( $K \rightarrow K$ ) and inter-valley ( $K \rightarrow K'$ ) transitions. The scattering processes that occur in graphene to produce the three main peaks (D, G and  $G'$ ) are shown in fig 4.1.

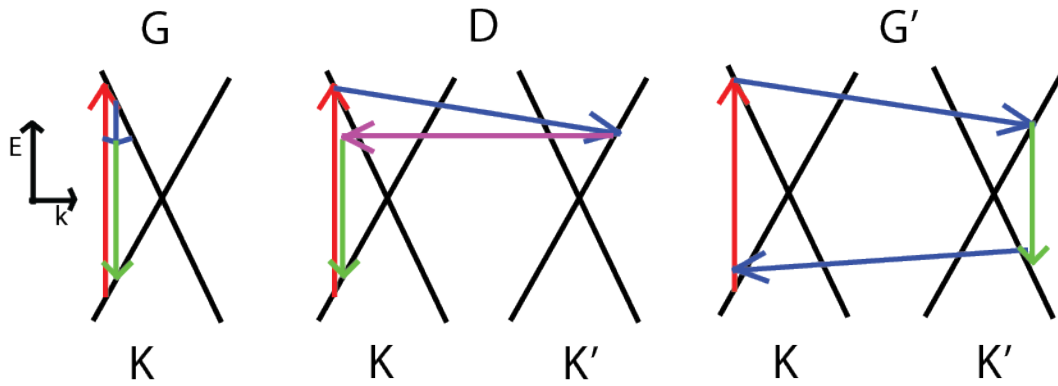


**Fig. 4.1:** E-k diagrams of the Raman Stokes scattering process corresponding to the G, D, and  $G'$  peaks. Transitions are indicated by arrows, wherein: red arrows represent photon absorption, blue arrows represent phonon emission, purple arrows represent scattering by a defect potential, and green arrows represent photon emission. Modified from [22].

The lines in fig 4.1 show, that there is a mode that is excited in energy with the incoming photon (red line). That excited mode may then scatter off a phonon (blue line) to the K' valley or stay in the K valley depending on the momentum modification. The green line represents the emission of a photon that generates the Raman signal. In clean graphene, there are no defects to scatter off of (purple line) and thus only the G and G' processes are allowed. In disordered graphene, the presence of defects allows a scattering mechanism that uses defects and enables the D peak to form, regardless of the defect type.

**Table 4.1** Summary of the position of the Raman Stokes shift at a pump wavelength of 514 nm with their commonly used label and scattering mechanism.

Wavenumber (cm <sup>-1</sup> )	Label	Scattering Mechanism
1350	D	single phonon + defect, inter-valley
1585	G	single phonon, intra-valley
1620	D'	single phonon + defect, intra-valley
2450	G*	double phonon, inter-valley
2700	G'	double phonon, inter-valley
2935	G+D	double phonon + defect, inter + intra-valley

Single crystal graphene exhibits three main peaks in the 1000 to 3000 cm<sup>-1</sup> range. The G, G\* and G' peaks are all active in a graphene with translational symmetry. The G peak is present in all sp<sup>2</sup> carbon systems and it is named for the G in graphite [78] given its sensitivity to C-C stretching. The wavenumber corresponding to the maximum intensity of the G peak is sensitive to the local levels of doping [79]. It is therefore expected that upon introducing lattice defects, via hydrogenation or otherwise, the G, G' and G\* peaks will appear with reduced intensity or disappear completely in the extreme case of high

disorder. The peaks or bands that appear upon introduction of translational symmetry breaking disorder are D, D' and G+D. In each of the D, D' and G+D peaks or bands, momentum is provided to the scattered electron by a defect that breaks translational symmetry, such as a point defect or edge. The intensity of these peaks or bands is related to the density of defects. The D band in particular has been used to estimate defect density in graphene sheets [23]. Owing to the experimental difficulty of measuring Raman scattering intensity in absolute units, the ratio of Raman intensities is commonly used. The ratio of Raman D band intensity,  $I_D$ , to Raman G peak intensity,  $I_G$  was used.

#### 4.1.3 Estimating Defect Density from Raman Spectra

To estimate the hydrogen induced defect density, the same phenomenological model is applied for point-defect induced disorder as has been successfully applied to understanding the correlation between defect spacing  $\lambda_D$  and Raman intensity ratio  $I_D/I_G$  in Ar<sup>+</sup>-ion bombarded graphene by Lucchese and coworkers [23]. In this phenomenological model, it is assumed that the graphene sample has point defects of uniform density without spatial correlations, in contrast to the situation of line defects as found in a poly-crystalline sample for example. Although the defects have no correlations, the model assumes there is a coalescence of the defected zones. The resulting phenomenological

mapping between  $I_D/I_G$  and  $\lambda_D$  is,

$$\frac{I_D}{I_G} = C_A \frac{r_A^2 - r_S^2}{r_A^2 - 2r_S^2} \left[ \exp\left(\frac{-\pi r_S^2}{\lambda_D^2}\right) - \exp\left(\frac{-\pi(r_A^2 - r_S^2)}{\lambda_D^2}\right) \right] + C_S \left[ 1 - \exp\left(\frac{-\pi r_S^2}{\lambda_D^2}\right) \right] \quad (4.1)$$

where the parameters  $C_A = 4.2$ ,  $C_S = 0.87$ ,  $r_A = 3.0$  nm and  $r_S = 1.0$  nm for a pump wavelength  $\lambda = 514$  nm. The parameters respectively represent the measure of the maximum value of the  $I_D/I_G$  ratio, the value of the  $I_D/I_G$  ratio in the highly disordered limit, the radius of the activated region and the radius of the structurally damaged region. These parameters were determined empirically from experiment. This curve and its fit with experimental Raman spectra of ion bombarded graphene is illustrated in fig 4.2.

Our Raman spectra measured at a  $\lambda = 514$  nm pump wavelength must be corrected for the pump wavelength dependence of  $I_D/I_G$ . Assuming that the known  $I_D/I_G \propto \lambda^4$  scaling for edge defects [78] can be applied to point defects, giving an estimated correction  $I_D/I_G(514 \text{ nm}) = (514/532)^4 \times I_D/I_G(532 \text{ nm})$  for comparison with the phenomenological model.

Importantly, there is a non-monotonic relationship between  $I_D/I_G$  and  $\lambda_D$ , as clearly seen in fig 4.2, arising from the coalescence of the effective area around defects where D peak scattering occurs. This introduces ambiguity into the inference of  $\lambda_D$  from  $I_D/I_G$  alone. To resolve this ambiguity, the D' peak can be used. The D' can also be utilized to differentiate the type of defect ( $sp^3$ , vacancy or boundary) [80].

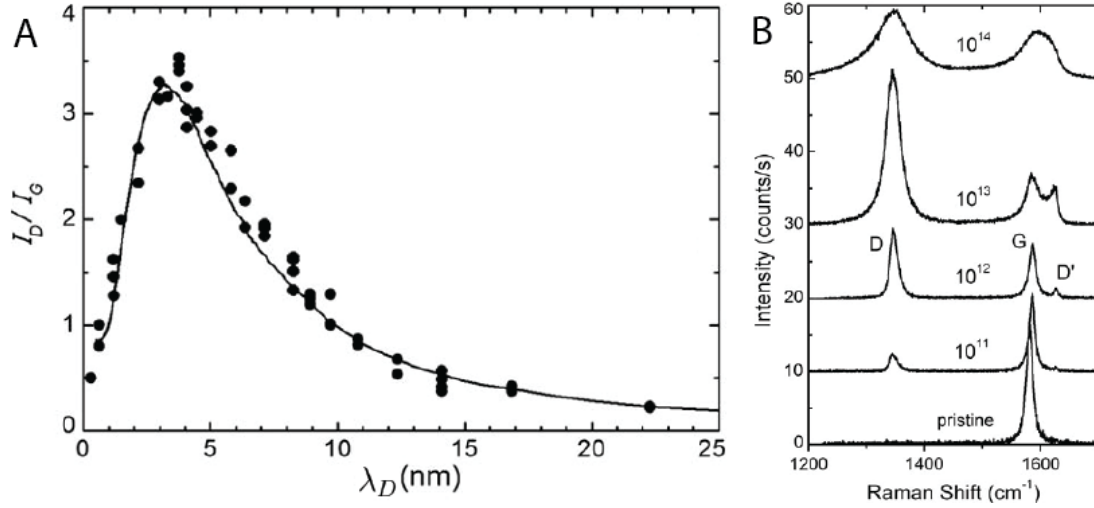


**Fig. 4.2:** Experimental Raman spectra from three different graphene samples bombarded by ions at a pump wavelength of 514 nm. A: Non-monotonic relationship between  $I_D/I_G$  and the defect density  $\lambda_D$ . B: Use of the D' peak to resolve ambiguity in determining  $\lambda_D$  from  $I_D/I_G$ . Taken from [23].

#### 4.1.4 Single Point Raman Spectra

Fig 4.3 gives a comparison of the Raman spectra of unhydrogenated and hydrogenated graphene. One sample was hydrogenated for four minutes, and the other sample was hydrogenated for fifteen minutes. All the samples analyzed are CVD grown on Cu and transferred to a Si/SiO<sub>2</sub> substrate.

Fig 4.3 shows several features that are common to all disordered graphene spectra observed in this project. The first is the large increase of the D peak intensity from being slightly above the noise floor of the spectrum in clean graphene to being the largest peak of the hydrogenated graphene spectrum. Fig 4.3 also shows a significant relative reduction in the G' peak intensity. The G' peak is sensitive to translational symmetry breaking and is correspondingly reduced in intensity by hydrogenation.

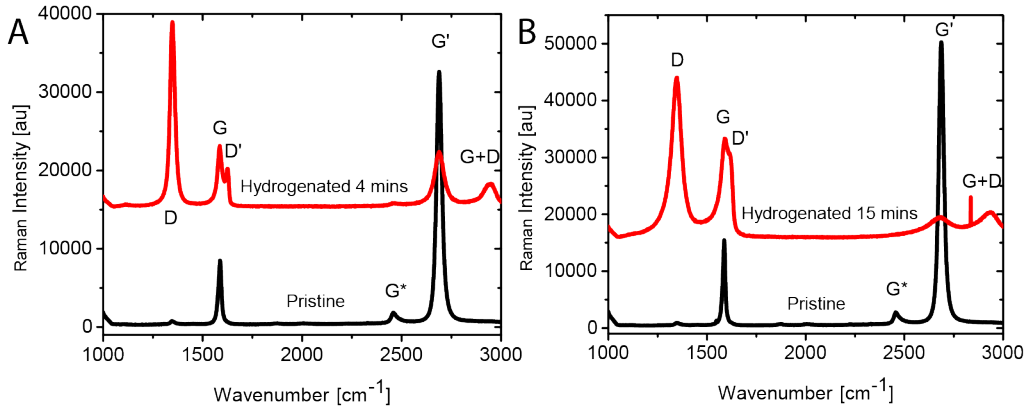


**Fig. 4.3:** Comparison of Raman spectra before (black) and after (red) hydrogenation. A: Hydrogenation time of 4 minutes with an extracted  $\lambda_D \approx 4.5\text{nm}$ . B: Hydrogenation time of 15 minutes with an extracted  $\lambda_D \approx 1.5\text{nm}$ . A vertical offset has been applied to the hydrogenated graphene spectra.

To summarize, the experimental evidence provided by Raman spectroscopy that the hydrogenation process increases point defect density is:

- D peak intensity increase
- D' peak intensity increase
- G' peak intensity decrease
- G\* peak intensity decrease
- G+D peak intensity increase

Raman point mapping gives information about the state of the graphene illuminated by the laser spot, but is painstaking and time consuming to probe the state of large-area graphene such as that used in this work.

#### 4.1.5 Raman Maps

To obtain a more representative estimate for the defect density of an entire sample, the RIMA system was used on graphene samples and their hydro-

generated counterparts on the same physical location of the sample. Fig 4.5 shows the difference in the maps for the intensity of the D and G peaks. This sample was hydrogenated for twelve minutes.

Upon the acquisition of a Raman spectral image, meaning a Raman spectrum at each image pixel, the peak intensities are carefully determined. The Raman baseline (blue curve in fig 4.4) is effectively removed by fitting the Raman spectrum to a sum of a third-order polynomial for the baseline and a Lorentzian lineshape for either the G or D peak (green curve in fig 4.4).

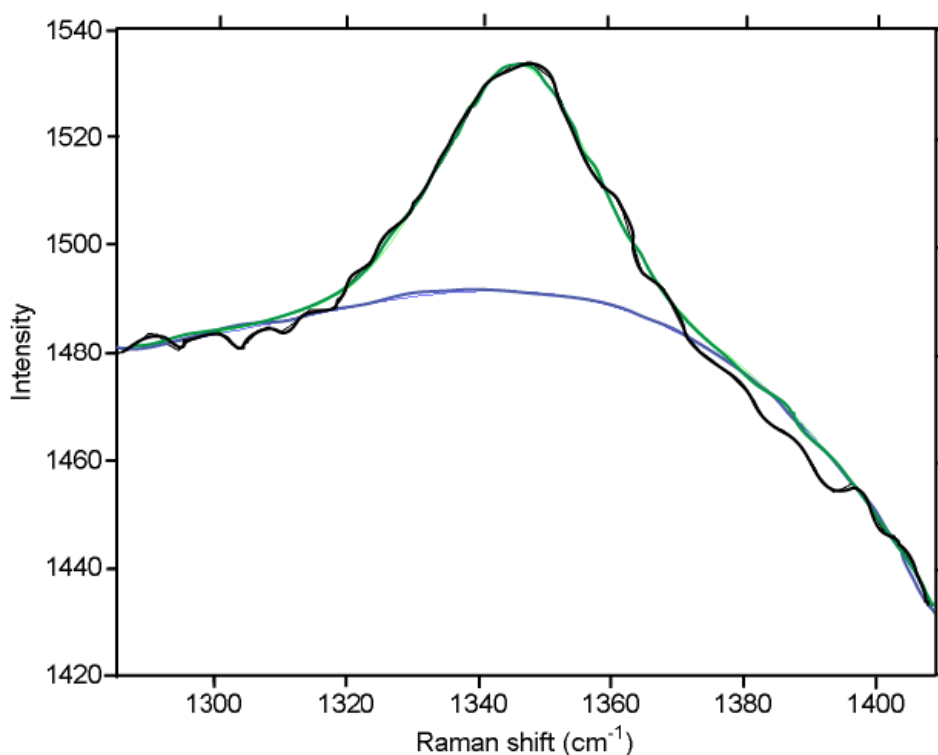


**Fig. 4.4:** A typical fit of the D peak for one of the points making up the Raman map. The blue line is the baseline fit, the green line is the signal fit and the black line is the data. Data taken from the 12 minute hydrogenation sample.

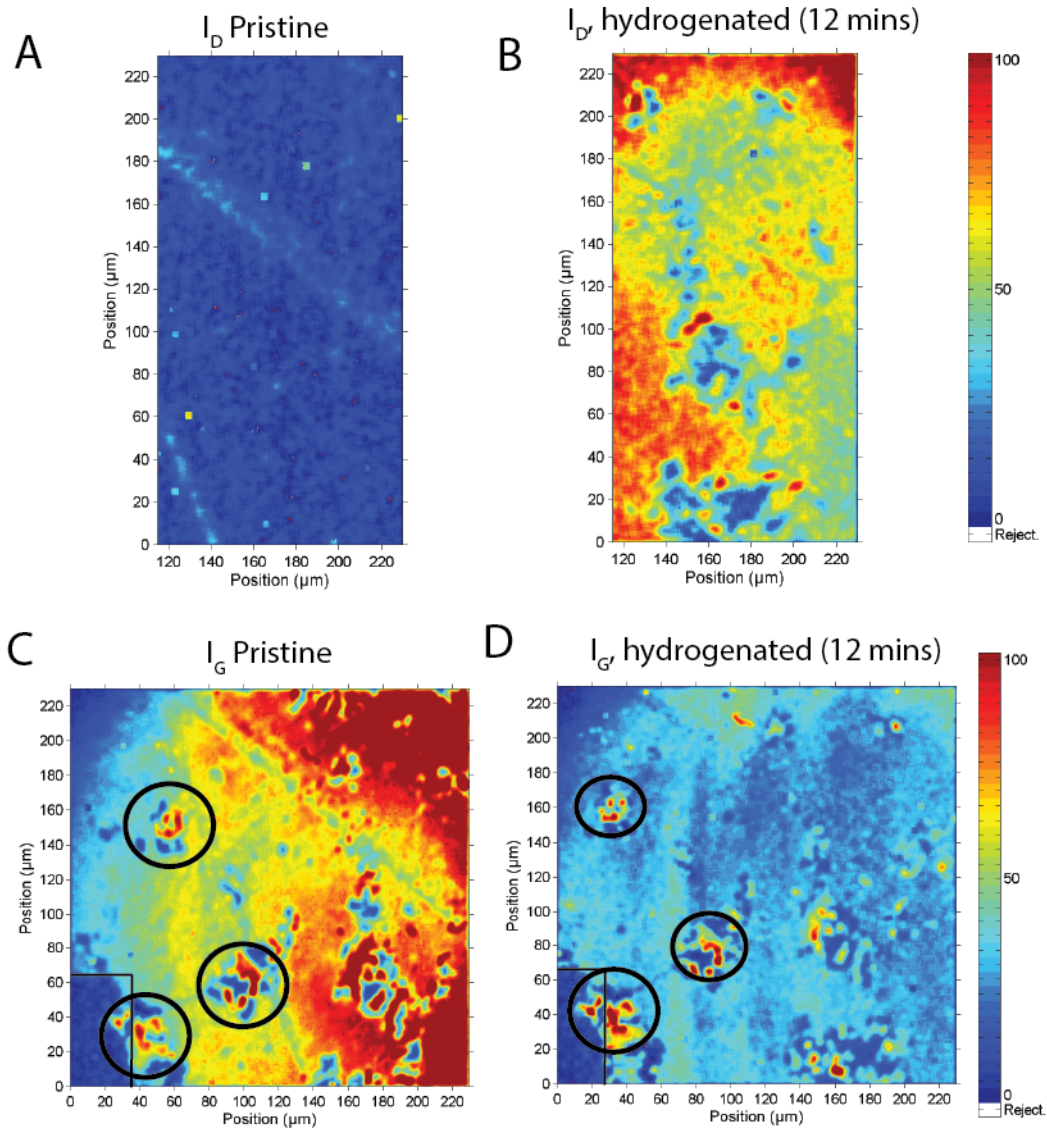


**Fig. 4.5:** Comparison of Raman maps where both the  $x$  and  $y$  axes are positions in  $\mu\text{m}$ . These are from the same sample which was hydrogenated twelve minutes. A: Intensity of the D peak before hydrogenation. B: Intensity of the D peak after hydrogenation. C: Intensity of the G peak before hydrogenation. D: Intensity of the G peak after hydrogenation. The bottom left corner of maps C and D is a scratched off gold pad. The circles represent regions which have defects before hydrogenation.

The full width half max, the position in wavenumber and the intensity of those peaks can thus be extracted. As can be seen in fig 4.5 and consistent with the Raman point spectroscopy, the G peak intensity is reduced upon hydrogenation and the D peak intensity is enhanced upon hydrogenation. It can be seen from the mapping that the defect density is non-uniform over the sample, as observed in the fluctuation of the D peak intensity after hydrogenation. Regions that were initially more disordered, such as the line defects diagonally crossing the sample in panels A and C, do not seem to correlate with more hydrogen coverage. The nature of these line defects is not known. Looking at the G peak intensity image after hydrogenation (panel D of fig 4.5), the G peak intensity has dramatically reduced over the majority of the mapped sample area. The only regions with negligible reduction in G peak intensity are circled in black. It is hypothesized that these regions suffer reduced hydrogen exposure on account of unintentional surface contamination that was not removed by the rinsing and annealing steps prior to hydrogenation.

A comparison of Raman maps for samples hydrogenated for six, eight, ten, and fourteen minutes is presented in fig 4.6, with the extracted  $I_D/I_G$  ratio plotted. The mean value of  $I_D/I_G$  over the mapped area is then compared in fig 4.7. The error bars were computed as a standard deviation of  $I_D/I_G$  over the map, and is thus an indication of the inhomogeneity of  $I_D/I_G$ . Importantly, it is observed that hydrogenation time gives poor predictive power, from sample to sample, of the mean Raman ratio  $I_D/I_G$ .

It is first interesting to note from fig 4.7 that for samples hydrogenated the same duration, the D/G ratio values for the samples hydrogenated 10

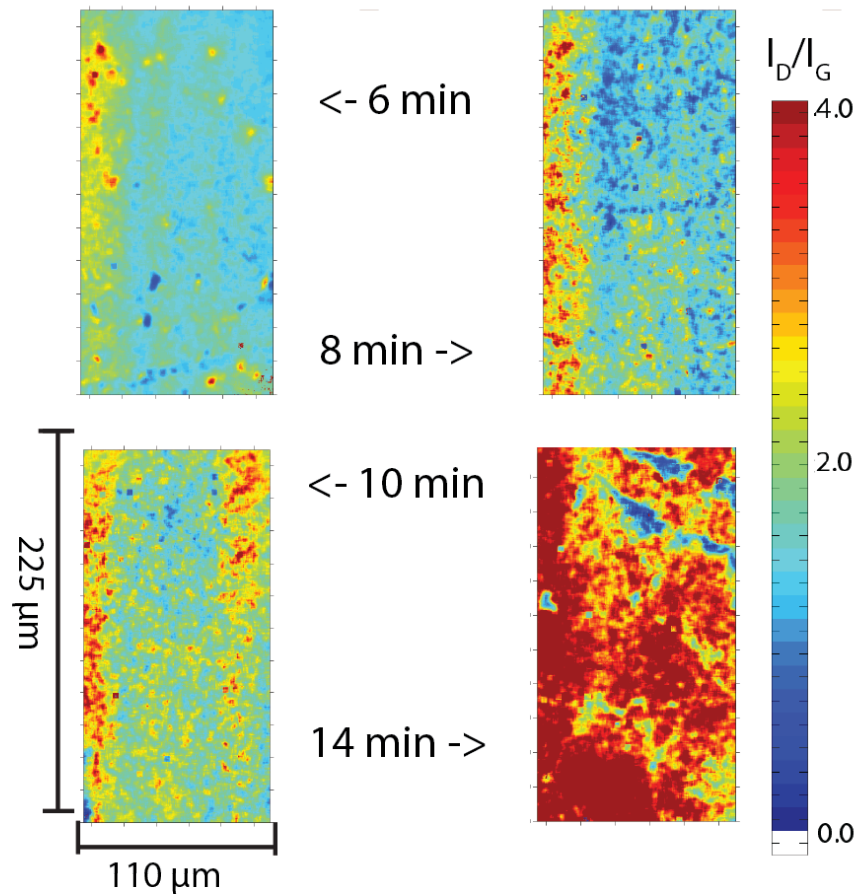


**Fig. 4.6:** Raman D/G ratio maps for samples hydrogenated six, eight, ten and fourteen minutes. All areas shown are  $110 \times 225 \mu\text{m}^2$ .

minutes do not match within the error bars. The only common trait held by all points is that they were all grown on Cu at the same time. Fig 4.7 also shows that in the limit of high hydrogenation, the D/G ratio does not follow the same trend as is expected from fig 4.2. The data rather seems to suggest that samples will hydrogenate at different rates thereby making it unreliable to use hydrogenation time as a figure of merit of disorder. Nonetheless, Raman maps do provide a useful tool to visualize the variation in defect density.

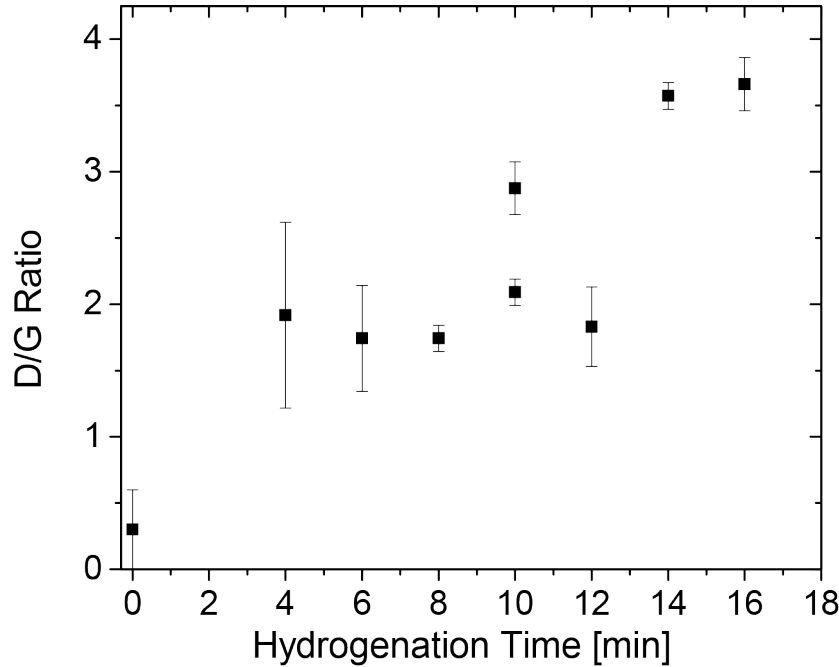


**Fig. 4.7:** Comparison of mean  $I_D/I_G$  ratio from Raman maps in fig 4.6 as a function of hydrogenation times for different samples. The points are taken from Raman maps (RIMA) in fig 4.6 with a typical clean sample at zero minutes for comparison. Every point corresponds to an independent sample.

## 4.2 From Raman to Transport

To bridge the understanding imparted by Raman maps and electronic transport, it is useful to measure the *in situ* resistance as a function of hydrogenation time. This measurement is taken in UHV as the sample is being hydrogenated, without breaking vacuum. As seen in fig 4.8, the resistance increase exponentially with hydrogenation time.

This measurement is an indication that hydrogenation causes a dramatic modification of the electronic transport properties of graphene. Many tests were done to confirm that the cause of this increase was the hydrogen. For example, heating the gun with no hydrogen, flowing hydrogen without ther-

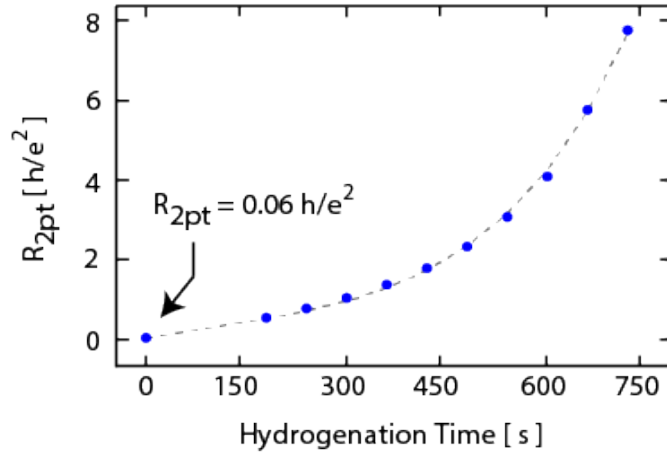


**Fig. 4.8:** Two point resistance as a function of hydrogenation time. Measured *in situ* during the hydrogenation process at 300K with an exponential fit represented by the dashed line.

mally cracking it and closing the shutter were all measured to yield no change in resistance. The exponential increase in resistance with hydrogen dose is inconsistent with doping, but rather with the introduction of disorder.

### 4.3 Temperature Dependent Transport

Another way to characterize the hydrogenation process is by measuring the temperature dependent resistance of the hydrogenated graphene. Fig 4.9 shows the measured resistance as a function of temperature at different gate voltages.

Fig 4.9 shows that the overall magnitude of  $dR/dT$  of the devices is carrier density dependent, however, its sign remains negative for all charge carrier densities. For this particular sample (HG9), the charge neutrality point is not exactly known, yet is most likely at a gate voltage above 50V. Looking at the

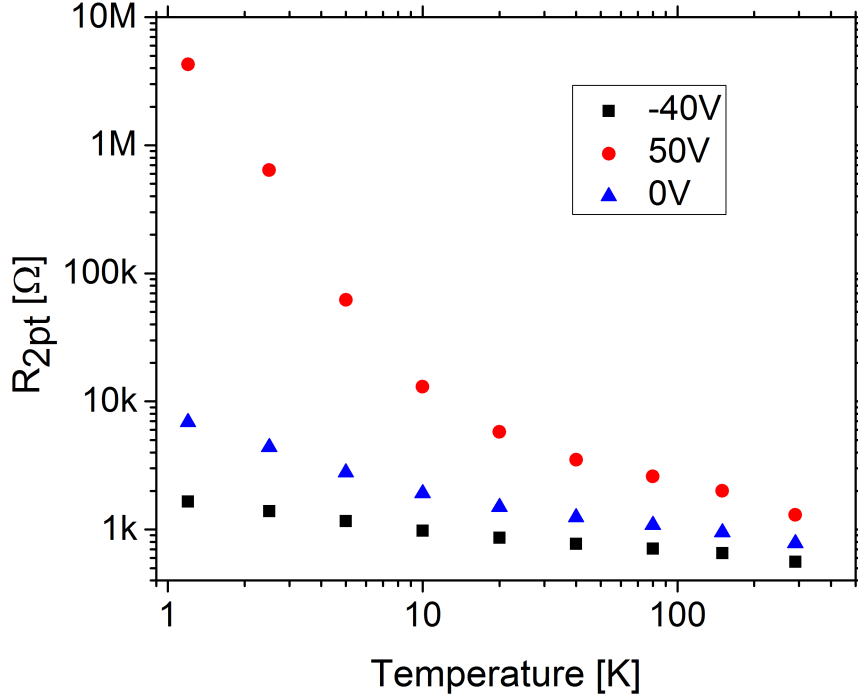


**Fig. 4.9:** Two point resistance *vs* temperature in log-log scale of sample HG9. Three different gate voltages are shown: -40V (black), 0V (blue) and 50V (red), with the latter having the fewest charge carriers (the device is p-type).

data in a log-log plot as is shown in fig 4.9, there seems to be a slope change at a temperature slightly above 10K, however this feature is absent in the -40V dataset. Recall from chapter 2 that the temperature dependence of the resistance is expected to follow Eq. 4.2 with  $n = 3$  in the case of Mott variable range hopping (VRH), or with  $n = 2$  in the case of Efros-Shklovskii variable range hopping (ESVRH) [15, 61], *i.e.*

$$R = R_0 \times e^{-(T_0/T)^{1/n}}. \quad (4.2)$$

By plotting the data shown in fig 4.9 with the specific purpose of deter-

mining whether  $n = 2$  or  $3$  is observed yields fig 4.10.

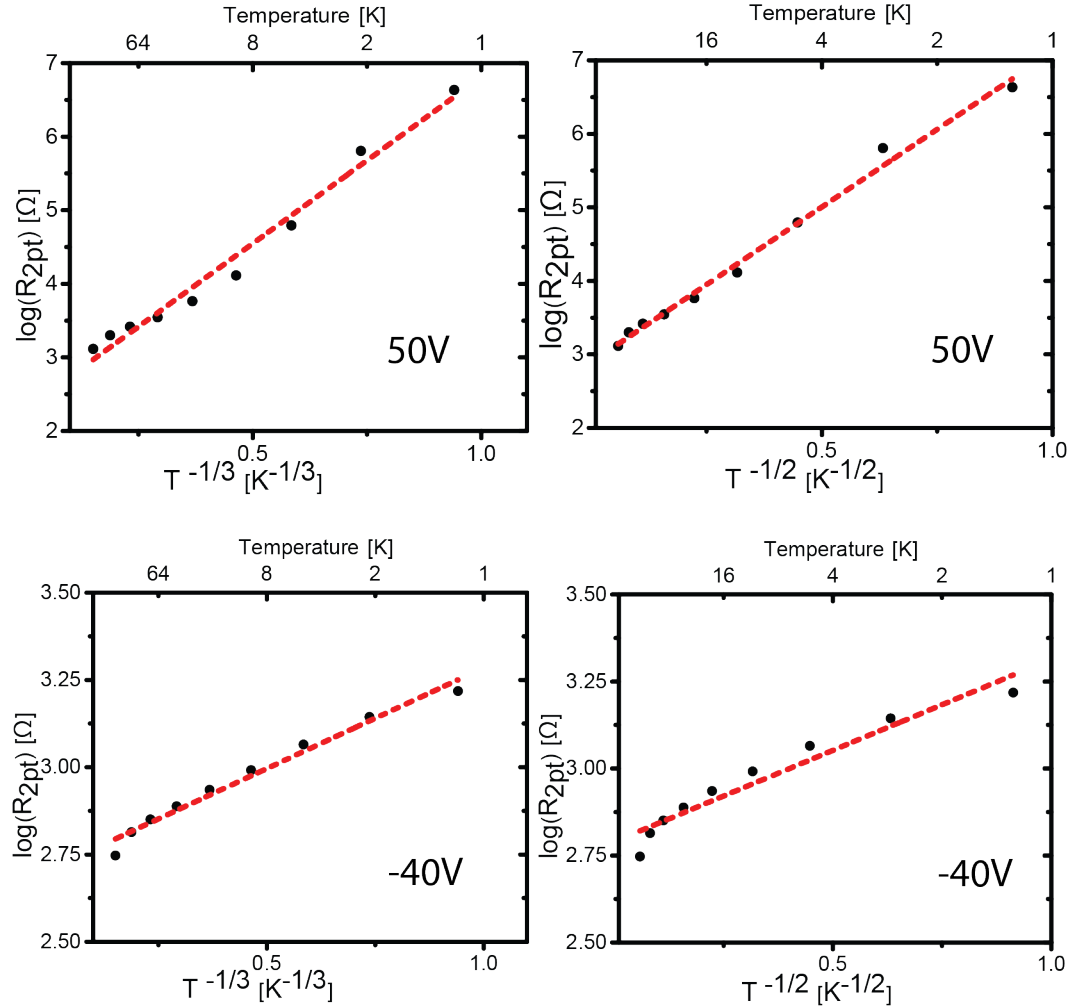


**Fig. 4.10:** Comparison of two point resistance *vs* temperature with the  $x$  axis plotted as  $T^{-1/3}$  on the left side and  $T^{-1/2}$  on the right side. The gate voltage is 50V at the top and -40V at the bottom. The quality of the fit fails to distinguish whether a Mott or Efros-Shklovskii model applies in the temperature range explored.

Looking at the fits presented in fig 4.10 the quality of the fits do not allow one to distinguish the underlying physical model for transport as corresponding to Mott VRH or ESRH. Most of the samples for which low temperature

transport has been measured show a similar behavior where there is qualitative VRH-like resistance versus temperature, but one cannot quantitatively assign a VRH or ESVRH behaviour to electron transport. The exact transport mechanism in hydrogenated graphene remains unknown.

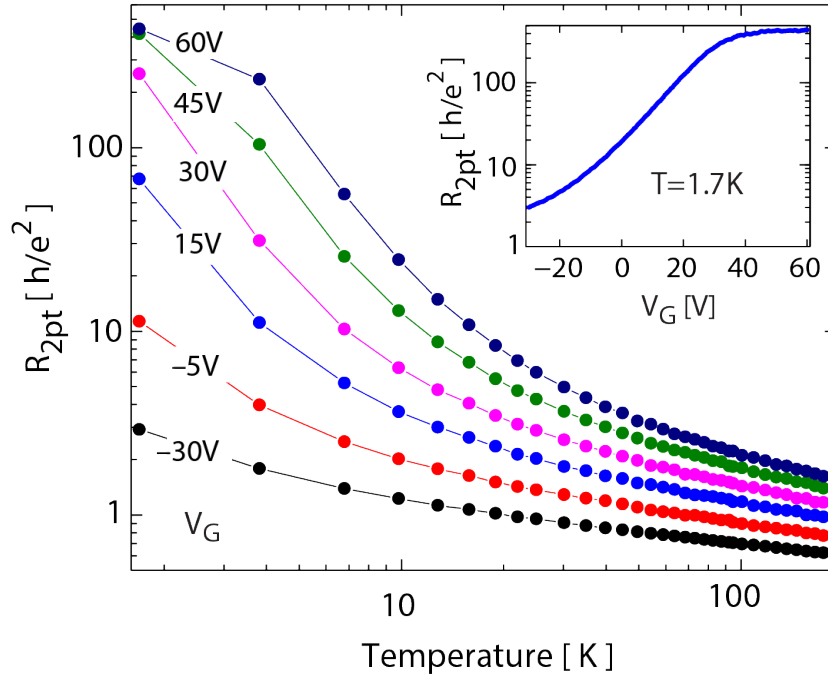


**Fig. 4.11:** Two point resistance *vs* temperature as a function of gate voltage of sample HG18. The inset shows the two point resistance as a function of gate voltage at 1.7K. There is evidence of a saturation regime at low carrier density at the lowest temperature.

Fig 4.11 shows similar transport to fig 4.9 and also fails to distinguish between VRH and ESVRH, but agrees qualitatively with the VRH model. The inset of fig 4.11 shows a resistance plateau regime observed at low carrier density and low temperatures. At the lowest temperature, both the 45V and 60V gate voltages yield approximately the same resistance. This is the case even though there are  $1 \times 10^{12} / \text{cm}^2$  more carriers in the former case, as estimated

by the parallel plate capacitive model where  $n = \epsilon\epsilon_0 V_g / t_{ox} q$ , with  $n$  as carrier density,  $\epsilon$  the permittivity of SiO<sub>2</sub> and  $t_{ox}$  the oxide thickness). This may suggest that there are at least  $1 \times 10^{12}$  carriers/cm<sup>2</sup> that are localized rather than free, as gate voltage is modulated from 45V to 60V. This observation is inconsistent with the density of states of pristine graphene, which is devoid of localized states. The resistance *vs* gate voltage also shows that as the carrier density is increased, the hydrogenated graphene becomes less strongly insulating since  $dR/dT$  then tends towards 0. This resistance plateau region has also been observed in the low charge carrier regime in several other samples.

In conclusion, the insulating behavior demonstrated by all hydrogenated graphene samples, the exponential growth of *in situ* resistance and the Raman spectra confirm that carriers become localized and translational symmetry defects are introduced to graphene by hydrogenation. The transport data suggests ambivalent agreement with VRH and ESVRH in both the high and low carrier density regimes. The emergence of a resistance saturation regime near the neutrality point is puzzling, and is investigated further with the application of a perpendicular magnetic field in chapter 6.

## Hydrogenated Graphene Based Thermometer and Bolometer

The most direct and useful applications of hydrogenated graphene use the strong temperature dependence arising from charge carrier localization. The two main applications that rely on this property are thermometers and bolometers. At low hydrogen density ( $\leq 10^{11}\text{cm}^{-2}$ ), a typical sample's resistivity is exponential at very low temperatures and the signs of the localization regime can only be perceived at 100's of mK. At higher hydrogen coverage ( $\geq 10^{11}\text{cm}^{-2}$ ) the exponential regime in resistance is observable at much higher temperatures and so the localization regime persists up to temperatures as high as 100's of K. A critical feature of this disordered system is that the temperature dependence of resistance can be controlled via the hydrogen dose.

Table 5.1 summarizes the properties of various types of thermometers where the key parameter in thermometers and one of the key parameters in bolometer is the sensitivity ( $dR/dT$ ). Fig 5.1 shows a comparison of the  $dR/dT$  values

**Table 5.1** Summary of thermometers used in low temperature environments.

Material	Range [K]	$\sigma$ mechanism	$R@4K[\Omega]$	Price [\$]
Ruthenium Oxide	[0.1, 40]	VRH	$> 1k$	[200,2000]
Zirconium Oxy-Nitride	[0.1, 300]	VRH	$\approx 1k$	[200,1000]
Doped Germanium	[0.05, 100]	VRH	$\approx 1k$	[500,2000]
Hydrogenated Graphene	[0.3, 50]	VRH	$\approx 20k$	TBD

between some of the most commonly used thermometers offered on the market and four different hydrogenated graphene devices. Fig 5.1 shows that the device with the largest  $dR/dT$  is the hydrogenated graphene device HG-D2 at 10 K which is slightly more sensitive than the doped germanium thermometer at 50 mK. The largest  $dR/dT$  is a consequence of the resistance of the device itself being large. Finally, the wide spread of  $dR/dT$  values at 10K shows that  $dR/dT$  can be tuned by hydrogen dose to meet different specifications. However, hydrogenated graphene thermometers show variable behavior on successive cooldowns.

Table 5.2 lists the hydrogenated graphene samples that were used for bolometry and thermometry measurements.

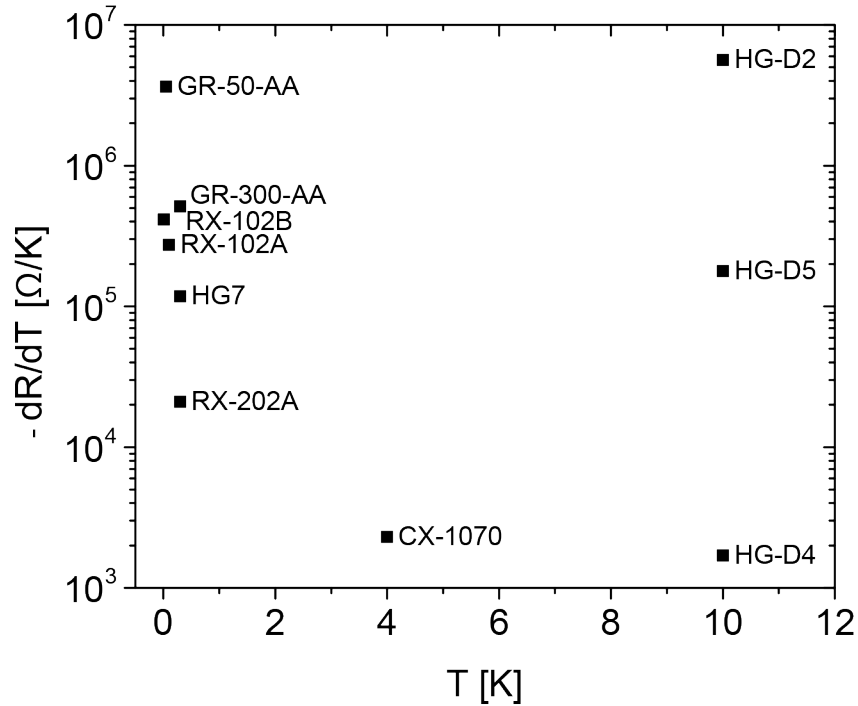


**Fig. 5.1:** Thermal sensitivity ( $-dR/dT$  at minimum temperature) *vs* temperature taken for all low temperature thermometers sold by Lakeshore compared to hydrogenated graphene. The GR series is doped germanium, RX is ruthenium oxide, and CX is zirconium oxy-nitride.

## 5.1 Hydrogenated Graphene as a Thermometer

### 5.1.1 Calibration

Typical thermometers used in low temperature measurements consist of either ruthenium oxide, doped germanium or zirconium oxy-nitride (Cernox). All three of these thermometers exhibit charge carrier transport well approximated by VRH at temperatures below 10 K and usually follow thermally activated transport above 10 K [81]. Table 5.1 indicates that the transport mechanism for all four thermometer types is the same. Some advantages that graphene has over conventional low temperature thermometers are its low heat

**Table 5.2** Summary of samples used in this chapter for fabrication of thermometers and bolometers.

Name	$dR/dT$ [ $\Omega/K$ ] at $T_{base}$	Application
HGD2	$-5.6 \cdot 10^6$	Bolometer
HGD5	$-1.8 \cdot 10^5$	Bolometer
HGD4	$-1.7 \cdot 10^3$	Bolometer
HG7	$-1.2 \cdot 10^5$	Thermometer

capacity ( $2 \cdot 10^{-21}$  J/K $\cdot\mu\text{m}^2$  at 5 K) [82], a low electron phonon coupling in graphene [82, 83, 84] and a large surface to volume ratio. Its ultra-thin film nature makes it possible to coat a reasonably flat surface of interest and thus minimize the physical distance between the thermometer and the object whose temperature is being measured.

To use graphene as a thermometer, characteristics such as sensitivity, repeatability and control of manufacturing must be demonstrated. In the following section, its high sensitivity will be demonstrated at cryogenic temperatures in the presence of a magnetic field. The first step thus required in order to use hydrogenated graphene as a thermometer is to perform the calibration of the resistance as a function of both temperature and magnetic field. To obtain these data, the field and temperature of a Janis He-3-SSV fridge were both kept at constant value until the resistance of the hydrogenated graphene device reached a constant equilibrium value to eliminate dynamic effects such as eddy current heating. For all measurements, the sourcing current was kept at 10 nA in order to prevent self heating of the device, as seen in the blue region

of fig 5.2. The data in fig 5.2 was taken on a subsequent cooldown which is why the resistance values at 300 mK are different than in other plots (*i.e.* figs 5.3, 5.4). This issue is most likely related to material stability and needs to be addressed prior to efforts at commercialization. A potential solution to be investigated in the future is to encapsulate the hydrogenated graphene surface.

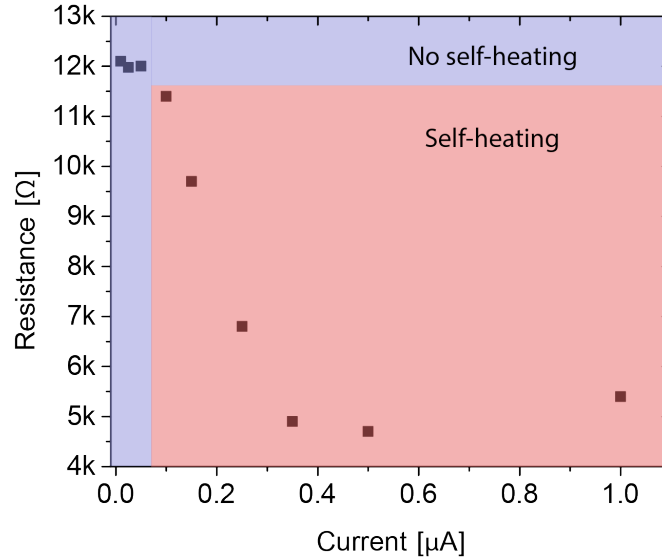


**Fig. 5.2:** Resistance *vs* bias current of HG7 at 300 mK on a subsequent cooldown. Sourcing currents of 10, 20 and 50 nA show no signs of self heating (blue region). The sourcing currents in the red region show signs of self heating.

The calibration of the resistance as a function of both temperature and magnetic field is shown in fig 5.3. Thermometers used at low temperatures are often used in systems with magnetic fields. It is therefore important to calibrate the effect of the magnetic field on the thermometer. An interpolation was done by a fourth order spline function to find resistance values where data points were not taken in temperature and magnetic field. The graphene resistance  $R$  was fit to the form  $\ln(R) = \sum \alpha_{m,n} \cdot B^m \cdot (1/T)^n$ , with the coefficients  $\alpha_{m,n}$  for  $m, n \leq 4$  determined by a least-squares fit over  $0.3\text{K} < T < 1.2\text{K}$  and

$0\text{T} < B < 9\text{T}$ . The hydrogenated graphene based thermometer's calibration was accurate such that the maximum deviation between the interpolated and measured temperature values was  $\approx 15\text{ mK}$ .

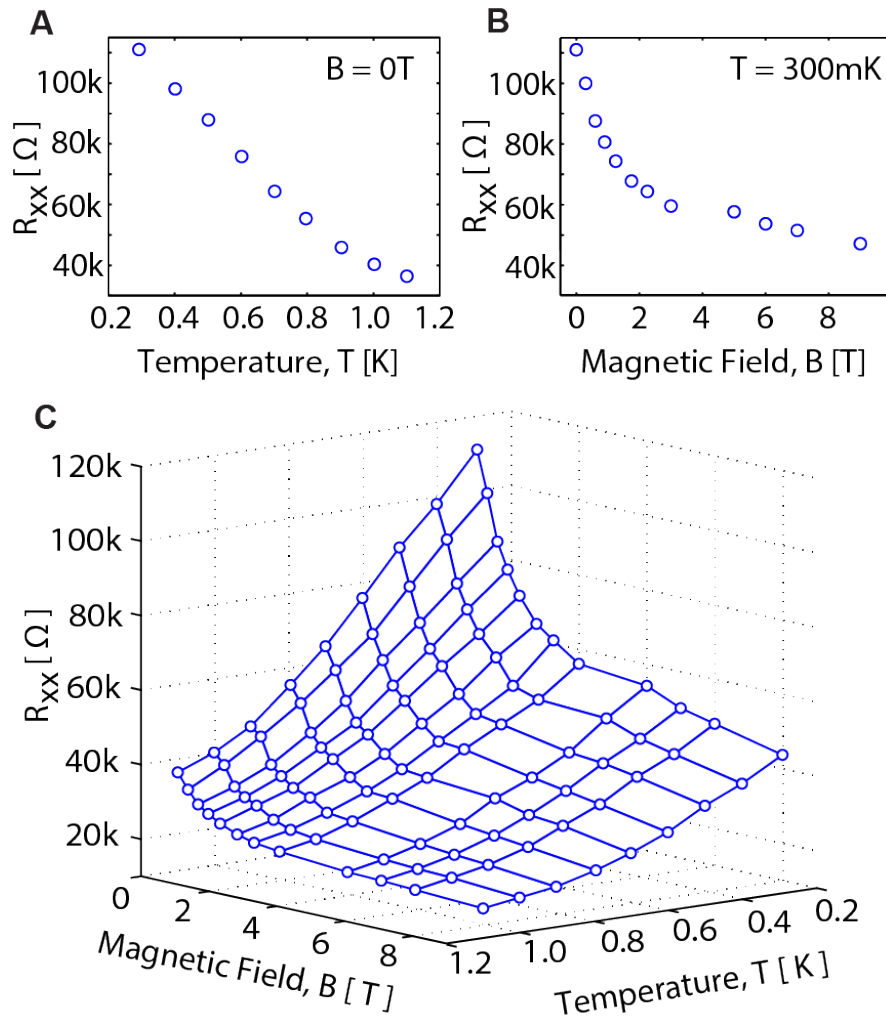


**Fig. 5.3:** A: Calibration of  $R$  vs  $T$  at  $B = 0\text{ T}$ . B: Calibration of  $R$  vs  $B$  at  $T = 300\text{ mK}$ . C: Calibration of the hydrogenated graphene thermometer in both  $T$  and  $B$ . The device measured is HG7.

### 5.1.2 Adiabatic Demagnetization Cooling

To test hydrogenated graphene as a thermometer, a measurement of the heating and cooling of a doped silicon wafer acting as a paramagnetic heater / refrigerator was performed. The set-up is such that the hydrogenated graphene device is sitting atop 300nm of SiO<sub>2</sub> and 500 $\mu$ m of doped silicon underneath. The hydrogenated graphene thermometer is in thermal contact with the silicon back gate. The As doped silicon back gate acts as a paramagnetic medium such that the electrons spins bound to the donor impurity atoms can undergo adiabatic demagnetization cooling. The entropy of donor-bound electron spins in heavily doped silicon dominates over both phonon entropy and electron gas entropy at low temperatures and moderate magnetic fields [85, 86], thus enabling effective cooling by demagnetization. Any minute temperature changes in the doped silicon should therefore be measured by the hydrogenated graphene device. The thin SiO<sub>2</sub> oxide has a relatively large thermal conductance ( $\kappa_{SiO_2} \approx 10^{-5}$ W/cm · K at 300mK) [87] such that  $\kappa_{SiO_2} \cdot A/L \approx 0.3$ W/K. This large thermal conductance allows the hydrogenated graphene thermometer to be approximately thermally shorted to the doped silicon. Despite a relatively large resistance (100's of k $\Omega$ ), the thermometer is experimentally measured to respond rapidly to temperature changes occurring in the doped silicon substrate (10's of seconds). The resistance of the hydrogenated graphene device was measured as the magnetic field was swept. Fig 5.4 shows the effect of sweep rate on the magnetoresistance compared to the value when both temperature and magnetic field are static.

The phenomena underlying the results shown in fig 5.4 is the expected

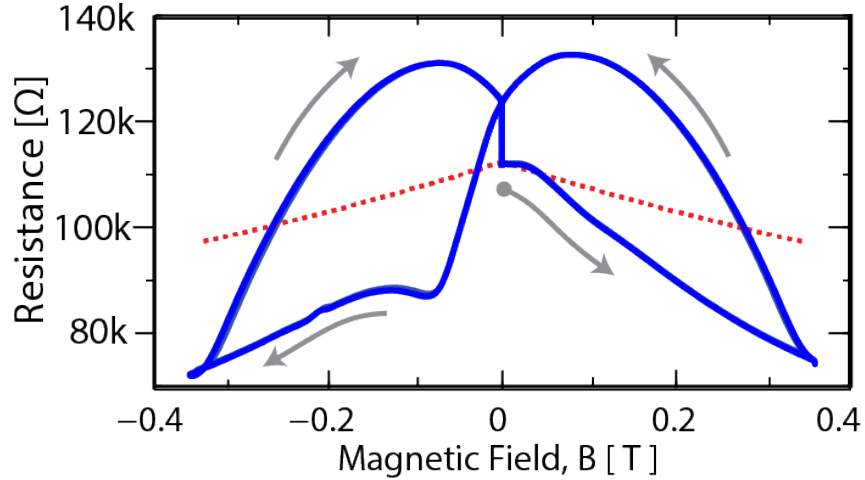


**Fig. 5.4:** Dynamic magnetoresistance with sweep rate at 0.225 T/min (blue) with the steady state values (red). The grey arrows represent the order in which the magnetic field was swept. The device measured is HG7.

adiabatic demagnetization cooling of the electron spins bound to the donor impurity atoms. The operating principle of this refrigerator is the same as a paramagnetic salt demagnetization stage used to extend the base temperature of dilution refrigerators. The heating in the device is explained by the relaxation of spin split states to the ground state and the cooling is explained by the demagnetization of the spins as the magnetic field is reduced towards zero field.

The four steps of adiabatic demagnetization cooling can be observed from the magnetoresistance curve in fig 5.5 taken at 300 mK and comparing the dynamic magnetoresistance (black) to the calibration values (blue). It is also possible to observe the full spin polarization of the demagnetization stage at approximately 4 T.

Subtracting the calibration curve from the dynamic resistance curve (black minus blue curve in fig 5.5) yields the temperature difference. Performing these

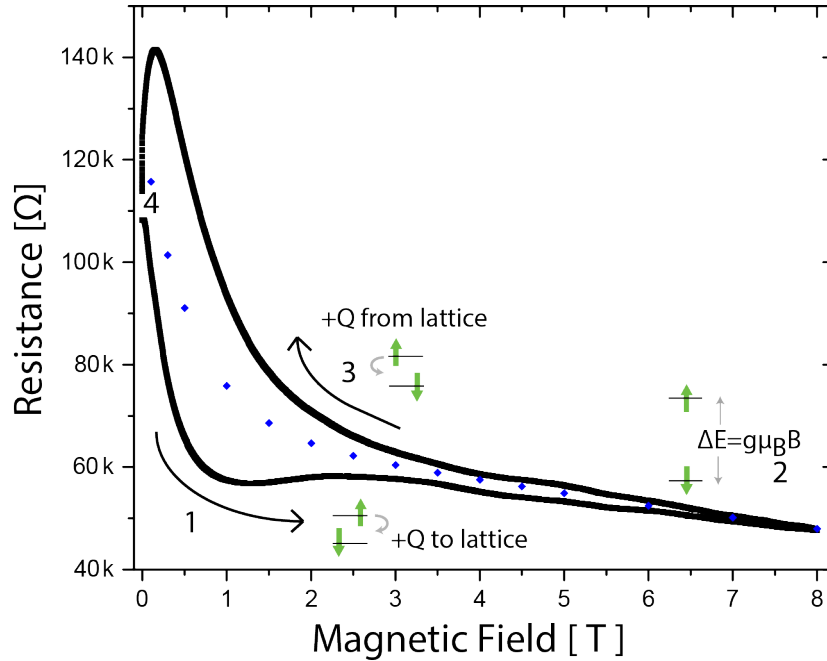


**Fig. 5.5:** Magnetoresistance (black) with the steady state value (blue). The sweep rate is 0.225 T/min. The device measured is HG7.

operation on data sets taken at different temperatures results in fig 5.6.

As can be seen from fig 5.6, the hydrogenated graphene thermometer is effective at measuring changes in the temperature of the doped silicon. The main impediment to commercializing this thermometer is the reliability upon successive cooldowns. The calibration curves measured for this device in fig 5.3 were inaccurate for subsequent cooldowns.

To summarize, hydrogenated graphene, once properly calibrated, can be used as a thermometer sensitive to  $|T_{Rox} - T_{HG}| \approx \pm 5$  mK based on the deviations of the hydrogenated graphene thermometer from the calibrated ruthenium oxide thermometer. The main problems with using hydrogenated graphene as a thermometer are its different behaviors upon thermal cycling

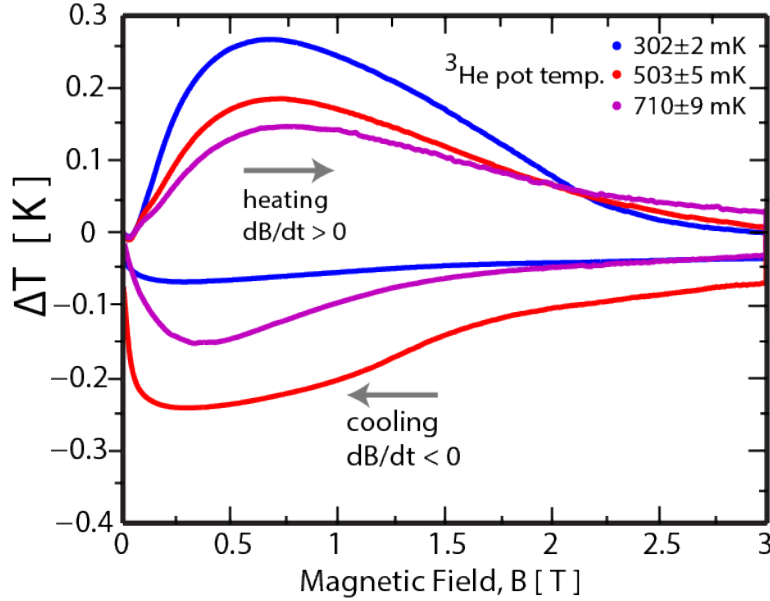


**Fig. 5.6:** Dynamic cooling of the demag stage at different temperatures. The sweep rate is 0.225 T/min. The device measured is HG7.

and the lack of predictability of temperature dependent transport based on hydrogenation time. As explained in chapter 4, this topic requires future investigation to fully understand the process by which defects mediate change in temperature dependent transport, and how defect density itself can be controlled. The main advantage with using hydrogenated graphene as a thermometer is its large and tuneable sensitivity  $dR/dT$ .

## 5.2 Hydrogenated Graphene as a Bolometer

Current bolometers available on the market for astronomy applications are typically made of silicon and achieve a responsivity of  $10^5$  V/W [88]. The operation principle of a bolometer is to have impinging radiation heat the absorbing medium and to have a sensitive resistive thermometer detect the

change of temperature due to the absorption of the radiation. For this experiment, the silicon is the absorbing medium and the hydrogenated graphene is the thermometer. Because of the weak electron phonon coupling present in graphene and its small electron heat capacity [82], it is possible that graphene's performance could exceed that of current bolometers in the THz range. It is also theoretically predicted that introducing disorder would further modify the electron phonon coupling [89]. Recently, it was experimentally demonstrated that bi-layer graphene could be used as a bolometer by making use of the gap that emerges in bilayers under appropriate conditions [90]. Generally speaking, the change of temperature of the electrons resulting from heating by absorption of radiation

$$T(P) - T(0) = \frac{\epsilon P}{\sqrt{G_{th}^2 + \omega^2 C_{th}^2}}, \quad (5.1)$$

where  $\epsilon$  is the emissivity,  $P$  is the impinging power,  $C_{th}$  the heat capacity and  $G_{th}$  the thermal conductance. Despite its small thermal conductance, hydrogenated graphene can still have a quick response due to its extremely small heat capacity. Therefore, to maximize  $\Delta T$ , it is intuitive to minimize the heat capacity and minimize thermal conductance. This ensures that the heat accumulated in the material will not dissipate too quickly. To maximize the voltage responsivity ( $R_V$ ), as shown in eq 5.2, it is important to have the largest  $dR/dT$  and  $\Delta T$ ,

$$R_V = \frac{I_{bias}(dR/dT)\Delta T}{P}, \quad (5.2)$$

Hydrogenated graphene could be an optimal material because of the large thermal resistance between its charge carriers and the rest of its environment, thereby allowing for the build up of a large temperature difference between the hydrogenated graphene's charge carriers and the environment.

State of the art sensors come in two forms, either superconducting transition edge sensors or doped germanium and silicon which achieve responsivities of  $10^8$  V/W and  $10^5 - 10^7$  V/W at  $\approx 160$  mK and  $\approx 2.5$  K respectively [91, 88]. The principle of operation of transition edge sensors is that a small change in heat causes the material to undergo a transition from a superconducting state to a resistive state, leading to a very large  $dR/dT$ , but a limited temperature range. The principle of operation for the doped silicon and germanium is to have the sample's doping close to its metal insulator transition where its  $dR/dT$  will be maximal. When this is the case, a small amount of heat will generate a large change in resistance. The neutron transmutation doping used in doping silicon and germanium has been well characterized over the years [92] and results in highly predictable performance. For hydrogenated graphene, the doping process has not yet been completely characterized and still suffers from inhomogeneity across the sample, as shown in chapter four.

Important to the characterization of both thermometers and bolometers is the measurement of both  $dR/dT$  and  $dR/dP_i$  in order to obtain the thermal resistance of hydrogenated graphene.

### 5.2.1 Thermal Resistance Characterization

To understand the efficiency of the hydrogenated graphene bolometer, we measure the thermal resistance  $R_{th} = 1/G_{th}$  to the environment. To perform thermal resistance measurements, the hydrogenated graphene devices were mounted on ceramic carriers which were in turn mounted on 16 pin G-10 headers. A copper thermal link was created between the cryostat cold head and the G-10 header. The cryostat used was a closed cycle 10K optical cryostat (Janis CCS-150) where the temperature uncertainty on the cold head was  $\approx \pm 0.1\text{K}$ . A semiconductor parameter analyzer (Agilent B1500) was used to measure the electronic characteristics of the sample. A two point measurements configuration was used to measure current while sourcing 10mV DC source-drain voltage. A schematic of the sample and its heat dissipation channels is shown in fig 5.7. The first step was to measure the temperature dependence of the samples as shown in fig 5.8.

The value of  $dR/dT \approx -5.6 \text{ M}\Omega/\text{K}$  was obtained for HGD2 and it is the largest of all four samples measured. This value of  $dR/dT$  is obtained at the smallest carrier density for HGD2. This temperature dependent resistance, similar to the data shown in the previous chapter, does not quantitatively fit to either Mott VRH, Efros-Skhlovskii VRH or thermally activated transport. To measure  $R_{th}$ , we measure  $dR/dT$  and  $dR/dP_i$ , where  $P_i$  is the internal Joule heating,

$$R_{th} = \frac{dT}{dP_i} \approx \frac{dR/dP_i}{dR/dT}. \quad (5.3)$$

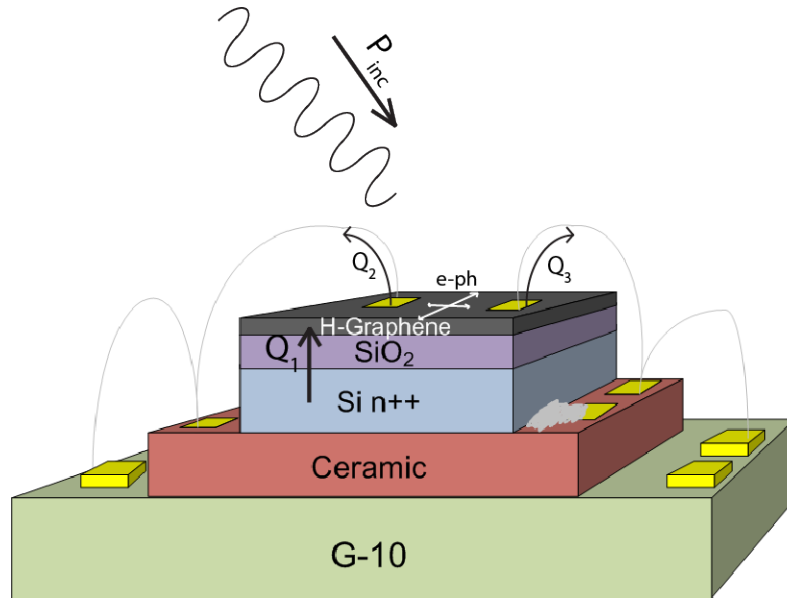


**Fig. 5.7:** Schematic of the sample being exposed to incoming radiation and the various channels through which heat can be dissipated.

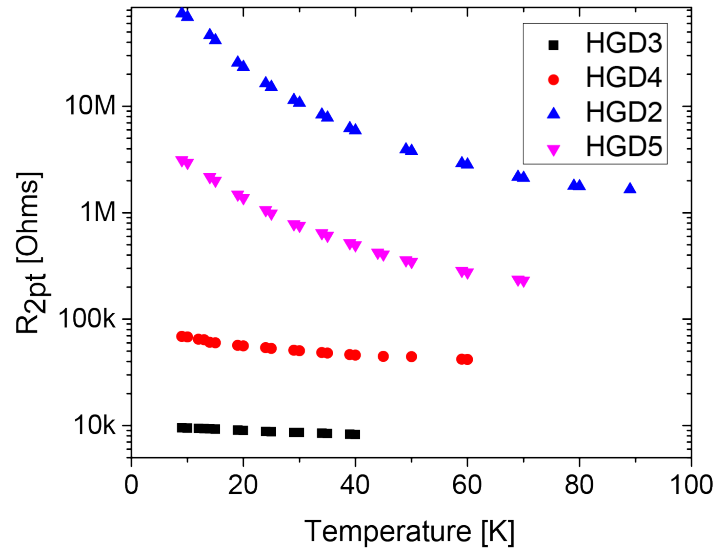


**Fig. 5.8:**  $R_{2pt}$  of four devices as a function of temperature. The carrier density was minimized for each sample.

To measure  $dR/dP_i$ , a calibration of the resistance versus bias voltage was measured. Firstly, the device was calibrated at every Kelvin in the range of

interest (9-30K). Then, at fixed cryostat temperature, the bias current was increased to self heat the device. Fig 5.9 is a plot of the inferred electron temperature versus the Joule heating induced by increasing the bias voltage. The hypothesis used to create this plot is that all the power pushed into the device goes towards self heating and is not caused by a non-linear IV curve.

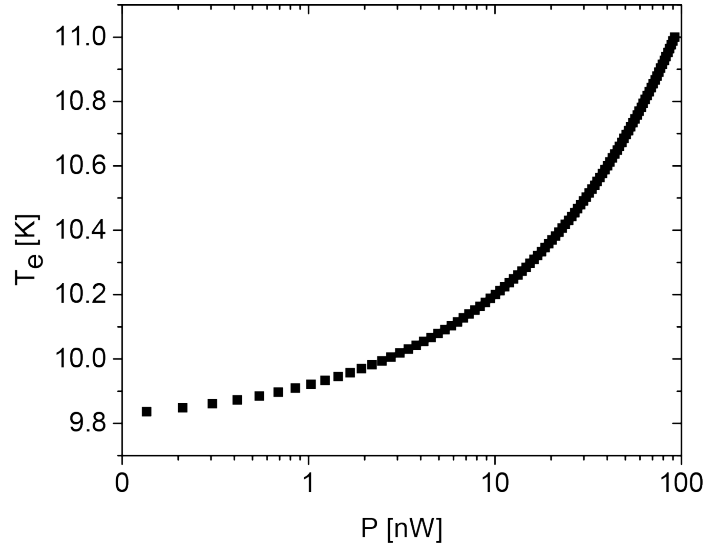


**Fig. 5.9:** Extracted electron temperature *vs* applied electrical power for HGD5 with base temperature 9.8K.

From these calibrated plots of  $R$  *vs*  $T$  and  $R$  *vs*  $P_i$ , it is now possible to calculate the thermal resistance in the devices as shown in fig 5.10. The maximum value of thermal resistance value obtained for HGD2 is  $R_{th} = 3\text{K/nW}$ . To give a sense of comparison, one meter of 30 gauge copper (0.225 mm diameter) has a thermal resistance of  $R_{th} = 3.2 \times 10^{-10}\text{K/nW}$  at room temperature.

To ensure that the cause of this effect was not a weak thermal link between the sample and the cryostat's cold head, the hydrogenated graphene was replaced with a germanium sample of similar dimensions but thicker (0.5 cm by 0.5 cm by 500  $\mu\text{m}$  thick), where a  $R_{th} = 4.8 \cdot 10^{-7}\text{K/nW}$  was measured.

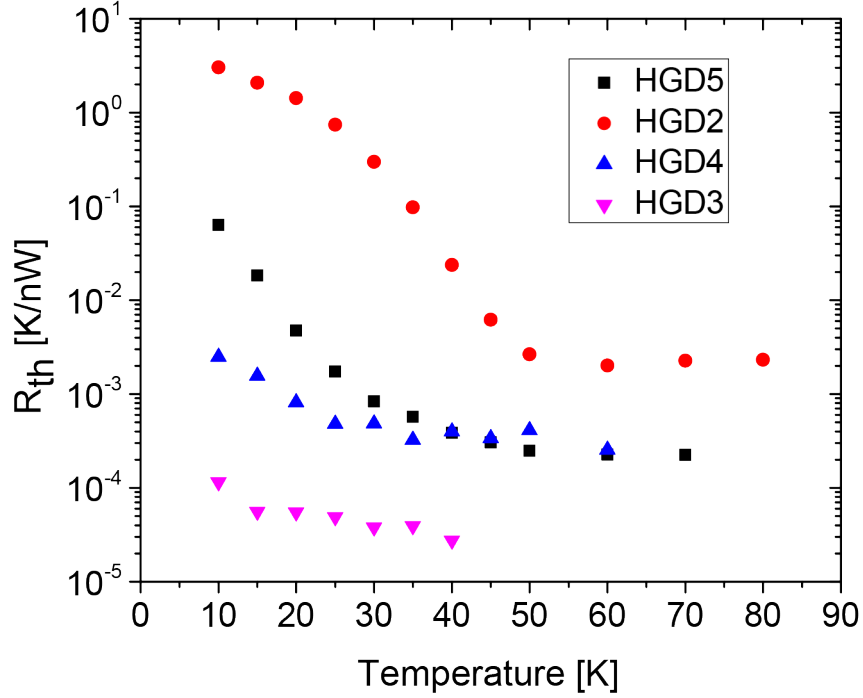


Fig. 5.10:  $R_{th}$  vs temperature for all devices.

It is therefore possible to rule out a poor thermal link between the cryostat and the sample. Remaining causes of the high thermal resistance could be the graphene oxide interface or high thermal resistance of oxide. However other work shows that the value of thermal resistance for 300 nm thick and one mm<sup>2</sup> of SiO<sub>2</sub> is  $R_{th} = 3 \times 10^{-11}$  K/nW at  $\approx 1$  K [87]. The value of the predicted thermal resistance of the interface (or Kapitza resistance) between graphene and silicon oxide is  $R_{th} = 1.5 \times 10^{-11}$  K/nW at 10K using the  $T^3$  extrapolation [93]. The doped silicon back gate has a dopant density that makes it metallic even at 0.3K and a thermal resistance of  $R_{th} = 8.5 \times 10^{-11}$  K/nW for 500  $\mu$ m at 10K using the Wiedemann-Franz law. It has also been calculated that the out of plane thermal resistivity of graphene is much higher than its in plane thermal resistance by roughly two orders of magnitude at room temperature

( $1.4 \cdot 10^{-10}$  vs  $1.4 \cdot 10^{-12}$  Km/nW) [94]. A possible explanation for the large thermal resistance of hydrogenated graphene is thus the decrease of in plane thermal transport owing to the presence of defects induced by hydrogenation. Indeed, calculations show that defects can alter the electron-phonon coupling in graphene with the Ioffe-Regel parameter  $k_F \lambda \gg 1$  [89]. It is thus likely that in the strongly disordered limit where  $k_F \lambda \ll 1$ , the electron phonon coupling may be dramatically altered by electron localization. These theoretical predictions could lead to an even weaker electron-phonon coupling and thus a higher thermal resistance.

### 5.2.2 Responsivity

To perform the responsivity measurements, a SiC globalar was heated between 300-1000K and focused through a thalium bromo-iodine window (KRS-5, transmission 0.7-30 $\mu$ m) on to the hydrogenated graphene samples. The incident power was measured with a thermopile (Excelitas TPD 1T 0514). The thermopile cannot measure radiation with wavelength  $\lambda < 6\mu$ m, so the incident power was estimated using Planck's blackbody radiation formula at the temperature of the globalar. The temperature of the globalar was determined from the manufacturer's calibration of temperature versus applied power. Visible light was experimentally found to have no impact on device response. It was then possible to measure bolometric response by irradiating the devices with the globalar, with results shown in fig 5.11

The largest responsivity  $10^5$  V/W corresponds to the smallest incident power of 9  $\mu$ W. This measurement was achieved by biasing the device with

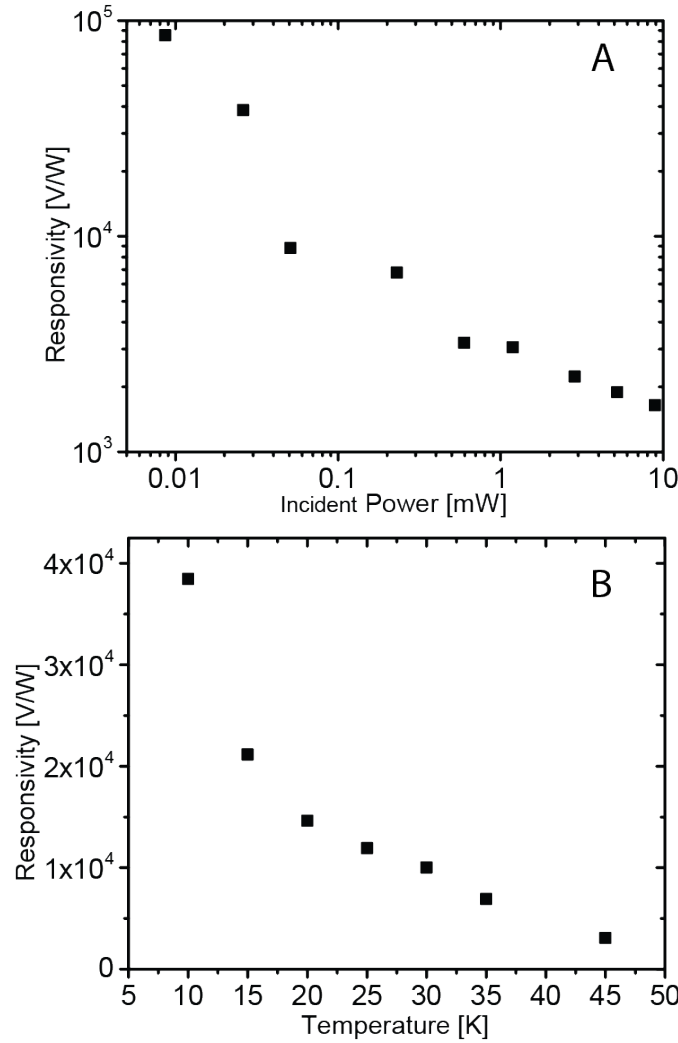


**Fig. 5.11:** A: Responsivity *vs* impinging global power at 10 K with  $9 \mu\text{W}$  of incident power for HGD2. B: Responsivity *vs* cryostat temperature with  $25 \mu\text{W}$  of incident power for HGD2.

an optimally chosen current, making a compromise between maximizing bias to maximize the signal and minimizing the bias to minimize self-heating. A maximum response was found by exposing the device to black body radiation from the room at 300K. Fig 5.11 shows that as incident power is increased there is a decreasing value of responsivity. This is a direct consequence of the

fact that the device is heated and so  $dR/dT$  is reduced.

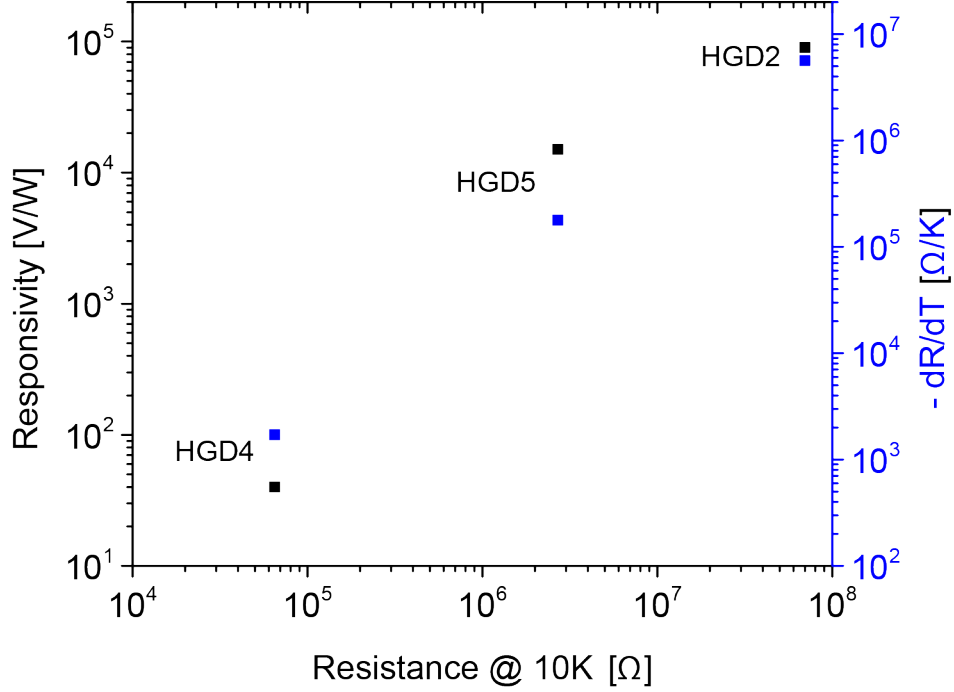


**Fig. 5.12:** Comparison of responsivity (black) and  $dR/dT$  (blue) as a function of two point resistance at 10K for the three surviving devices.

Fig 5.12 shows that increasing the electrical resistance and thus  $dR/dT$  by operation at lower temperatures further improves bolometer responsivity. Given that increased electrical resistance correlates with increased thermal resistance, introducing more defects via hydrogenation improves detector performance.

HGD2 achieves a responsivity of  $\approx 10^5$  V/W at 10K and compares advantageously to commercially available silicon bolometers which have responsivities of  $10^5 - 10^7$  V/W at operating temperatures between 1.6 and 4.2 K [88]. Given that there is a strong correlation between device resistance, thermal resistance

and  $dR/dT$ , one way to improve performance would be to hydrogenate the devices further. However, since the measurements are electrical, it is important to hydrogenate such that  $R < \approx 1G\Omega$  to ensure that electronic conduction is dominated by hydrogenated graphene rather than parasitic leakage conduction through wiring or the oxide substrate.

## Magnetoresistance of Hydrogenated Graphene

It is a matter of debate as to whether Anderson or Mott insulators exhibit positive or negative magnetoresistance under an applied perpendicular magnetic field [95, 96, 97, 98, 99]. In the specific case of disordered graphene, the observation of negative magnetoresistance has been common in fluorinated [36], oxidized [37] and hydrogenated [42, 39] graphene. Our observation of negative magnetoresistance as a transition from insulating state to a quantum Hall state is the result of an interplay between disorder and magnetic confinement. The experiments presented in this chapter answer a question posed by Sankar Das Sarma which reads: *A far more interesting situation would be to pick a system that is strongly localized ( $k_F\lambda_D \ll 1$ ) at 0 T and to create delocalized states via the application of a B field. The natural question then arises about whether one would observe at finite fields the quantized Hall conductance phenomenon in a high disorder strongly localized (at 0 T) 2D system as the B field is increased* [64].

The quantum Hall effect had previously been observed in high mobility GaAs/AlGaAs gated to subthreshold densities to increase the Ioffe-Regel dis-

order parameter and generate insulating like behavior ( $dR/dT < 0$ ). By dramatically reducing carrier density ( $n \approx 10^{10}\text{cm}^{-2}$ ), a disordered regime of transport is recovered at dilution fridge temperatures (10's to 100's of mK) [100, 101]. Refined experiments increased the maximum carrier density at which insulating type behavior was observed ( $n \approx 10^{11}\text{cm}^{-2}$ ), a direct result of increased disorder, and thus the temperature at which the quantum Hall effect could be observed was increased to  $\approx 1$  K [102]. In all three of these papers, disorder is never purposely introduced, but is rather dependent on the purity of the growth. A fundamental question that arises is whether the quantum Hall effect is robust to arbitrary amounts of disorder. This will be investigated here.

Presented in this chapter are results from four hydrogenated graphene samples inserted in large DC magnetic fields at the NHMFL. The quantum Hall effect at  $\nu = -2$  is observed in the most disordered sample to date, as characterized by a Ioffe-Regel parameter of  $\approx 250$ . A magnetic field dependent localization of charge carriers, a transition from insulating like behavior to a quantum Hall state and a positive magnetoresistance in parallel magnetic field configuration were observed.

## 6.1 Measured Samples

Table 6.1 summarizes the basic properties of the samples whose data is shown in the later parts of the chapter. As noted in chapter four, the correla-

tion between hydrogenation time and electrical resistance is poor.

**Table 6.1** Summary of the properties and measurements for the four samples measured in high fields. These all share a two point geometry.

Name	$R$ @ 300K [ $\Omega$ ]	$R$ @ Base [ $\Omega$ ]	H time [min]	Configurations
HG18	110k $\Omega$	1.8M $\Omega$ at 0.3 K	12	$\parallel, \perp$ 33 T
HG33	17k $\Omega$	6.5M $\Omega$ at 0.6 K	6	$\perp$ 45 T, dV/dI
HGT2	4.5k $\Omega$	35k $\Omega$ at 1.5 K	8	$\perp$ 70 T
7H5m	17k $\Omega$	18k $\Omega$ at 1.5 K	5	$\perp$ 60 T

Fig 6.1 shows the temperature transport data for HG-33. All other hydrogenated graphene samples exhibit the same insulating behavior, *i.e.*  $dR/dT < 0$ , as well as hole type conduction at zero gate voltage. The inset of fig 6.1 also shows a zero field resistance plateau region that will be explored in more detail in later sections. Fig 6.2 shows a similar resistance plateau region for HG-18.

As shown in fig 6.2, the effect of an applied magnetic field is orientation dependent. When the field is parallel to the graphene plane, the gate voltage width of the resistance plateau is increased by positive magnetoresistance, but when the field is perpendicular to the graphene plane, the resistance plateau width is reduced by negative magnetoresistance.

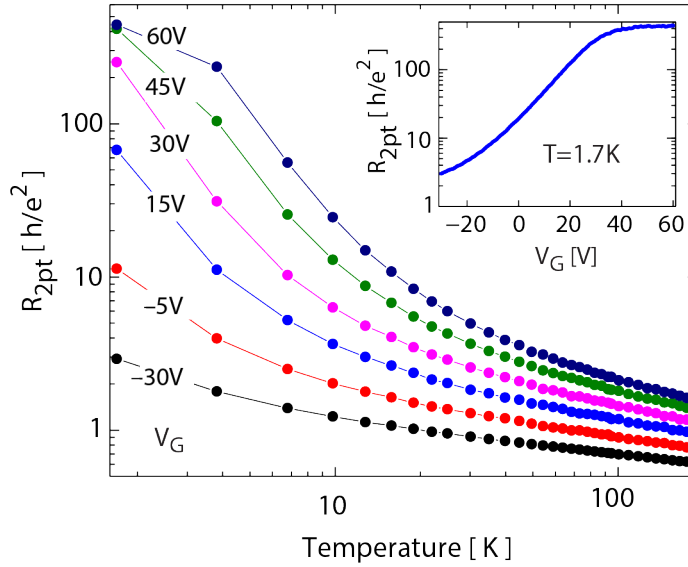


**Fig. 6.1:** Resistance  $R_{2pt}$  vs temperature for different gate voltages  $V_G$  of sample HG-33. The inset shows the resistance  $R_{2pt}$  vs gate voltage  $V_G$  at the base temperature of 1.7 K.

## 6.2 Magnetoresistance in a Parallel High Magnetic Field

### Field

It is found that hydrogenated graphene has a positive magnetoresistance under parallel magnetic field conditions. Specifically, at higher carrier density, the magnetoresistance is found to increase by a factor of four whereas no change in the magnetoresistance is observed at low carrier density. Finally, the positive magnetoresistance is found to reduce in magnitude as the temperature is increased.

In the following section, the measurements of HG-18 in a 33T magnet are described with the parameters of the experiment explained in chapter three.

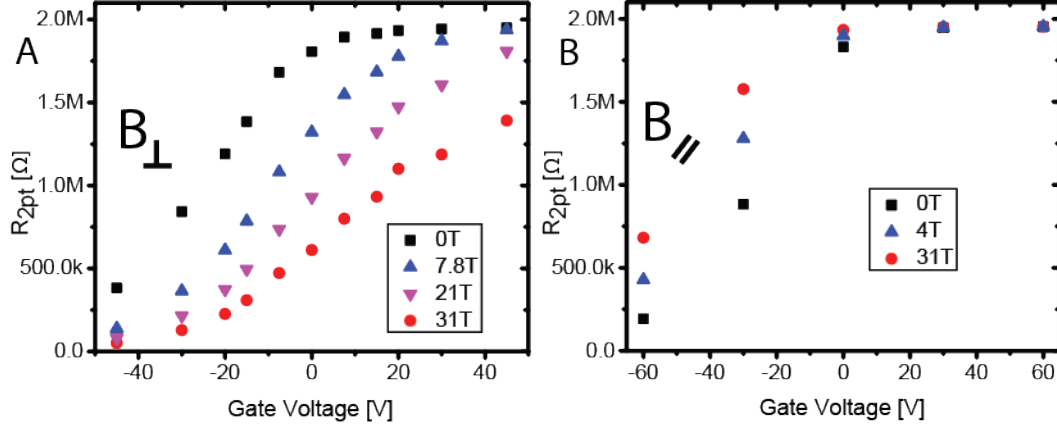


**Fig. 6.2:** A: Resistance  $R_{2pt}$  vs gate voltage for a perpendicular magnetic fields for sample HG-18. B: Resistance  $R_{2pt}$  vs gate voltage for a parallel magnetic field for sample HG-18. The parallel magnetic field increases the resistance plateau and the perpendicular one reduces the resistance plateau. All data was taken at  $\approx 300$  mK.

The upper bound for the misalignment between magnetic field and graphene plane is  $\approx 0.5^\circ$ . This sample has a zero field resistance of  $\approx 70 h/e^2$ , which is far above the Ioffe-Regel limit for metallic conduction. As expected, this sample behaved like an insulator as determined by from its temperature dependent resistance (not shown). Fig 6.3 shows that upon an increase in carrier density, a larger positive magnetoresistance is observed. Both low carrier density gate voltages of 30V (not shown) and 60V show very small magnetoresistance in the parallel field configuration. In contrast, at a gate voltage of -60V, the zero field resistance is 193 k $\Omega$  and increases to 350% of its initial value or 689 k $\Omega$  which is still far from the resistance plateau value shown in fig 6.2,  $\approx 2M\Omega$ .

A possible theoretical explanation for this effect was proposed [98, 99] such that in the hopping conduction regime, when carriers attempt to hop to another energy state, the Pauli exclusion principle can become effective at

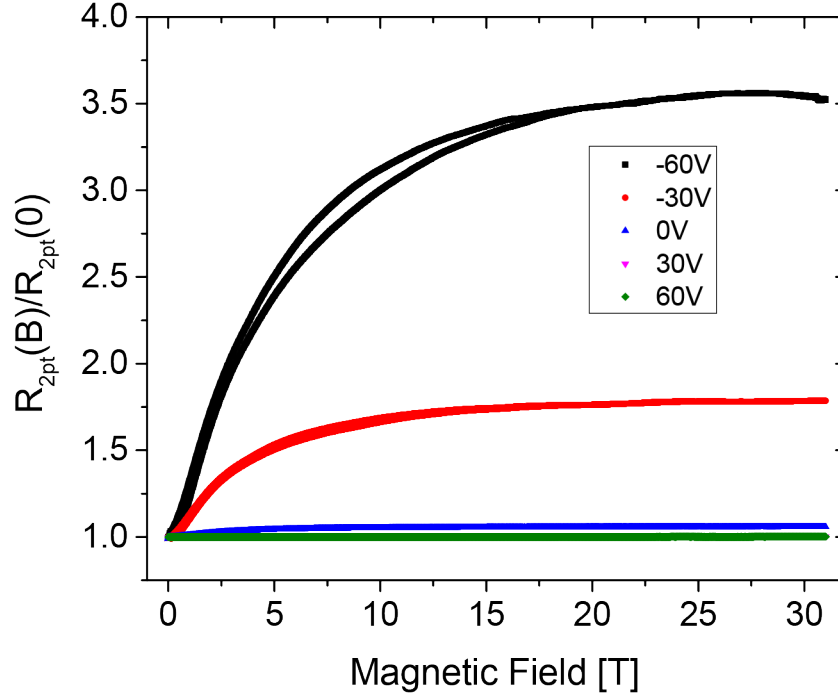


**Fig. 6.3:** Normalized two point resistance  $R_{2pt}$  vs parallel magnetic field for different gate voltages  $V_G$  for sample HG-18. The low carrier densities exhibit no change in resistance as a function of parallel magnetic field in contrast to the high carrier densities. Data was taken at  $\approx 300\text{mK}$ . Both sweep directions are plotted.

blocking the hop as a result of the spin polarization of localized states. At sufficiently high temperatures, the thermal energy can be made comparable to Zeeman energy, *i.e.*  $k_B T \approx g\mu_B B$ . Thus as temperature is increased, the positive magnetoresistance is expected to decrease with the depolarization of localized spins. Fig 6.4 shows the experimental parallel field magnetoresistance at different temperatures for the highest carrier density.

From the temperature dependence presented in Fig 6.4, it can be seen that the positive contribution to the magnetoresistance indeed decreases as the temperature is increased. We note that  $g\mu_B B = kT$  at  $B = 25\text{T}$  results in  $T = 33\text{K}$  for  $g = 2$ , as expected from a low  $Z$  material such as graphene. The

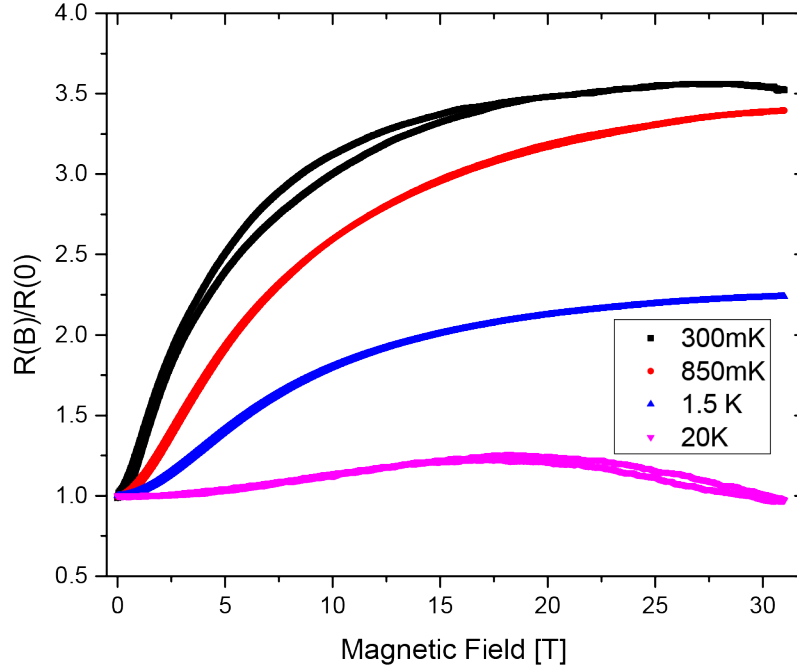


**Fig. 6.4:** Normalized two point resistance  $R_{2pt}$  vs parallel magnetic field at  $-60V$  gate voltage for different temperatures for sample HG-18. Increasing the temperature reduces the positive magnetoresistance. Both sweep directions are plotted.

dramatic reduction of the positive magnetoresistance at  $T = 20K$  is consistent with the hypothesis that the origin of the effect is due to spin polarization of localized states. However, there is presently insufficient experimental evidence to uniquely identify the origin of the positive magnetoresistance in the parallel field configuration.

## 6.3 Magnetoresistance in a Perpendicular High Field

### 6.3.1 Quantum Hall Effect

The application of a perpendicular field modifies electron transport primarily through the orbital degree of freedom, meaning the physics of Lorentz force

or Landau levels as previously described. The  $\nu = -2$  quantum Hall effect was observed in hydrogenated graphene. More generally, hydrogenated graphene was measured to have truly colossal negative magnetoresistance when a perpendicular magnetic field is applied. The localization of carriers was also found to depend on magnetic field. A transition from metallic-like to insulating-like behavior was observed as a function of magnetic field and carrier density.

In the following section, the measurements of HG-33 are described up to 45T in the hybrid resistive-superconducting magnet at the NHMFL in Tallahassee with the parameters of the experiment presented in chapter three. This sample has a zero field resistance of  $\approx 250 h/e^2$ , which is far above the Ioffe-Regel limit for metallic conduction. HG-33 also behaves like an insulator as shown in fig 6.1 ( $dR/dT < 0$ ). Fig 6.5 also shows  $R_{2pt}$  as a function of magnetic field and gate voltage, at base temperature ( $\approx 550\text{mK}$ ).

In fig 6.5, the resistance plateau is clearly observed up to 17.5T. As the magnetic field is increased, the gate voltage width of the plateau reduces. Oscillations of resistance versus carrier density begin to appear at 25T. Fig 6.6 shows the  $\nu = -2$  quantum Hall state at 45 T when the gate voltage is swept.

The inset of fig 6.6 shows a zoom-in where the resistance takes the value of  $R_{2pt} = 12\,962 \, \Omega$  which is within 0.5% of  $h/2e^2 = 12\,906 \, \Omega$ . In a quantum Hall state, the longitudinal four point resistance  $R_{xx} \rightarrow 0$  and the two point resistance approaches the transverse resistance  $R_{2pt} \rightarrow |R_{xy}|$ . The behavior of  $R_{2pt}$  is fully consistent with a Hall component admitting the quan-

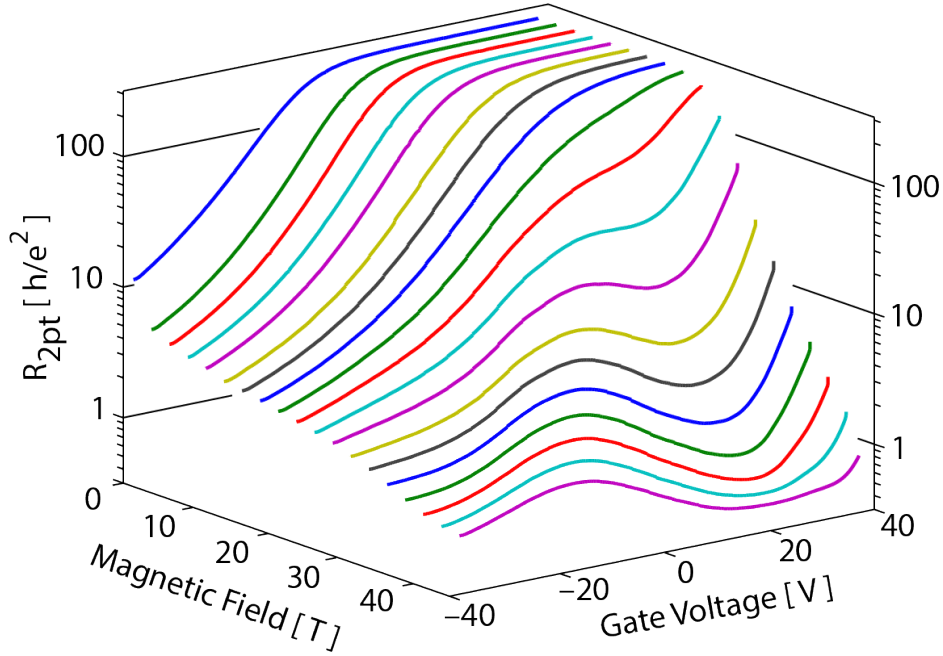


**Fig. 6.5:** Resistance  $R_{2pt}$  vs perpendicular magnetic field and gate voltage at  $\approx 550\text{mK}$  for sample HG-33.

tized value  $R_{xy} = 2h/e^2$ . From the known anomalous QH series of graphene  $R_{xy} = \pm h/4e^2(N + 1/2)^{-1}$ [26, 103], the hole doping of the sample, and an assumption of preserved spin and valley degeneracies, this QH state corresponds to the  $N = -1$  LL index. Recall that two conditions to observe the quantum Hall effect is temperature smaller than the Landau level separation and that the disorder broadening of those Landau levels still allows for splitting of the Landau levels at a given magnetic field. Notably, no Shubnikov-de Haas oscillations in resistance are observed as this QH state emerges directly from an insulating state. A potential explanation to explain the absence of Shubnikov-de Haas oscillations is the large disorder broadening inherent to this sample. This broadening can be calculated in Kelvin using  $\Gamma = \hbar/2\tau$  where

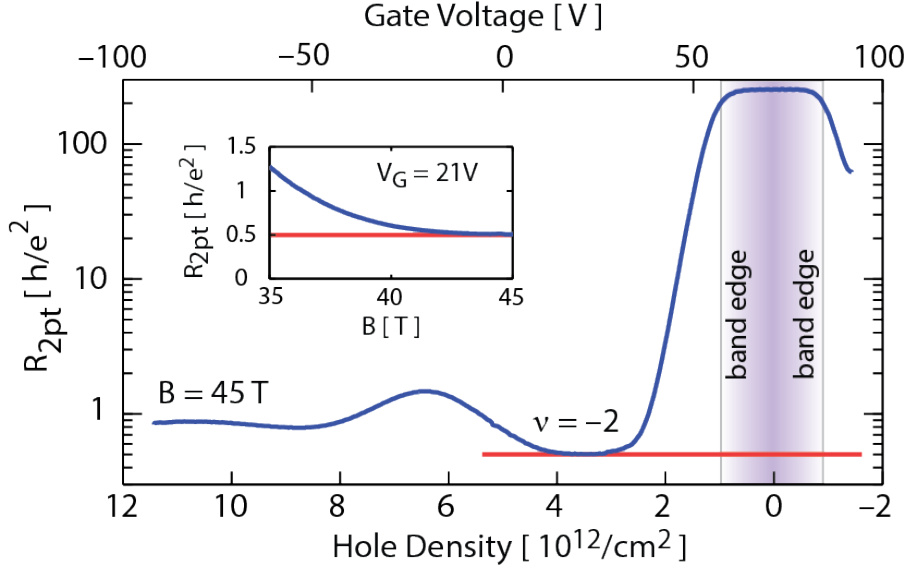


**Fig. 6.6:** Resistance  $R_{2pt}$  vs hole density (lower ordinate) or gate voltage (higher ordinate) at 45 T for sample HG-33 from [24]. The density was estimated by using a parallel plate capacitor model and the charge neutrality point was taken to be the gate voltage about which the curve is symmetric. Data was taken at  $\approx 550$  mK.

$\tau$  is given by  $\tau = \lambda_D/v_f$  or the scattering time defined by the mean defect spacing. Calculating this values yields a LL broadening of 775K. In contrast, the expected splitting of the LLs at 45T in graphene is expected to be  $\approx 3000$ K.

The mobile hole density at  $\nu = -2$  is given by  $2eB/h = 2.2 \cdot 10^{12}/\text{cm}^2$ , however, the quantum Hall plateau is observed at a displacement field corresponding to  $3.6 \times 10^{12}/\text{cm}^2$ . This discrepancy in the number of carriers directly confirms the presence of localized carriers in the resistance plateau region. The discrepancy in carrier density at the  $\nu = -2$  state is roughly equal to the width of the resistance plateau region of  $1.4 \times 10^{12}/\text{cm}^2$  (represented as the purple halo in fig 6.6).

The  $\nu = -4$  or  $\nu = -6$  quantum Hall states are not observed, however, a weak minimum is present at about  $8 \times 10^{12}/\text{cm}^2$ , as seen in Fig 6.6. The expected density of the  $\nu = -6$  plateau is  $6eB/h = 6.6 \times 10^{12}/\text{cm}^2$ , and taking into account the  $1.4 \times 10^{12}/\text{cm}^2$  localized carriers, the total density should be approximately  $8 \times 10^{12}/\text{cm}^2$ . This density is in agreement with the experimental observation under the hypothesis that the resistance plateau causes the shift in Hall plateau densities. The lack of a  $\nu = -6$  plateau is consistent with the fact that the energy gap between the  $N = -2$  and  $N = -1$  LLs is smaller than it is between the  $N = 0$  and the  $N = -1$  LLs.

Shown in Fig 6.7 is the evolution of the localized carrier density as measured by the width of the plateau region. Here, carriers are defined to be localized if the resistance is above  $\approx 6.25 \text{ M}\Omega \approx 240h/e^2$ . Fig 6.7 B shows that localization is reduced as perpendicular magnetic field is increased.

As can be seen in fig 6.8, the sample appears to crossover from an insulating state to a quantum Hall state when the magnetic length becomes less than, or similar to, the mean defect spacing  $\lambda_D$ . The mean defect spacing  $\lambda_D$  was determined by Raman point scattering measurements over several points on the sample per the techniques described in chapter four. Based on this observation, the following heuristic is proposed. At low magnetic fields, the electron's wavefunction is not spatially compressed by the magnetic field (purple halo in fig 6.8), and its extent encompasses several scattering centers (black spheres in fig 6.8). This results in a high resistance from the localization of charge carriers. In contrast, in the high magnetic field regime, the wavefunction is

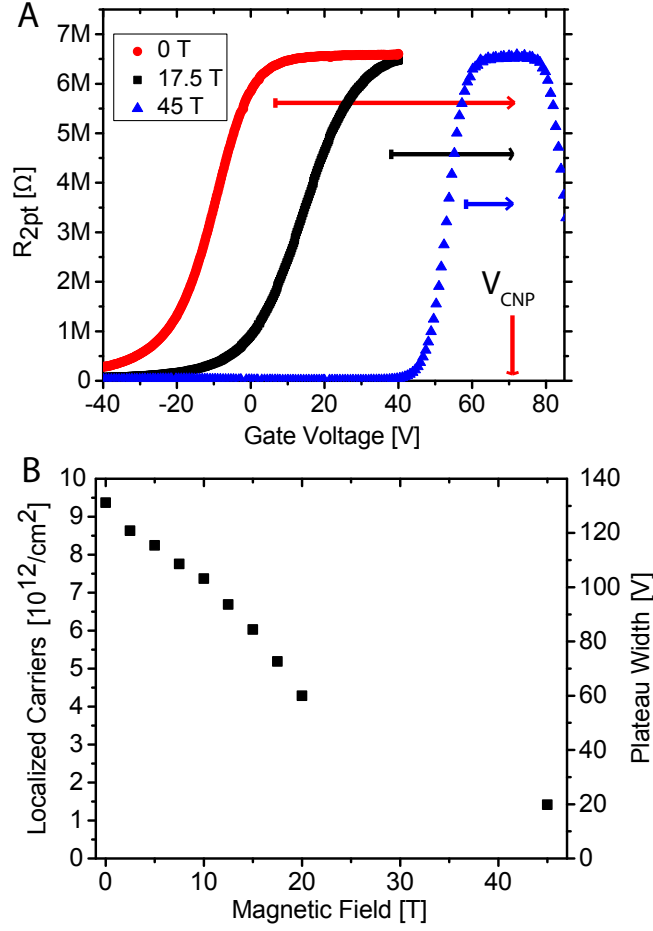


**Fig. 6.7:** A: Resistance  $R_{2pt}$  vs gate voltage for 0 T, 17.5 T and 45 T for sample HG-33. The voltage distance between the charge neutrality point and when the resistance falls below 6.25 M $\Omega$  is plotted on the bottom and converted to carrier density. B: Localized carriers vs magnetic field in units of both carrier density and width of the plateau in gate voltage for sample HG-33. The two are related via  $n = \epsilon V_g / t_{ox} q$  where  $n$  is carrier density,  $\epsilon$  the permittivity of SiO<sub>2</sub> and  $t_{ox}$  the oxide thickness. Data was taken at  $\approx 550$  mK.

spatially compressed to dimensions of the order of the magnetic length, and so conduction may percolate between the scattering centers. In other words, once the magnetic length becomes of the order of the defect spacing ( $l_B \approx \lambda_D$ ), conduction edge channels likely percolate through the disorder. For this

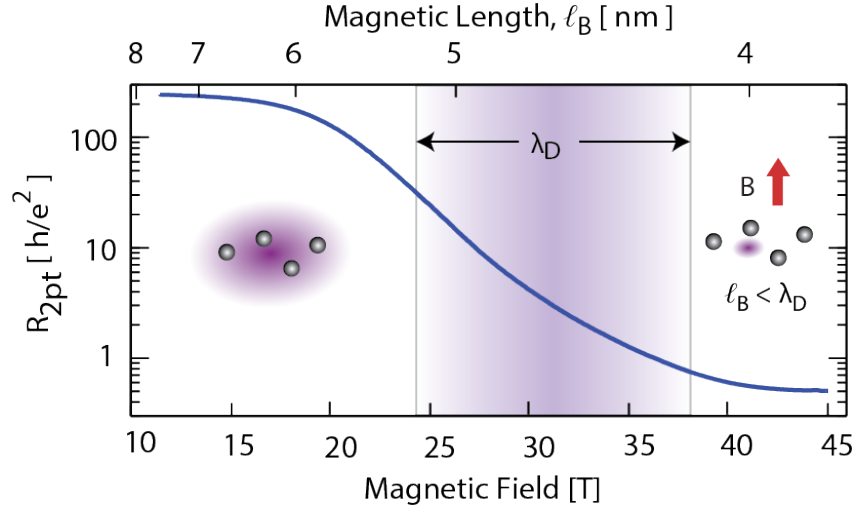


**Fig. 6.8:** Resistance  $R_{2pt}$  of sample HG33 at 21 V gate voltage *vs* both the magnetic field (lower ordinate) and magnetic length,  $l_B$  (upper ordinate). The shaded region indicates the estimated point defect spacing extracted from the Raman spectra from [24]. Data was taken at  $\approx 550\text{mK}$ .

particular device, the defect spacing was estimated to be  $\lambda_D = 4.6 \pm .5 \text{ nm}$  from Raman spectroscopy. Assuming that this device is similar to those analyzed in chapter four, it is expected to have heterogeneous hydrogen coverage. The insulator to quantum Hall transition occurs when the magnetic length is in the range of 4-6 nm, which is consistent with the point defect spacing measured with Raman spectroscopy.

### 6.3.2 Differential Resistance ( $dV/dI$ ) in the Quantum Hall Regime

A useful technique to obtain more information concerning the metallic or insulating behavior of a sample is to perform  $dV/dI$  measurements. To perform these measurements, a signal containing both the AC and DC components is used to measure the differential resistance,  $dV/dI$ , of the sample as a function of bias voltage. In other words, by increasing the kinetic energy of the

electrons, a greater number of conduction channels open. On the other hand, thermal effects may dominate as the sample warms up owing to the Joule heating associated with a finite current flow in a resistive channel. Recall that for insulators  $dR/dT < 0$  and for metals  $dR/dT > 0$ . Therefore as the DC bias is increased, an increase in differential resistance corresponds to a metallic state whereas a decrease in differential resistance corresponds to an insulating state. The latter interpretation in terms of sample warming neglects the modulation of the number of conducting channels that is expected at large biases, such as inter-LL transitions when  $e \times V_{bias} > E_N - E_{N-1}$ . For these experiments, a 100 mV AC RMS bias and a DC bias of up to 700 mV were applied on a 10 M $\Omega$  resistor to source  $\approx 10$  nA of AC current and  $\approx 70$  nA DC current through two points in a similar fashion to what is discussed in chapter three. Measurements of the differential resistance as the DC bias is increased are shown in fig 6.10. The points at which these measurements were made are shown on fig 6.9 and are labelled A, B and C. Label A corresponds to a higher carrier density than the  $\nu = -2$  plateau (0 V, 45 T, labeled A). Label B corresponds to the  $\nu = -2$  plateau (20 V, 45 T, labeled B). Label C corresponds to the local resistance maximum at a higher carrier density than the  $\nu = -2$  plateau (-17 V, 45 T, labeled C). Finally, the last curve, labelled D, is taken in the resistance plateau region at zero magnetic field (20 V, 0 T) and is not labelled in figs 6.9 given that it is taken at 0 T.

Fig 6.10 shows curve C crossing over from a regime where  $dR/dT > 0$  to a regime where  $dR/dT < 0$ . The same figure shows curve A starting to change curvature at the highest bias. Curve B, corresponding to  $\nu = -2$  fill-

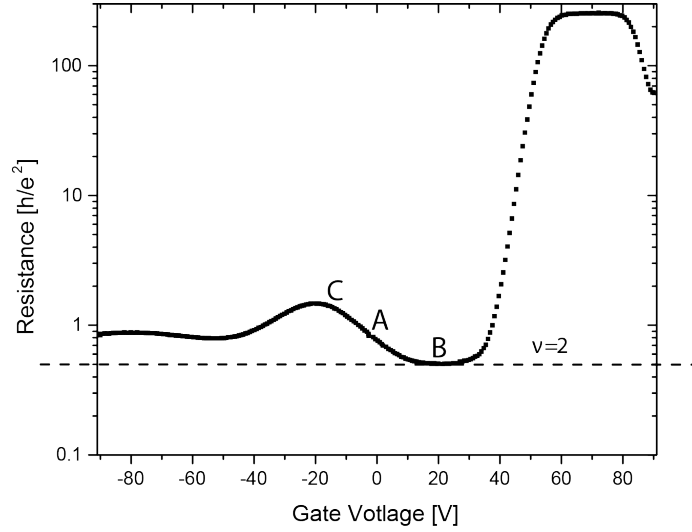


**Fig. 6.9:** Two point resistance as a function of gate voltage for HG-33 at 45 T. The labels show the positions at which the  $dV/dI$  experiments were performed. Data was taken at  $\approx 550\text{mK}$ .

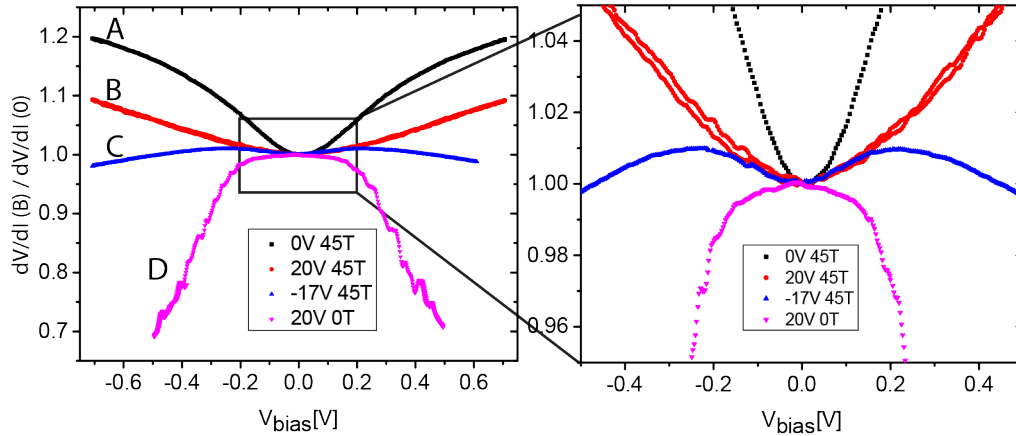


**Fig. 6.10:** Normalized two point differential resistance  $dV/dI$  vs applied DC bias at different gate voltages and magnetic fields for sample HG-33. Data was taken at  $\approx 550\text{mK}$ . Both sweep directions are plotted.

ing, displays an increasing resistance as the bias voltage is increased which is consistent with metallic behavior ( $dR/dT > 0$ ) whereas at zero magnetic field at the same applied gate voltage the differential resistance curve corresponds to insulating behavior ( $dR/dT < 0$ ). The data taken in the localization regime

(20 V, 0 T curve) displays the steepest decrease in resistance, consistent with a highly insulating state. The behavior of this sample is very similar to HGD5 which was used to make the bolometer presented in chapter five. In summary, the  $dV/dI$  data taken in the resistance saturation region shows strictly insulating behavior in contrast to those taken at high field near  $\nu = -2$  which show a transition from metallic like behavior to insulating like behavior.

### 6.3.3 Quantum Hall Effect and the Ioffe-Regel Limit

Here, HG-33 is compared to previous samples that exhibited the quantum Hall effect. In fig 6.11 many of the seminal papers where the quantum Hall effect was measured are shown. The two axes of fig 6.11 are the Ioffe-Regel parameter  $(k_f\lambda)^{-1}$  and the Wigner Seitz radius  $r_s$  which is the ratio of total Coulomb energy to total kinetic energy for the electron gas  $r_s = E_C/E_K$ . Focusing only on the position of the samples on the y axis, it is clear that most samples where the quantum Hall effect was observed are on the metallic side of the Ioffe-Regel limit. Previous to this work, the sample closest to HG-33 was a modulation doped 2DEG of GaAs/AlGaAs [102] (labeled 2 in fig 6.11). Two important differences between the areas labeled one and two in fig 6.11 are that sample two displays a mobility of the order of  $10^4\text{cm}^2/\text{Vs}$  at 0T and away from the subthreshold region and displays no resistance plateau region.

Although the decomposition of the Ioffe-Regel parameter into a product of Fermi wavelength and mean free path is questionable above the metallic limit for conduction, the notion of a dimensionless Ioffe-Regel parameter inferred from a ratio of measured sheet resistance with the resistance quantum still

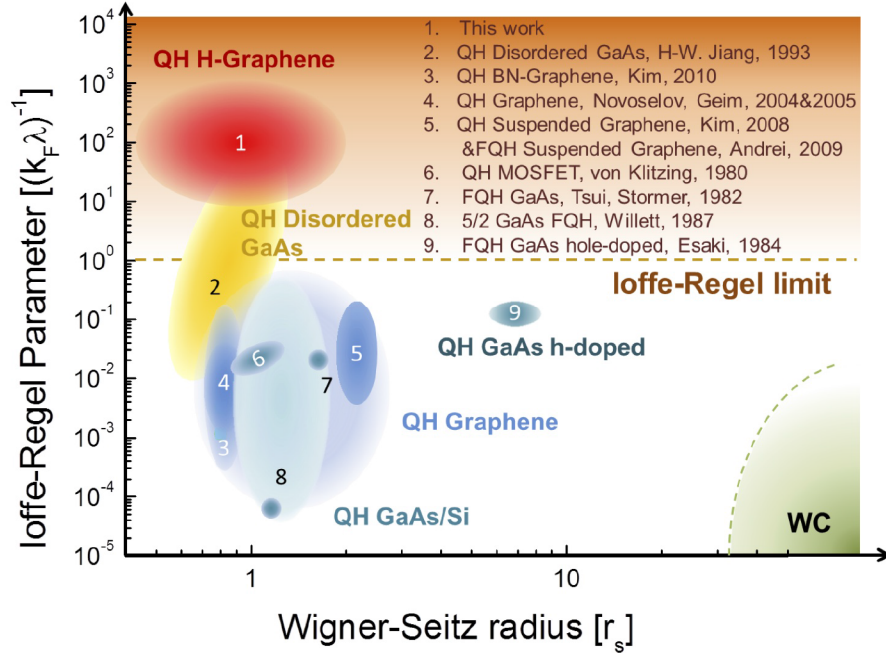


**Fig. 6.11:** Ioffe-Regel Wigner-Seitz diagram for the main families of materials exhibiting the quantum Hall effect. The figure shows the zero-field value of the Ioffe-Regel disorder parameter  $(k_F\lambda)^{-1}$  plotted *vs* the Wigner-Seitz radius, both dimensionless, for the main 2DEG families in which the integer and fractional quantum Hall effect were observed. A brief description of the material system, indexed numerically, is given in the upper right. The size of the labeled regions is representative of the parameter range from observed mobilities and densities. The dashed line shows the Ioffe-Regel limit where  $k_F\lambda = 1$ . The Wigner crystal (WC), thought to occur at large  $r_s$  and low disorder, is highlighted in green. Taken from [24].

gives an approximate measure of disorder. The fact that the quantum Hall effect was observed in a sample with Ioffe-Regel parameter  $\approx 250$  suggests that the quantum Hall effect may be arbitrarily robust against disorder.

A final observation concerns the energy scales accessible by applying magnetic field to highly disordered samples. Graphene with a low coverage of

hydrogen (0.1-0.3 %) has an estimated zero field band gap  $E_G$  of 400-600 meV as measured by ARPES [13]. The energy spacing between the first pair ( $N = 0$  and  $N = \pm 1$ ) of Landau levels is 240 meV at 45T for pristine graphene. The similarity of energy scales shows that this system is ideal to study the interplay between disorder and magnetic confinement as well as the quantum Hall to insulator transition [104].

## Conclusions and Future Work

### 7.1 Conclusions

Presented in this thesis are: the method by which graphene is hydrogenated, the methods used to analyse hydrogenation in terms of obtaining a spatial map of the defects by Raman spectroscopy and gathering the temperature dependent resistance. Raman spectroscopy confirmed the introduction of defects breaking the translational symmetry of graphene and allowed an estimate of defect density induced by hydrogenation to be inferred. Samples appear to hydrogenate at different rates. Also presented are two potential technological applications that could be improved using hydrogenated graphene: thermometers and bolometers. Thermometers showing a sensitivity of  $\approx 10^7 \Omega/\text{K}$  were measured as well as bolometers showing a responsivity of  $\approx 10^5 \text{V}/\text{W}$  and a thermal resistance of  $R_{th} = 3\text{K}/\text{nW}$ . Measurements of the magnetic field dependent transport in both perpendicular and parallel field configurations have been shown to yield opposite magnetoresistance signs. The colossal negative magnetoresistance found in the perpendicular configuration

led to the measurement of the quantum Hall effect in the most disordered 2D system to date as measured by a Ioffe-Regel parameter of  $\approx 250$ . The observed colossal negative magnetoresistance is thought to be a transition from an insulating state to the  $\nu = -2$  quantum Hall state. The experiment was motivated by the question: is the quantum Hall effect robust to arbitrary amounts of disorder? The experiments presented in this thesis have increased the upper bound of disorder where the quantum Hall effect is observed.

### 7.1.1 Hydrogenated Graphene Characterization

As was shown in chapter four, measurements of the Raman spectra of hydrogenated graphene were taken with both a spot point system and an imaging system. An increase in hydrogenation time led to an increase in the ratio of Raman D peak intensity to Raman G peak intensity for the maps which is consistent with an increase of the neutral point defect density. The defect mapping that was measured showed measurable heterogeneity across the area measured.

However, two samples prepared in the same way and hydrogenated for the same duration were measured to have different D/G ratios over an area of 200 by 200  $\mu\text{m}^2$ . It thus appears that samples hydrogenated at different rates despite all efforts to maintain the same experimental conditions. A potential reason for sample to sample variation in hydrogenation time is the corrugation of the graphene sheet. It is known that bonding a hydrogen atom changes the bonding of the carbon atom to the other carbon atoms from  $sp^2$  to  $sp^3$  which causes a lattice deformation. If the lattice is already deformed due to

corrugation, it may provide an optimal region for the hydrogen to start bonding. Another potential source of sample to sample variation is the presence of polymer residues that inhibit the hydrogenation process [105, 106].

Temperature dependent electronic transport was measured at different densities and was found to always yield insulating behavior ( $dR/dT < 0$ ) for all carrier densities. This insulating behavior is qualitatively consistent with a VRH model and none of the measured samples quantitatively fit either Efros-Shklovskii or Mott VRH models. A resistance plateau at zero field was observed in two different samples at a resistance well above the resistance quantum of  $\approx 26 \text{ k}\Omega$ . The cause of this plateau remains unknown.

### 7.1.2 Applications

As was shown in chapter five, hydrogenated graphene was used as a thermometer and a bolometer because of its large  $dR/dT$ .

Hydrogenated graphene has the largest  $dR/dT$  compared to any thermometer sold for cryogenic applications. The  $dR/dT$  value is likely smaller than transition edge sensors, but the temperature range in which the hydrogenated graphene thermometers can operate is much wider. A hydrogenated graphene thermometer can be calibrated to sense minute changes ( $\approx 10 \text{ mK}$ ) in temperature as evidenced by a demonstration of adiabatic demagnetization with the doped silicon substrate supporting the graphene thermometer. Graphene's small heat capacity due to the small atomic number density in a monolayer, large  $dR/dT$  and ability to be placed in proximity to surfaces of interest could make it an ideal thermometer. The reproducibility of the temperature depen-

dent resistance as well as the stability of the samples upon successive cooldowns remains problematic. Such problems could potentially be fixed by device refinement, including encapsulation by an inert superstrate to protect the hydrogenated graphene from the external environment.

Hydrogenated graphene on silicon was measured to have bolometric responsivities as high as  $\approx 10^5$  V/W on par with current commercial bolometers. Two of the contributing factors are its large  $dR/dT$ , and its large thermal resistance ( $R_{th} \approx 3$  K/nW). The precise origin of the large thermal resistance remains unclear, but is possibly due to the very weak electron phonon coupling of graphene that is further altered by electron localization and modification of the acoustic phonon density of states upon hydrogenation.

### 7.1.3 Hydrogenated Graphene in a Magnetic Field

As was shown in chapter six, hydrogenated graphene shows positive magnetoresistance in a parallel magnetic field configuration and negative magnetoresistance in a perpendicular magnetic field configuration. The positive parallel field magnetoresistance was shown to be both temperature and carrier density dependent. As temperature is increased or carrier density is decreased, the magnitude of the positive magnetoresistance declines. It is possible the positive parallel field magnetoresistance could originate in the declining availability of states due to the spin polarization of carriers in the hopping transport regime [98, 99].

The quantum Hall effect was observed with the emergence of the  $\nu = -2$  state from an insulating state in which the Ioffe-Regel parameter is  $\approx$

250. The width in gate voltage or carrier density of the resistance plateau regime is experimentally observed to decline as a function of magnetic field. In other words, as perpendicular magnetic field is increased, the number of localized carriers declines. A heuristic explanation based on a magnetic field mediated carrier percolation through point defects was suggested. A metal like to insulating like transition in the differential two point resistance was measured in the vicinity of the  $\nu = -2$  plateau.

## 7.2 Future Work

From the observations made throughout the thesis, one problem stands out: the reproducibility of the hydrogenation as probed by the Raman spectra and the temperature dependent transport. This problem makes it difficult to conduct systematic studies of transport and other material properties versus hydrogen fraction of  $\text{CH}_x$ . Solving this problem could lead to a better understanding of the influence of disorder on conduction, the opening of a gap as hydrogen fraction increases, and even the commercialization of thermometers using hydrogenated graphene.

To improve the reproducibility of the hydrogenation process, it is necessary to understand the parameters that influence it. The reproducibility of the hydrogenation is determined by the likelihood of bonding hydrogen to carbon. Three factors that can control this are the surface roughness, the presence of contaminants and the temperature of the graphene sheet. Previous experiments have shown that increasing surface roughness correlates with

an increased likelihood of adsorption [107]. It is probable that a corrugated substrate forces reduces the energy barrier for a deformation from  $sp^2$  like to  $sp^3$  like orbital hybridization. Indeed, the decreasing chemical reactivity of the sequence of graphitic allotropes from fullerenes, carbon nanotubes, graphene and ultimately graphite is consistent with our hypothesis. It has also been demonstrated that  $\text{SiO}_2$  is much rougher than substrates like mica [108] or boron nitride [107]. It would be advisable to measure the introduction of disorder as a function of substrate roughness by comparing the hydrogenation process on  $\text{SiO}_2$  with smoother substrates such as mica or boron nitride.

The second factor that could influence the likelihood of hydrogen carbon bonding is the presence of contaminants. Methods like Raman spectroscopy cannot easily detect polymer residues on top of a graphene sheet that could be preventing the hydrogen from bonding to the carbon. Even with the annealing step at  $> 100^\circ\text{C}$  before hydrogenation, it is possible that not all contaminants are removed. Previous experiments have shown that transmission electron microscopy and Auger microscopy should be used to conclusively state whether there are polymer residues on the graphene sheet [109]. Comparing the images from these techniques with Raman maps should clarify whether contaminants are at the source of the reproducibility problem.

The last factor that may contribute to variation in hydrogenation efficiency is the temperature of the graphene sheet. It is clear that bonding hydrogen to carbon requires energy as the lattice needs to reorganize from  $sp^2$  to  $sp^3$  ,

the stable  $\pi - \pi^*$  electron bonding broken, and the carbon-hydrogen  $\sigma$  bond formed. It is certain that increasing the temperature of the substrate provides thermal energy to assist in overcoming the energy barrier required to enable this chemical reaction from taking place. By comparing samples hydrogenated for the same duration at different substrate temperatures, it will be possible to determine if temperature influences density of nucleation sites and thus the reproducibility of the hydrogenation process. It should be noted however, that increasing the substrate temperature will also increase the rate of dehydrogenation, and thus it is unclear what the net effect of substrate temperature will be.

With a reproducible hydrogenation process, it would be possible to tailor the temperature at which the  $dR/dT$  of the device is maximal and optimize thermometer production. The current thermometer market offers thermometers that all have their maximum  $dR/dT$  at low temperatures. By tailoring the amount of disorder, the exponential pick up in the resistance could be designed to happen at the desired temperature.

Another necessary investigation would be to take a closer look at the resistance plateau observed in chapter six. This resistance plateau is unusual because insulators are known to have  $R \rightarrow \infty$  as  $T \rightarrow 0$ . The nature of conduction at this resistance plateau is unknown. Moreover, the measurement of such large resistances becomes challenging because of the presence of shunting capacitances such as the back gate. Calculations show that shunting should not be the issue given the capacitance of a 3 mm by 3 mm hydrogenated

graphene sheet atop a 300 nm  $\text{SiO}_2$  layer resulting in a capacitance of  $\approx 1$  nF. This capacitance results in an impedance of  $\approx 75 \text{ M}\Omega$  at 13 Hz or about an order of magnitude larger than the value at which the resistance saturates.

The resolution of reproducibility of hydrogenation with dose is an important aspect of the study of graphene hydrogenation. From a more fundamental perspective of material properties engineering, achieving a tunable band gap in hydrogenated graphene could open the way to many technological applications. Investigation of tunable band gaps has been explored in 3D materials for the mercury cadmium telluride compound with results suggesting complete control over the gap as evidenced in fig 7.1.

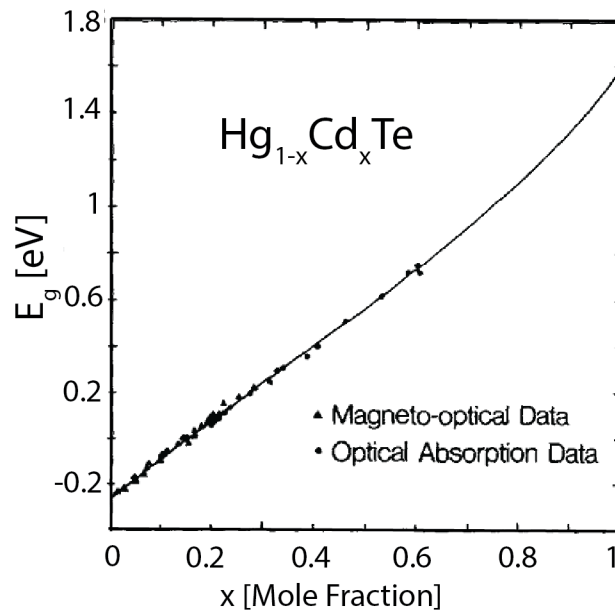


**Fig. 7.1:** Measurement of the band gap of the compound as a function of the mole fraction of cadmium. These measurements are taken with optical absorption and magneto-optical measurements at 80K. Graph from [25].

It is presently not clear whether such control can be achieved in 2D. It is

necessary to further map the progression on the alloy line between graphene and graphane presented in fig 1.1. The basic question remains: can one tune continuously from 2D semi-metal to 2D insulator? Dimensionality is known to play an important role in electronic properties. As hydrogenation times increase, transport measurements are likely to no longer be possible due to incredibly large resistances and optical absorption measurements will be required such as Fourier transform infrared spectroscopy and/or UV-Vis absorbance spectroscopy. These measurements will need to be carried out with control over the electrochemical potential of the device to be able to place it inside or outside the gap. Control over the temperature is also necessary to have the ability to tune the temperature to be smaller or larger than the disorder induced gap. Measuring the absorption as a function of photon energy will allow an investigation of the existence of a band gap and the presence or absence of free carrier absorption. Indeed, the evolution of the absorption spectrum of  $\text{CH}_x$  as  $x$  increases will provide an interesting test of the Thomas-Reiche-Kuhn oscillator f-sum rule for a 2D system evolving from semi-metal to insulator. These measurements would be analogous to the optical spectroscopy taken to measure the band gap of  $\text{Hg}_{1-x}\text{Cd}_x\text{Te}$  shown in fig 7.1.

From the energy band diagram perspective, fig 7.2 gives a hypothetical evolution of graphene with increasing hydrogen fraction. The three images are snap shots along the alloying line between graphene and graphane. The second step shows the emergence of a localized band of states that has been measured in two samples during this project. The picture thus far is conjec-

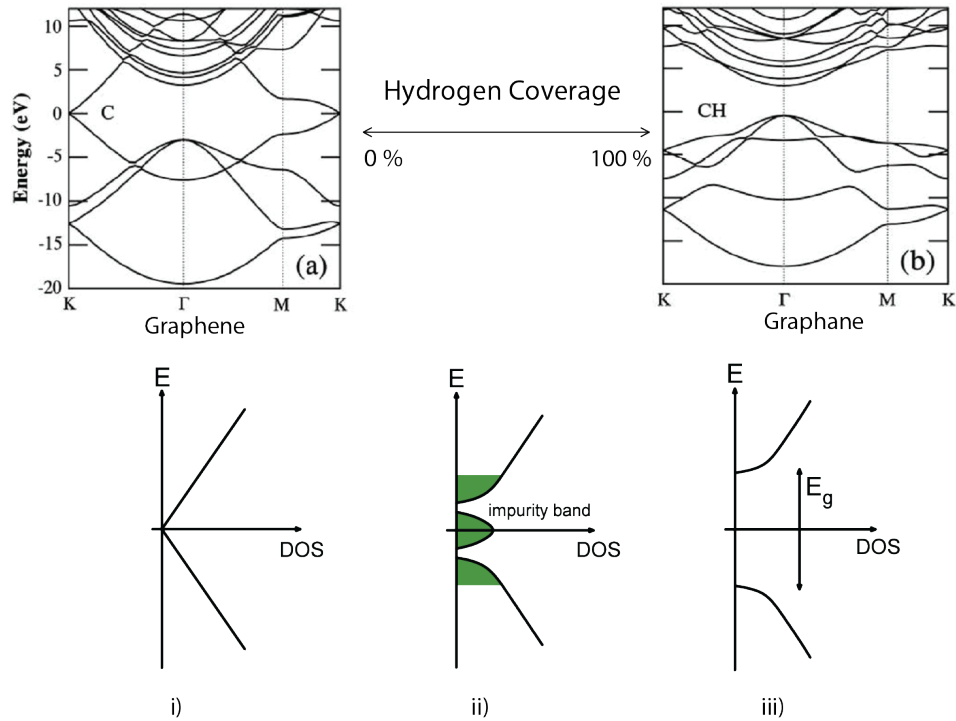


**Fig. 7.2:** Proposed evolution of the energy band diagram as more disorder is introduced. In i), we have the density of states of a pristine graphene sheet. In ii) a gap opens and localized states appear. Mid gap states associated with dangling bonds are generated by isolated hydrogenation sites. iii) A fully hydrogenated graphene, meaning graphane, is anticipated to be a gapped system with no mid gap states because there are no dangling bonds. The green region corresponds to states that are localized. Band diagrams taken from [12]

ture, but the ARPES data [13] presented in the introduction (fig 1.7) suggests the emergence of a impurity band with mid gap states arising from the presence of dangling bonds generated by the bond breaking required for CH bond formation. Whether or not the carriers in this band are localized remains unknown. In other words, it is unclear if a metal insulator transition occurs with variation in mid gap state density. An ideal graphane sheet has an H at every C, leaving behind no dangling bonds for mid gap state formation. In summary,

this thesis has probed only a small portion of the evolution from graphene to graphane, with much remaining uncharted.

# Appendices

Fig 1 shows the mask used to make Hall bars with all its dimensions.

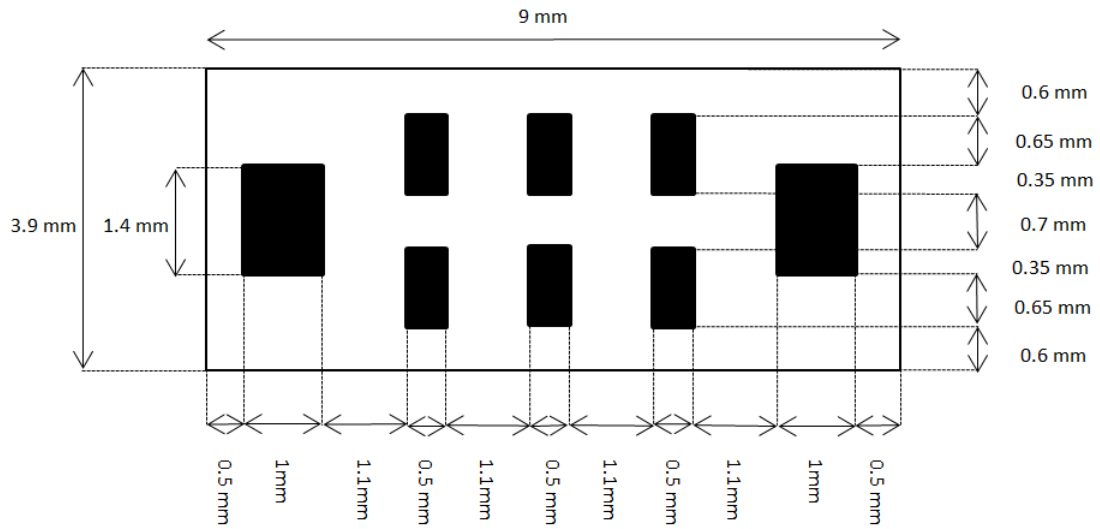


**Fig. 1:** Shadow mask used to make a Hall bar geometry on a sample. The mask material is molybdenum and its thickness is  $\approx 1$  mm.

## References

- [1] Dean, CR, Young, AF, Cadden-Zimansky, P *et al.*, *Nature Physics*, 7, 9 (2011) 693.
- [2] Dean, CR, Wang, L, Maher, P *et al.*, *Nature*, 497, 7451 (2013) 598.
- [3] Lin, YM, Dimitrakopoulos, C, Jenkins, KA *et al.*, *Science*, 327, 5966 (2010) 662.
- [4] Kobayashi, T, Bando, M, Kimura, N *et al.*, *Applied Physics Letters*, 102, 2 (2013) 023112.
- [5] Bae, S, Kim, H, Lee, Y *et al.*, *Nat Nano*, 5, 8 (2010) 574.
- [6] Bunch, JS, Verbridge, SS, Alden, JS *et al.*, *Nano Letters*, 8, 8 (2008) 2458.
- [7] Meyer, JC, Girit, CO, Crommie, MF & Zettl, A, *Nature*, 454, 7202 (2008) 319.
- [8] Mooney, J, sp<sup>2</sup> bonds, <http://www.introorganicchemistry.com/basic.html>, 2013.
- [9] OrgWorld, Organic semiconductors, <http://www.iapp.de/orgworld/basics:whatareorganicsemiconductors>, 2013.
- [10] Sofo, JO, Chaudhari, AS & Barber, GD, *Physical Review B - Condensed Matter and Materials Physics*, 75, 15.

- 
- [11] Casolo, S, Lovvik, OM, Martinazzo, R & Tantardini, GF, *Journal of Chemical Physics*, 130, 5.
- [12] Munoz, E, Singh, AK, Ribas, MA *et al.*, *Diamond and Related Materials*, 19, 56 (2010) 368.
- [13] Haberer, D, Petaccia, L, Farjam, M *et al.*, *Physical Review B*, 83, 16 (2011) 165433.
- [14] Castro Neto, AH, Guinea, F, Peres, NMR *et al.*, *Reviews of Modern Physics*, 81, 1 (2009) 109.
- [15] Mott, NF, *Philosophical Magazine*, 19, 160 (1969) 835.
- [16] Pudalov, VM, Brunthaler, G, Prinz, A & Bauer, G, *Physica E*, 3, 1-3 (1998) 79.
- [17] Dean, CR, *A study of the fractional quantum hall energy gap at half filling*, Ph.D. thesis, McGill University, 2009.
- [18] Von Klitzing, K, Dorda, G & Pepper, M, *Physical Review Letters*, 45, 6 (1980) 494.
- [19] Sabri, SS, *Surface Potentiometry with Graphene Field Effect Transistors for Sensing Applications*, Ph.D. thesis, McGill University, 2013.
- [20] Bischler, U & Bertel, E, *Journal of Vacuum Science and Technology a-Vacuum Surfaces and Films*, 11, 2 (1993) 458.
- [21] Omicron, Product page for the efm 3, [www.omicron.de/en/products/efm-3/instrument-concept](http://www.omicron.de/en/products/efm-3/instrument-concept), 2013.
- [22] Venezuela, P, Lazzeri, M & Mauri, F, *Physical Review B*, 84, 3.
- [23] Lucchese, MM, Stavale, F, Ferreira, EHM *et al.*, *Carbon*, 48, 5 (2010) 1592.
- [24] Guillemette, J, Sabri, SS, Wu, B *et al.*, *Physical Review Letters*, 110, 17 (2013) 176801.
- [25] Hansen, GL, Schmit, JL & Casselman, TN, *Journal of Applied Physics*, 53, 10 (1982) 7099.
- [26] Novoselov, KS, Geim, AK, Morozov, SV *et al.*, *Science*, 306, 5696 (2004) 666.

- [27] Novoselov, KS, Jiang, Z, Zhang, Y *et al.*, *Science*, 315, 5817 (2007) 1379.
- [28] Du, X, Skachko, I, Duerr, F *et al.*, *Nature*, 462, 7270 (2009) 192.
- [29] Feldman, BE, Krauss, B, Smet, JH & Yacoby, A, *Science*, 337, 6099 (2012) 1196.
- [30] Frank, IW, Tanenbaum, DM, Van der Zande, AM & McEuen, PL, *Journal of Vacuum Science and Technology B*, 25, 6 (2007) 2558.
- [31] Lee, C, Wei, X, Kysar, JW & Hone, J, *Science*, 321, 5887 (2008) 385.
- [32] Yuan, JH, Cressler, JD, Krithivasan, R *et al.*, *IEEE Transactions on Electron Devices*, 56, 5 (2009) 1007.
- [33] Head, Graphene racquet, <https://www.head.com/tennis/products/racquets/>, 2013.
- [34] Robinson, JT, Burgess, JS, Junkermeier, CE *et al.*, *Nano Letters*, 10, 8 (2010) 3001.
- [35] Withers, F, Dubois, M & Savchenko, AK, *Physical Review B*, 82, 7.
- [36] Hong, X, Cheng, SH, Herding, C & Zhu, J, *Physical Review B*, 83, 8.
- [37] Moser, J, Tao, H, Roche, S *et al.*, *Physical Review B*, 81, 20.
- [38] Leconte, N, Moser, J, Ordejon, P *et al.*, *ACS Nano*, 4, 7 (2010) 4033.
- [39] Elias, DC, Nair, RR, Mohiuddin, TMG *et al.*, *Science*, 323, 5914 (2009) 610.
- [40] Jones, JD, Mahajan, KK, Williams, WH *et al.*, *Carbon*, 48, 8 (2010) 2335.
- [41] Luo, ZQ, Shang, JZ, Lim, SH *et al.*, *Applied Physics Letters*, 97, 23.
- [42] Matis, BR, Bulat, FA, Friedman, AL *et al.*, *Physical Review B*, 85, 19 (2012) 195437.
- [43] Peres, NMR, Guinea, F & Neto, AHC, *Physical Review B*, 73, 12.
- [44] Pereira, VM, Guinea, F, dos Santos, J *et al.*, *Physical Review Letters*, 96, 3.

- [45] Vardalas, J, *Herbert Kroemer, an Oral History*, New Brunswick, NJ, 2003.
- [46] Bernal, JD, *Proceedings of the Royal Society of London Series a-Containing Papers of a Mathematical and Physical Character*, 106, 740 (1924) 749.
- [47] Wallace, PR, *Physical Review*, 71, 9 (1947) 622.
- [48] Kroto, HW, Heath, JR, Obrien, SC *et al.*, *Nature*, 318, 6042 (1985) 162.
- [49] Iijima, S, *Nature*, 354, 6348 (1991) 56.
- [50] Martel, R, Schmidt, T, Shea, HR *et al.*, *Applied Physics Letters*, 73, 17 (1998) 2447.
- [51] Tans, SJ, Verschueren, ARM & Dekker, C, *Nature*, 393, 6680 (1998) 49.
- [52] Boehm, HP, Heck, W, Sappok, R & Diehl, E, *Angewandte Chemie-International Edition*, 3, 10 (1964) 669.
- [53] Chuhei, O & Ayato, N, *Journal of Physics: Condensed Matter*, 9, 1 (1997) 1.
- [54] Mott, NF, *Advances in Physics*, 16, 61 (1967) 49 .
- [55] Anderson, PW, *Physical Review*, 109, 5 (1958) 1492.
- [56] Abrahams, E, Anderson, PW, Licciardello, DC & Ramakrishnan, TV, *Physical Review Letters*, 42, 10 (1979) 673.
- [57] Mott, N, *Physics Today*, 31, 11 (1978) 42.
- [58] Dynes, RC, *International Journal of Modern Physics B*, 24, 12-13 (2010) 2072.
- [59] Mott, NF, *Philosophical Magazine*, 17, 150 (1968) 1259 .
- [60] Mott, NF & Davis, EA, *Philosophical Magazine*, 17, 150 (1968) 1269 .
- [61] Efros, A & Shklovskii, B, *Electronic Properties of Doped Semiconductors*, Springer-Verlag, 1984.
- [62] Marnieros, S, Berge, L, Juillard, A & Dumoulin, L, *Physical Review Letters*, 84, 11 (2000) 2469.

- [63] Fleury, G, *Effet de l'Interaction Coulombienne sur la Localisation d'Anderson dans le gaz bidimensionnel d'électrons*, Ph.D. thesis, Université Paris Saclay, 2010.
- [64] Das Sarma, S & Pinczuk, A, *Perspectives in Quantum Hall Effects: Novel Quantum Liquids in Low-Dimensional Semiconductor Structures*, Wiley-CVH, 1996.
- [65] Zhang, Y, Jiang, Z, Small, JP *et al.*, *Physical Review Letters*, 96, 13.
- [66] Young, AF, Dean, CR, Wang, L *et al.*, *Nature Physics*, 8, 7 (2012) 550.
- [67] Li, XS, Cai, WW, An, JH *et al.*, *Science*, 324, 5932 (2009) 1312.
- [68] Park, S & Ruoff, RS, *Nature Nanotechnology*, 4, 4 (2009) 217.
- [69] Newman, PF & Holcomb, DF, *Physical Review B*, 28, 2 (1983) 638.
- [70] Robinson, JA, LaBella, M, Zhu, M *et al.*, *Applied Physics Letters*, 98, 5.
- [71] Stobiski, L & Du, R, *Applied Surface Science*, 62, 12 (1992) 77.
- [72] Fink, D, Krauser, J, Nagengast, D *et al.*, *Applied Physics a-Materials Science and Processing*, 61, 4 (1995) 381.
- [73] Tuttle, B, *Physical Review B*, 61, 7 (2000) 4417.
- [74] Bunch, JS, Verbridge, SS, Alden, JS *et al.*, *Nano Letters*, 8, 8 (2008) 2458.
- [75] Eibl, C, Lackner, G & Winkler, A, *Journal of Vacuum Science and Technology a-Vacuum Surfaces and Films*, 16, 5 (1998) 2979.
- [76] Schwarz-Selinger, T, von Keudell, A & Jacob, W, *Journal of Vacuum Science and Technology a-Vacuum Surfaces and Films*, 18, 3 (2000) 995.
- [77] Herzberg, G & Spinks, J, *Molecular Spectra and Molecular Structure: Infrared and Raman spectra of polyatomic molecules*, Prentice-Hall, 1945.
- [78] Jorio, A, Dresselhaus, MS, Saito, R & Dresselhaus, G, *Raman Spectroscopy in Graphene Related Systems*, Wiley, Weiheim, 2011.
- [79] Das, A, Pisana, S, Chakraborty, B *et al.*, *Nature Nanotechnology*, 3, 4 (2008) 210.

- [80] Eckmann, A, Felten, A, Mishchenko, A *et al.*, *Nano Letters*, 12, 8 (2012) 3925.
- [81] Courts, SS & Swinehart, PR, *AIP Conference Proceedings*, 684, 1 (2003) 393.
- [82] Fong, KC & Schwab, KC, *Physical Review X*, 2, 3.
- [83] Graham, MW, Shi, SF, Ralph, DC *et al.*, *Nature Physics*, 9, 2 (2013) 103.
- [84] Song, JCW, Reizer, MY & Levitov, LS, *Physical Review Letters*, 109, 10.
- [85] Lakner, M, Vonlohneysen, H, Langenfeld, A & Wolfle, P, *Physical Review B*, 50, 23 (1994) 17064.
- [86] Wagner, S, Lakner, M & vonLohneysen, H, *Physical Review B*, 55, 7 (1997) 4219.
- [87] Stephens, RB, *Physical Review B*, 8, 6 (1973) 2896, stephens, rb.
- [88] Laboratories, I, Infrared bolometers, <http://www.infraredlaboratories.com/bolometers.html>, 2013.
- [89] Chen, W & Clerk, AA, *Physical Review B*, 86, 12, chen, Wei Clerk, Aashish A.
- [90] Yan, J, Kim, MH, Elle, JA *et al.*, *Nature Nanotechnology*, 7, 7 (2012) 472.
- [91] Woodcraft, AL, Sudiwala, RV, Wakui, E & Paine, C, *Journal of Low Temperature Physics*, 134, 3-4 (2004) 925, woodcraft, AL Sudiwala, RV Wakui, E Paine, C.
- [92] Itoh, KM, Haller, EE, Beeman, JW *et al.*, *Physical Review Letters*, 77, 19 (1996) 4058.
- [93] Chen, Z, Jang, W, Bao, W *et al.*, *Applied Physics Letters*, 95, 16.
- [94] Pop, E, Varshney, V & Roy, AK, *Mrs Bulletin*, 37, 12 (2012) 1273.
- [95] Eto, M & Kamimura, H, *Journal of the Physical Society of Japan*, 58, 8 (1989) 2826.

- 
- [96] Kuivalainen, P, Heleskivi, J, Leppihalme, M *et al.*, *Physical Review B*, 26, 4 (1982) 2041.
- [97] Kamimura, H, *Supplement of the Progress of Theoretical Physics*, 1, 72 (1982) 206.
- [98] Kurobe, A, *Journal of Physics C-Solid State Physics*, 19, 13 (1986) 2201.
- [99] Kurobe, A & Kamimura, H, *Journal of the Physical Society of Japan*, 51, 6 (1982) 1904.
- [100] Shahar, D, Tsui, DC & Cunningham, JE, *Physical Review B*, 52, 20 (1995) 14372.
- [101] Hanein, Y, Shahar, D, Yoon, J *et al.*, *Physical Review B*, 58, 20 (1998) 13338.
- [102] Jiang, HW, Johnson, CE, Wang, KL & Hannahs, ST, *Physical Review Letters*, 71, 9 (1993) 1439.
- [103] Zhang, YB, Tan, YW, Stormer, HL & Kim, P, *Nature*, 438, 7065 (2005) 201.
- [104] Pallecchi, E, Ridene, M, Kazazis, D *et al.*, *Sci. Rep.*, 3.
- [105] Lin, YC, Jin, CH, Lee, JC *et al.*, *ACS Nano*, 5, 3 (2011) 2362.
- [106] Geringer, V, Subramaniam, D, Michel, AK *et al.*, *Applied Physics Letters*, 96, 8.
- [107] Dean, CR, Young, AF, Meric, I *et al.*, *Nature Nanotechnology*, 5, 10 (2010) 722.
- [108] Lui, CH, Liu, L, Mak, KF *et al.*, *Nature*, 462, 7271 (2009) 339.
- [109] Ledwosinska, E, *Graphene as a Mechanical or Electrical Transducer for Far-Infrared/TeraHertz Detection*, Ph.D. thesis, 2013.